

Dripping, jetting and tip streaming

J. M. Montanero^a, A. M. Gañán-Calvo^b

^aDepto. de Ingeniería Mecánica, Energética y de los Materiales and
Instituto de Computación Científica Avanzada (ICCAEx),
Universidad de Extremadura, E-06006 Badajoz, Spain
^bDepto. de Ingeniería Aeroespacial y Mecánica de Fluidos,
Universidad de Sevilla, E-41092 Sevilla, Spain

Abstract

Dripping, jetting and tip streaming have been studied up to a certain point separately by both fluid mechanics and microfluidics communities, the former focusing on fundamental aspects while the latter on applications. Here, we intend to review this field from a global perspective by considering and linking the two sides of the problem. In the first part, we present the theoretical model used to study interfacial flows arising in droplet-based microfluidics, paying attention to three elements commonly present in applications: viscoelasticity, electric fields and surfactants. We review both classical and current results about the stability of jets affected by these elements. Mechanisms leading to the breakup of jets to produce drops are reviewed as well, including some recent advances in this field. We also consider the relatively scarce theoretical studies on the emergence and stability of tip streaming in open systems. In the second part of this review, we focus on axisymmetric microfluidic configurations which can operate on the dripping and jetting modes either in a direct (standard) way or via tip streaming. We present the dimensionless parameters characterizing these configurations, the scaling laws which allow predicting the size of the resulting droplets and bubbles, as well as those delimiting the parameter windows where tip streaming can be found. Special attention is paid to electrospray and flow focusing, two of the techniques more frequently used in continuous drop production microfluidics. We aim to connect experimental observations described in this section of topics with fundamental and general aspects described in the first part of the review. This work closes with some prospects at both fundamental and practical levels.

Keywords: dripping, jetting, tip streaming, surface tension, capillary flow, flow focusing, coflowing, electrospray

Contents		2.5 Searching for scaling laws	13
1	Introduction	3	3
2	Theoretical model	6	3.1
2.1	Bulk equations	7	Local stability analysis
2.1.1	Viscoelasticity	7	3.1.1 Temporal and spatial stability analyses
2.1.2	Electric fields	8	14
2.1.3	Surfactants	8	3.1.2 The convective-to-absolute instability transition analysis . . .
2.2	Interface boundary conditions	9	15
2.2.1	Electric fields	9	3.2 Global stability analysis
2.2.2	The leaky-dielectric model . . .	10	16
2.2.3	Surfactants	11	3.3 Short term response
2.3	Solid boundary conditions	12	17
2.4	The 1D approximation	12	4
			Results of spatio-temporal and global stability analyses
			18
		4.1	Convective-to-absolute instability transition
		4.2	Global stability
			20
		5	Capillary instabilities
			21

Email addresses: jmm@unex.es (J. M. Montanero),
amgc@ues.es (A. M. Gañán-Calvo)

Email addresses: jmm@unex.es (J. M. Montanero),
amgc@ues.es (A. M. Gañán-Calvo)

5.1	End-pinching instability	21	11 Jetting	45
5.2	Rayleigh instability	21	11.1 Direct jetting	45
5.3	Rayleigh stability analysis	22	11.1.1 Gravitational direct jetting	45
5.4	Boundary layer and viscosity effects	22	11.1.2 Electrified direct jetting	46
5.5	Confinement effects	23	11.1.3 Coflowing direct jetting	46
5.6	Compound jets	24	11.1.4 Flow focusing direct jetting	47
5.7	Viscoelasticity effects	24	11.2 Jetting from tip streaming	47
5.8	Electrified jets	25	11.2.1 Gravity-driven steady tip streaming	47
5.9	Surfactant effects	26	11.2.2 Coflowing steady tip streaming	48
5.10	Relationship with the convective-absolute instability transition	26	11.2.3 Selective withdrawal steady tip streaming	48
5.11	Modulated capillary instability	26	12 Electrospray steady tip streaming	49
6 Whipping instabilities	27	12.1 The DC cone-jet mode of electrospray	49	
7 Jet breakup	28	12.1.1 Droplet diameter and electric current	49	
7.1 Newtonian liquids	28	12.1.2 Breakup length and whipping	50	
7.1.1 Satellite droplets	28	12.1.3 Minimum flow rate	50	
7.1.2 The interface pinch-off	28	12.2 Coaxial electrospray	52	
7.2 Viscoelasticity, electric fields and surfactants	30	12.3 AC electrospray	52	
7.3 The 1D approximation	31	12.4 Electrospinning	52	
8 Tip streaming in open systems	31	13 Flow focusing steady tip streaming	53	
8.0.1 Surfactant-driven tip streaming	32	13.1 Liquid-liquid flow focusing	53	
8.0.2 Surfactant-free tip streaming	33	13.2 Gaseous flow focusing	54	
8.0.3 Electrohydrodynamic tip streaming	33	13.2.1 Jet shape and size	54	
9 Microfluidic configurations and governing parameters	35	13.2.2 Breakup length and whipping	54	
9.1 Axisymmetric injection	35	13.2.3 Minimum flow rate	55	
9.2 Gravitational forces	37	13.3 Gaseous stream focused by a liquid current	55	
9.3 Electrical force	37	14 Prospectives and futures	56	
9.3.1 Electrospray and electrospinning applications	37	14.1 Transient ejections	56	
9.3.2 Electric dimensionless numbers	38	14.2 Natural breakup of capillary jets	57	
9.4 Coflowing	38	14.3 Steady tip streaming stability	57	
9.5 Flow focusing	39	14.4 Coaxial capillary jets	58	
9.5.1 Axisymmetric geometry and injection method	39	14.5 Surfactant-driven tip streaming in microfluidics	58	
9.5.2 Flow focusing applications	40	14.6 Other worth noting geometrical and driving effects in jetting	58	
9.5.3 Flow focusing dimensionless numbers	41			
9.6 Selective withdrawal and electrified films	42			
10 Dripping and bubbling	42			
10.1 Direct dripping and bubbling	42			
10.2 Dripping and bubbling from tip streaming	43			

1. Introduction

A multitude of technological applications demands the fragmentation of a continuous phase (gas, liquid or solid) down to the submillimeter scale in a controlled manner. This fragmentation can be produced by gently deforming, stretching and splitting matter in its fluid form. The resulting drops, bubbles, emulsions or capsules are subsequently solidified (if necessary). In this way, these fluid entities are used as templates for the synthesis of complex micro-objects, like multi-component and non-spherical microparticles [1], or large aspect ratio microfibers [2]. These micro-objects can be utilized in very diverse technologies, including drug synthesis and delivery, field responsive rheological fluids, tissue engineering scaffolds, food additives, photonic materials, particle-based display technologies, high-performance composite filler materials, etc. For more details about these technologies, the reader is referred to, e.g., the review of Nunes et al. [3] and references therein.

The formation of the above-mentioned fluid entities on the micro and nanometer scales has been extensively investigated over the last thirty years. Driven by their technological relevance, studies have mainly focused on both the size of the fluidic individuals and the monodispersity degree of the population. Experience has repeatedly shown that these two features are somehow antagonistic with the usual atomization technologies (see, e.g., [4]): the smaller sizes are reached only at the expense of monodispersity, and *vice versa*. Reducing the size of the produced fluid entities requires overcoming the resistance offered by both viscosity and surface tension, which can only be achieved by injecting a significant amount of energy into the process. Only those procedures in which that injection is carefully focused can lead to high monodispersity degrees. Figure 1 illustrates how the atomization mechanism reflects in the internal structure of the produced dispersion.

An ample variety of methods can be used to produce droplets/bubbles of different nature and morphology with narrow diameter distributions on the micro and nanometer scales. Among them, we can distinguish drop-on-demand techniques from those in which droplets/bubbles are continuously generated (Fig. 3) [6, 7]. The thermal and piezoelectric inkjet methods constitute important examples of the first class. In the thermal inkjet method [8], a resistor heats the ink until it vaporizes. Then, a bubble grows and collapses quasi-instantaneously producing the ejection of a droplet through the nozzle. This technique requires inks with high vapor pressure, low boiling point, and high

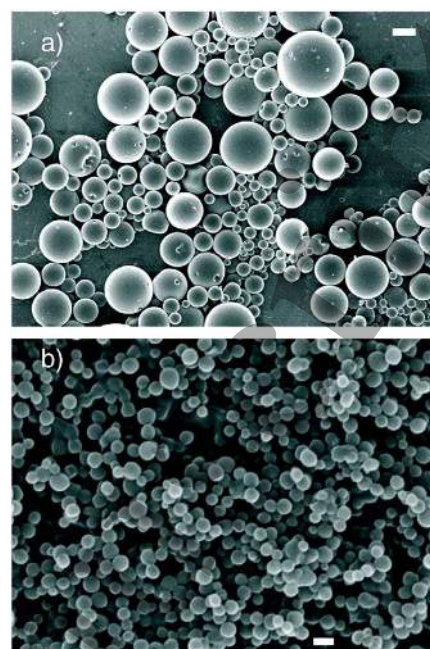


Figure 1: SEM images of Gem-loaded PLGA particles produced by (a) turbulent fragmentation followed by solvent extraction, and (b) capillary breakup using Flow Focusing® followed by solvent extraction (bar length: 1 μm) [5].

kogation stability. In the piezoelectric inkjet method [7, 9], the pressure wave necessary to eject the droplet comes from the contraction of a piezoelectric element. The major limitation of this technique is probably the fact that the ejected inks must have viscosities and surface tensions within relatively narrow ranges. Both the thermal and piezoelectric methods produce drops with diameters similar to that of the ejecting nozzle. The droplet diameter can be adjusted by modulating the electric signal applied to the resistor and piezoelectric element, respectively. Under certain specific conditions, droplets with diameters much smaller than that of nozzle can be formed [10] (Fig. 2). Drop-on-demand methods were originally devised to recreate a digital image onto paper, plastic or other substrates. This technology has been subsequently extended to many other fields. Among them, the building of functional structures in tissue engineering [11] has deserved special mention.

In this review, we will pay attention to microfluidic configurations commonly used to *continuously* produce drops and bubbles [12]. These configurations can operate in the dripping/bubbling and/or the jetting mode. In the dripping/bubbling mode, drops/bubbles are produced right behind the exit of a feeding capillary or ejecting nozzle. On the contrary, a fluid thread long

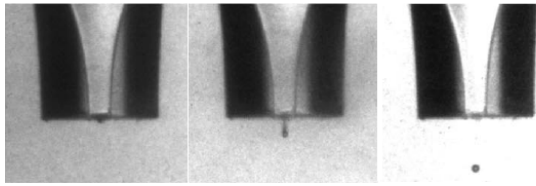


Figure 2: Formation of an ultra-small drop upon application of voltage waveform to a piezoelectric transducer [10]. The drop diameter is about $32\mu\text{m}$.

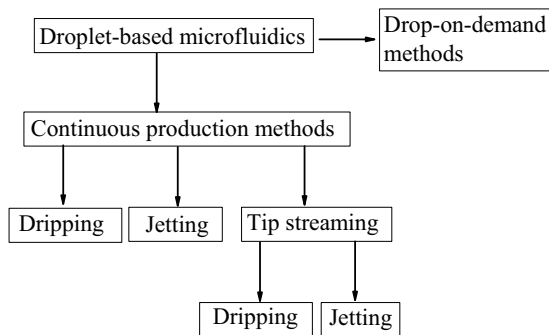


Figure 3: Methods for producing droplets/bubbles on the micrometer and nanometer scales. Tip streaming is a route to dripping and jetting with sizes much smaller than that of the microfluidic device.

compared with its diameter is formed in the jetting regime. In this case, the surface tension eventually triggers instabilities which yield the breakage of the thread into a collection of droplets/bubbles.

The distinction between the dripping/bubbling and jetting regimes is not always clear. There are many applications in which that distinction is established ambiguously: jetting becomes dripping/bubbling as the precursor fluid thread shortens. Ambravaneswaran et al. [13] have proposed to define the dripping-to-jetting transition in a leaky faucet as the parameter conditions for which certain measures of the dynamics undergo sharp changes. According to this criterion, the jet length at the dripping-to-jetting transition ranges from a few to hundreds of jet radii as the viscosity increases. The fact that the jet breakup can be regarded as a local phenomenon in terms of the jet's length can also be considered as the defining condition of the jetting regime. In fact, if the axial size of the breakup region were commensurate with the jet length, then the growth of the capillary perturbation would be affected by the discharge orifice, as it is characteristic of the dripping regime.

While the dripping/bubbling mode generally yields higher monodispersity degrees, the generation of droplet streams in the jetting regime is also very attrac-

tive because it leads to larger production rates. Typically, dripping/bubbling produces drops with sizes that are commensurate with, or even much greater than that of the nozzle. The diameters of the droplets resulting from the inertio-capillary breakup of jets are around twice that of the precursor jet. As will be shown in Sec. 5, this proportion can be significantly altered by viscosity, electric fields, confinement and other factors.

In some configurations such as electrospray [14, 15], coflowing [16], hydrodynamic focusing [17] and flow focusing [18, 19], there is a narrow parameter window leading to the so-called tip streaming [16]. In this regime, the fluid is directed by some external actuation towards the tip of a deformed film, drop or stretched meniscus attached to a feeding capillary. This tip emits small drops/bubbles either directly (Fig. 4) or via the breakage of a very thin jet (Fig. 5). In both cases, the droplets/bubbles are smaller or even much smaller than any characteristic length of the microfluidic device. In almost all the cases, the external actuation mentioned above is gently exerted by interfacial stresses, whether their origin is electrical (Maxwell stresses), hydrodynamic (an outer stream) or any other. Maxwell stresses result from both the accumulation of free electric charges at the interface and the jump of electrical permittivity across this surface [20]. Hydrodynamic forces are caused by the suction (decrease of hydrostatic pressure) and/or viscous traction exerted by an outer stream moving faster than the dispersed phase.

In tip streaming, normal interfacial stresses can cause variations of the hydrostatic pressure on the inner side of the interface, which gives rise to bulk forces throughout the dispersed phase. Tangential stresses accelerate the fluid layer next to the interface, and feed recirculation cells for low enough viscosities and injected flow rates [33]. Both types of stresses may play a critical role depending on the specific configuration considered. Interestingly, normal stresses may play a subdominant role in the final energy budget of some tip streaming realizations. However, they are necessary for this phenomenon to take place. In any case, tip streaming is the result of a delicate balance between the forces driving and opposing the flow. When that balance is tilted in favor of one of those forces, regular or intermittent dripping is obtained. This explains why tip streaming is sometimes an elusive phenomenon, only found under very specific conditions. Despite the important advances in the understanding of tip streaming, there are still many open questions about both the origin of this phenomenon and the instability mechanisms which limit its appearance.

Tip streaming has been shown to be very advantageous at the technological level essentially because it

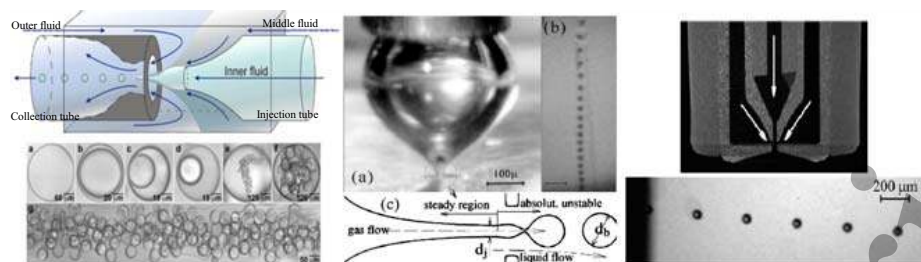


Figure 4: Some examples of dripping/bubbling from tip streaming: double emulsions produced with hydrodynamic focusing (left-hand images) [21], bubbling in flow focusing (central images) [22, 23], and dripping in gaseous flow focusing (right-hand images) [24].

allows for the production of droplets with sizes well below that of the feeding channels, avoiding clogging effects. When designing new devices based on tip streaming, one must concentrate efforts on enhancing the stability and robustness of this mode. For instance, the presence of surfactants at the tip weakens the interfacial tension and makes the phenomenon more robust [34–36]. Modifications of the injection system to eliminate recirculating patterns in the liquid source is another way to stabilize tip streaming [37–40].

Most microfluidic devices possess a planar (two-dimensional, 2D) topology. These devices can be manufactured in essentially one single step, either through photolithography and etching in substrates of silicon or via soft lithography in substrates of polymer materials (PDMS) [41, 42]. This property has conferred great popularity among researchers on the 2D configuration. However, the planar topology also presents certain disadvantages. In these devices, an emerging droplet typically touches the walls of the channel, which can damage fragile particles and cause problems associated with the competitive wetting between immiscible liquids [43]. In addition, PDMS channels swell in strong organic solvents and siloxane-based compounds and tend to deform with intense applied pressures due to their high elasticity. The planar geometry usually requires specific coatings dedicated surfactants. The problems mentioned above are eliminated in an axisymmetric device. The circular cross-section of the outlet channel allows the continuous phase to surround completely and shield the dispersed one at all flow rates. Axisymmetric devices can be fabricated with glass, which is a resistant, smooth and transparent material. Finally, axisymmetry necessarily entails a considerable increase of the droplet production rate with respect to that taking place in the 2D topology. The major drawback of the axisymmetric geometry is probably the fact that microfluidic devices commonly consist of several pieces that must be carefully aligned to obtain the desired out-

come. For this reason, fabrication techniques are in most cases art-dependent and not scalable.

There is an immense body of literature about properties and functionality of microfluidic devices designed for the continuous production of droplets and bubbles. Excellent reviews have summarized the major achievements in this field [12, 36, 44–46]. Here, we will focus on the axisymmetric configuration, which has been reviewed on many fewer occasions, and normally as part of a work with a broader scope [47–50]. In an attempt to present an original vision, we will group the results according to the production mode (instead of the employed technique), distinguishing the “simple” dripping and jetting regimes from their counterparts obtained via tip streaming (Fig. 3). We will devote special attention to electrospray and flow focusing, probably the most popular techniques in this area.

Microfluidics researchers typically pay attention to the development and experimental characterization of microfluidic techniques. Experimental results are rationalized using dimensional analysis, which looks for scaling relationships among dimensionless governing parameters. These studies are frequently assisted by direct numerical simulations to describe global, qualitative or involved aspects of the problem. On the other hand, in the quest to reveal the physics of those aspects, fluid dynamics researchers focus on rather fundamental questions, reducing reality to models kept as simple as possible, which sometimes have little connection with experiments or technological applications. The present review aims to serve and bridge both the microfluidic and fluid dynamicist communities, indicating and emphasizing the connections between results obtained from both approaches. For this reason, we will contemplate not only practical aspects of the problem but also fundamental issues which may help experimentalists to understand those aspects.

This review is organized as follows. In Sec. 2, we describe the theoretical models, approximations and as-

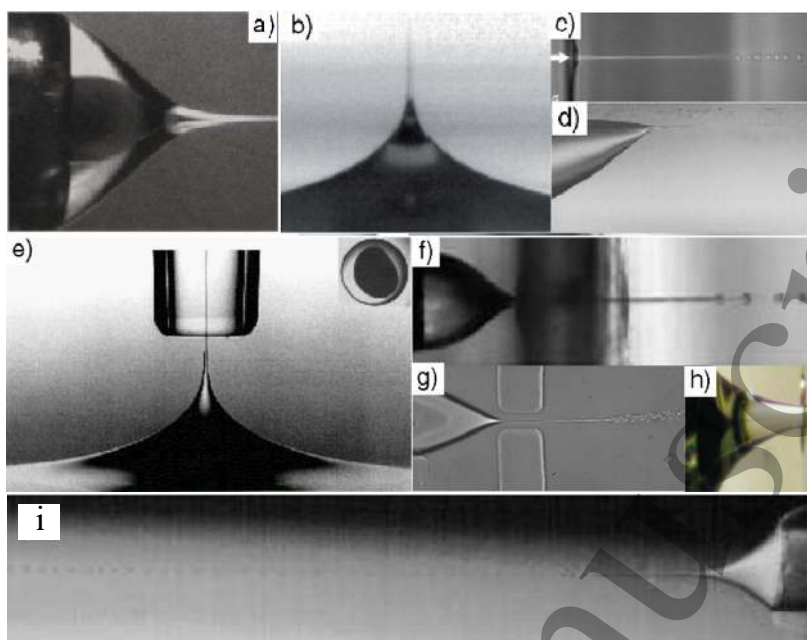


Figure 5: Some examples of jetting from tip streaming: (a) double electrospray configuration to produce capsules down to the nanometer scale [25], (b) electrified film of a low-conductivity liquid [26], (c) liquid transport due to light scattering [27], (d) tip streaming due to the action of a shear flow in the presence of surfactants [28], (e) selective withdrawal to produce microcapsules [29], (f) original flow focusing configuration [30], (g) flow focusing in a 2D microfluidic device [19], (h) double flow focusing arrangement to coat microparticles [31] and (i) liquid-liquid coflowing configuration to produce emulsions [32].

sumptions typically used to examine the microfluidic configurations considered throughout this review. In Sec. 3, we explain some of the fundamental ideas involved in the stability analysis of those configurations. Sections 4–6 present some important results about the linear stability of capillary jets. Here, we also mention studies on the global stability of tip streaming flows. The results are presented in more detail in subsequent sections, once the corresponding microfluidic configurations have been described. Section 7 shows relevant results about the nonlinear breakup of fluid threads. We devote Sec. 8 to discuss fundamental and general features of tip streaming and present relevant results of tip streaming in open systems. The microfluidic configurations considered in this review are described in detail in Sec. 9, where the governing dimensionless numbers are introduced too. Sections 10 and 11 show how those configurations work in the simple dripping and jetting modes, and in their counterparts from tip streaming. We review the scaling laws predicting the sizes of the produced droplets/bubbles and discuss the instability mechanisms which determine the parameter regions where the different modes operate. We pay special attention to electrospray and flow focusing operating in the steady tip streaming regime in Secs. 12 and 13, respectively.

The paper closes with some prospects in Sec. 14.

2. Theoretical model

In this section, we present the theoretical model which frames the microfluidic applications described in this review. It includes the three major factors that increase the level of complexity of the problem: viscoelasticity, electric fields and surfactants. We also introduce two approximations frequently considered in this context: the leaky-dielectric model for electrohydrodynamic processes, and the one-dimensional (1D) approximation for slender configurations.

Liquid-liquid microfluidic devices operate in the laminar regime essentially because of their smallness. However, there are gas-liquid configurations in which turbulence may play a relevant role. In particular, the mixing layer between the high-speed gaseous jet and the surrounding ambient in flow focusing [18] becomes unstable and renders the flow turbulent at small distances from the discharge orifice. Turbulent viscosity slows down the gaseous jet, which losses most of its kinetic energy a few nozzle diameters beyond the orifice. This effect influences the amount of energy transferred by the gaseous stream to the liquid through viscous shear

stresses beyond the discharge orifice. The spinning [51] and electrospinning [52] of polymeric solutions assisted by a high-speed gas current constitute good examples of partially turbulent microfluidic realizations.

2.1. Bulk equations

Consider the density $\rho^{(j)}(\mathbf{r}, t)$ and velocity $\mathbf{v}^{(j)}(\mathbf{r}, t)$ fields for the inner ($j = i$) and outer ($j = o$) fluid phases. These fields verify the continuity equation

$$\frac{\partial \rho^{(j)}}{\partial t} + \nabla \cdot (\rho^{(j)} \mathbf{v}^{(j)}) = 0, \quad (1)$$

which in the incompressible regime reduces to $\nabla \cdot \mathbf{v}^{(j)} = 0$. This last equation applies to all liquid-liquid configurations reviewed here, and also to microfluidic devices used for producing bubbles [22, 23, 53]. It can also be safely used to describe gas-liquid flows in which the outer gaseous stream moves with velocities smaller than, say, 100 m/s. This last condition holds for gaseous flow focusing devices [18] and other liquid ejections assisted with airflow [54, 55] if the applied pressure drop does not exceed around 100 mbar. The comparison between numerical simulations and experiments shows that $\nabla \cdot \mathbf{v}^{(j)} = 0$ constitutes a relatively good approximation even for pressure drops up to 250 mbar [56]. However, compressibility effects must be accounted for in some specific applications; for instance, in solution blow spinning [51, 57] or when using gaseous flow focusing in the Serial Femtosecond Crystallography [58], where the fluid streams are injected on high-vacuum conditions.

In the absence of viscoelasticity and electrical forces, the momentum equation reduces to

$$\rho^{(j)} \left(\frac{\partial \mathbf{v}^{(j)}}{\partial t} + \mathbf{v}^{(j)} \cdot \nabla \mathbf{v}^{(j)} \right) = -\nabla p^{(j)} + \nabla \cdot \boldsymbol{\tau}^{(j)}, \quad (2)$$

where $p^{(j)}(\mathbf{r}, t)$ is the reduced pressure field,

$$\boldsymbol{\tau}^{(j)} = 2\mu^{(j)} \mathbf{D}^{(j)} + \lambda_\mu^{(j)} (\nabla \cdot \mathbf{v}) \mathbf{I} \quad (3)$$

the total extra stress tensor, $\mu^{(j)}$ the fluid viscosity, $\mathbf{D}^{(j)} = 1/2[\nabla_s \mathbf{v}^{(j)} + (\nabla \mathbf{v}^{(j)})^T]$ the deformation rate tensor, $\lambda_\mu^{(j)}$ the dilatational coefficient of viscosity, and \mathbf{I} the identity matrix.

The energy equation

$$\frac{\partial (\rho^{(j)} e^{(j)})}{\partial t} + \nabla \cdot (\rho^{(j)} \mathbf{v}^{(j)} e^{(j)}) = -\nabla \cdot (p^{(j)} \mathbf{v}^{(j)}) + \nabla \cdot (\boldsymbol{\tau}^{(j)} \cdot \mathbf{v}^{(j)}) - \nabla \cdot \mathbf{q}^{(j)} \quad (4)$$

and the ideal gas law $p^{(j)} = \rho^{(j)} R_g^{(j)} T^{(j)}$ are considered in the gaseous phases when compressibility effects are

accounted for. Here, $e^{(j)} = c_v^{(j)} T^{(j)} + 1/2 v^{(j)2}$ and $T^{(j)}$ are the specific energy and temperature fields in each phase, respectively, while $c_v^{(j)}$ and $R_g^{(j)}$ are the corresponding specific heat coefficients and gas constants, respectively. In addition, $\mathbf{q}^{(j)} = -\kappa_T^{(j)} \nabla T^{(j)}$ is the heat flux vector and $\kappa_T^{(j)}$ the thermal conductivity.

2.1.1. Viscoelasticity

Many microfluidic applications involve dilute polymer solutions. These liquids exhibit a constant viscosity (shear thinning can be neglected) over a wide range of shear rates so that the major polymer effects are the increase of the solution viscosity μ with respect to that of the solvent and elasticity [59]. For quasi-monodisperse molecular weight distributions, it is frequently assumed that elasticity can be approximately quantified by a single characteristic time λ_s , related to the slowest relaxation process of the entire molecular chain [60]. The Olroyd-B model [61], or similar approximations including polymer finite extensibility effects [62], has been frequently used in microfluidics to calculate the total extra stress tensor of this type of non-Newtonian liquids. The Olroyd-B model popularity can be attributed to its relative simplicity and the fact that it can be derived from kinetic theory by assuming that the viscoelastic solution is an ideal system of Hookean dumbbells dissolved in a Newtonian liquid [63]. It can also be obtained following a pure continuum approach by assuming (i) a linear relationship between the polymer stress and a certain state variable, (ii) a linear relaxation law for that variable, and (iii) affine motion (i.e., each material point of the polymer follows the flow) [64].

The total extra stress tensor $\boldsymbol{\tau}^{(j)}$ in the Olroyd-B model verifies the constitutive relationship

$$(1 + \lambda_s^{(j)} \mathbf{G}) \boldsymbol{\tau}^{(j)} = 2\mu^{(j)} (1 + \lambda_r^{(j)} \mathbf{G}) \mathbf{D}^{(j)}, \quad (5)$$

where $\lambda_s^{(j)}$ and $\lambda_r^{(j)} = \lambda_s^{(j)} \mu_s^{(j)} / \mu^{(j)}$ are the stress relaxation and retardation time, respectively, $\mu_s^{(j)}$ and $\mu^{(j)}$ are the solvent viscosity and solution viscosity at zero shear rate, respectively, and \mathbf{G} is the upper convective derivative operator. The Navier-Poisson law (3) for an incompressible fluid is recovered for $\lambda_s^{(j)} = 0$.

The Olroyd-B model is believed to provide reasonable predictions in capillary extensional flows [65] when the stress relaxation time is properly adjusted. For this reason, one expects to obtain reliable results from this or similar approximations for microfluidic configurations such as electrospinning [66, 67], flow focusing or selective withdrawal [68], in which the polymer is subject to a strong extensional flow in the tip of the tapering liquid meniscus. In any case, caution must be

taken when other capillary flows are analyzed because the Olroyd-B model can lead to important errors for certain polymer solutions [69]. For instance, Turkoz et al. [70] have recently found considerable discrepancies between the Olroyd-B and experimental [71] self-similar dynamics for the final stages of the thinning of a viscoelastic filament.

2.1.2. Electric fields

Electric forces drive the liquid motion in important microfluidic configurations, such as electrospray [14, 15] and electrospinning [2, 72–79]. In the absence of magnetic fields and permittivity gradients in the bulk, the electric volumetric forces are caused by the net free charge exclusively, and the momentum equation (2) reduces to

$$\rho_e^{(j)} \left(\frac{\partial \mathbf{v}^{(j)}}{\partial t} + \mathbf{v}^{(j)} \cdot \nabla \mathbf{v}^{(j)} \right) = -\nabla p^{(j)} + \nabla \cdot \boldsymbol{\tau}^{(j)} + \rho_e^{(j)} \mathbf{E}^{(j)}. \quad (6)$$

Here, $\rho_e^{(j)}(\mathbf{r}, t)$ is the (volumetric) charge density and $\mathbf{E}^{(j)}$ the electric field given by the Maxwell electrostatic equations

$$\nabla \cdot \mathbf{E}^{(j)} = \frac{\rho_e^{(j)}}{\varepsilon^{(j)}}, \quad \nabla \times \mathbf{E}^{(j)} = \mathbf{0}, \quad (7)$$

where $\varepsilon^{(j)}$ is the electrical permittivity.

In some microfluidic applications, such as electrospray or electrospinning, ionic species, initially present in the liquid or generated at an upstream electrode, migrate across the bulk with zero net production of positive/negative charges owing to electrochemical reactions. In this case, the conservation equation for the volumetric charge density $\rho_e(\mathbf{r}, t)$ becomes [80]

$$\frac{\partial \rho_e^{(j)}}{\partial t} + \mathbf{v}^{(j)} \cdot \nabla \rho_e^{(j)} = \mathcal{D}_{\rho_e}^{(j)} \nabla^2 \rho_e^{(j)} + \nabla \cdot (-K^{(j)} \mathbf{E}^{(j)}), \quad (8)$$

where $\mathcal{D}_{\rho_e}^{(j)}$ is the thermal diffusion coefficient, and

$$K^{(j)}(\mathbf{r}, t) = \sum_k \omega_k \mathcal{F} e z_k^2 n_k^{(j)} \quad (9)$$

is the electrical conductivity. Here, ω_k , z_k and $n_k^{(j)}(\mathbf{r}, t)$ are the mobility, valence and number of mols per unit volume of the k -species, respectively, while \mathcal{F} and e are the Faraday constant and elementary charge, respectively. The ejection of micrometer size fluid objects demands intense electric fields. In this sense, it is sensible to neglect the migration of electric charges due to thermal diffusion versus the electric drift under the applied electric field. It is also frequent to assume that the dissolved species are distributed over most part of the bulk

with a certain degree of uniformity, and, therefore, the electrical conductivity (9) takes a constant value in that region (the so-called Ohmic conduction model) [80]. When this condition does not hold, an electrokinetic model must be adopted.

In an electrokinetic model, the distributions of ions, $n_k^{(j)}$, are calculated throughout the fluid domain by solving the corresponding Nernst-Planck conservation equations [80]. The electrical conductivity (9) is calculated from the spatial distributions of ions and their mobilities. Electrokinetic effects must be taken into account when, for instance, the size of the system is comparable to the Debye layer thickness [80]. In this case, the electrical conductivity exhibits a strong spatial dependence, and the Ohmic model fails to describe the transport of free charges across the fluid medium. The predictions provided by an electrokinetic model also differ from those of the Ohmic approximation in the disintegration of microdroplets and the pinching of fluid threads. In these problems, an interface can be created at a rate at least of the order of the inverse of the electric relaxation time, which makes the Ohmic model overestimate the injection of charges from the bulk onto the fresh interface. In these examples, the evolution of solutions consisting of ions of opposite charges and different mobilities can significantly depend on the polarity of the applied electric field, an effect not contemplated in the Ohmic model. This is an area of research which has not as yet properly explored.

Electrokinetic effects are not the only cause that invalidates the Ohmic model. Equation (8) implicitly assumes that the conduction of electrical charges in the bulk is isotropic. However, in microfluidic configurations such as electrospinning, the presence of macromolecules significantly stretched along the streamwise direction may limit the validity of that assumption in the critical cone-jet transition region. Electrical conduction along the Debye layer may significantly differ from that in the bulk, which may constitute another noticeable source of anisotropy for large surface-to-volume ratios.

2.1.3. Surfactants

Soluble surfactants play a fundamental role in many microfluidic applications [36]. For bulk concentrations below the critical micellar concentration (CMC), soluble surfactants are present as monomers in solution. Above that critical concentration, fluid-like aggregates called micelles form spontaneously. The volumetric concentration of surfactant as monomers, $c^{(j)}(\mathbf{r}, t)$, and micelles, $m^{(j)}(\mathbf{r}, t)$, are calculated in a fluid dynamical

problem from the conservation equations [81]

$$\frac{\partial c^{(j)}}{\partial t} + \mathbf{v}^{(j)} \cdot \nabla c^{(j)} = \mathcal{D}_c^{(j)} \nabla^2 c^{(j)} - n \mathcal{J}_{cm}^{(j)}, \quad (10)$$

$$\frac{\partial m^{(j)}}{\partial t} + \mathbf{v}^{(j)} \cdot \nabla m^{(j)} = \mathcal{D}_m^{(j)} \nabla^2 m^{(j)} + \mathcal{J}_{cm}^{(j)}, \quad (11)$$

where $\mathcal{D}_c^{(j)}$ and $\mathcal{D}_m^{(j)}$ are the diffusion coefficients for the surfactant as monomers and micelles, respectively, n is the number of monomers that constitute a micelle, while $\mathcal{J}_{cm}^{(j)}$ stands for the net rate either of formation ($\mathcal{J}_{cm}^{(j)} > 0$) or breakup ($\mathcal{J}_{cm}^{(j)} < 0$) of micelles per unit volume.

In many droplet production techniques, the dispersed phase is injected from a reservoir at equilibrium ($\mathcal{J}_{cm}^{(j)} = 0$) with uniform monomer and micelle concentrations ($c = \text{const.}$, $m = \text{const.}$). In this case, Eqs. (10) and (11) show that those concentrations are convected by the fluid particles so that they remain constant throughout most of the liquid domain. Spatial variations of surfactant concentration can arise in the sublayer next to the interface, which constitutes a source/sink of surfactant molecules during the system evolution. The transfer of surfactant molecules from the bulk to the fresh interface created during the atomization is essentially governed by the adsorption/desorption process and/or diffusion within the sublayer, while bulk diffusion and convection are much less relevant.

2.2. Interface boundary conditions

“God made the bulk; surfaces were invented by the devil” (Wolfgang Pauli).

Due to the large surface-to-volume ratios reached in microfluidics, interfaces play a critical role in the dynamics of the fluid system. In fact, they contain most of the physics of the problem, which must be modeled accurately. Interfaces are barriers preventing the continuous diffusion of free ions under applied electric fields. The accumulation of charges onto those surfaces and the jump of electrical permittivity in that region substantially affect surface forces and their equilibrium. Surface active molecules adsorb at interfaces and form monolayers which locally reduce the interfacial tension and can exhibit rheological properties. Interfacial (Debye, surfactant, ...) layers are typically much thinner than the rest of the fluid domain, and, therefore, the resolution of their spatial structure is a difficult task. For this reason, they are topologically reduced to surfaces and introduced into the problem as boundary conditions.

The balance of stresses on the two sides of the interface reflects the complexity of the problem considered. In the absence of electric fields and surfactants, it yields

$$\mathbf{n} \cdot \|\boldsymbol{\tau}^{(j)}\| - [\|\rho^{(j)}\| + \|\rho^{(j)}\|(\mathbf{g} \cdot \mathbf{r})] \mathbf{n} = \sigma(\nabla \cdot \mathbf{n})\mathbf{n}, \quad (12)$$

where \mathbf{n} is the unit outward normal vector, $\|A\|$ denotes the difference $A^{(o)} - A^{(i)}$ between the values taken by the quantity A on the two sides of the interface, \mathbf{g} is the gravitational acceleration, and σ is the the interfacial tension. As will be shown below, Eq. (12) is completed by additional stresses when electric fields and surfactants are present.

Neither of the two phases can cross the interface separating immiscible fluids, which leads to the kinematic compatibility boundary condition

$$\frac{\partial f}{\partial t} + \mathbf{v}^{(j)} \cdot \nabla f = 0. \quad (13)$$

The equation $f(\mathbf{r}_s, t) = 0$ determines the interface position \mathbf{r}_s . Alternatively, one can also define the distance $F(\theta, z, t)$ of an interface element from the axis z of a cylindrical coordinate system (r, θ, z) . This function obeys the equation

$$\frac{\partial F}{\partial t} - v_r^{(j)} + \frac{v_\theta^{(j)}}{F} \frac{\partial F}{\partial \theta} + v_z^{(j)} \frac{\partial F}{\partial z} = 0, \quad (14)$$

where $v_r^{(j)}$, $v_\theta^{(j)}$ and $v_z^{(j)}$ stand for the radial, angular and axial components of the velocity field, respectively. This last formulation allows for the implementation of interface-tracking techniques [82] and boundary fitted methods [83] to numerically integrate the hydrodynamic equations. It also facilitates imposing the anchorage of triple contact lines in the numerical simulation.

2.2.1. Electric fields

When electric fields are present, they must be calculated considering the interface boundary conditions

$$\|\boldsymbol{\varepsilon}^{(j)} \mathbf{E}^{(j)}\| \cdot \mathbf{n} = \sigma_e, \quad \|\boldsymbol{\varepsilon}^{(j)} \mathbf{E}^{(j)}\| \times \mathbf{n} = \mathbf{0}, \quad (15)$$

where σ_e is the surface charge density. The conservation equation for this quantity reads

$$\frac{\partial \sigma_e}{\partial t} + \nabla_s(\sigma_e \mathbf{v}_s) + \sigma_e \mathbf{n} \cdot (\nabla_s \cdot \mathbf{n}) \mathbf{v} = -\|K^{(j)} \mathbf{E}^{(j)}\| \cdot \mathbf{n}, \quad (16)$$

where $\nabla_s = \mathbf{l}_s \nabla$ is the surface gradient operator, $\mathbf{l}_s = \mathbf{l} - \mathbf{n}\mathbf{n}$ the tensor that projects any vector onto the interface, \mathbf{l} the identity tensor, and $\mathbf{v}_s = \mathbf{l}_s \mathbf{v}^{(j)}$ the surface velocity. In the above equation, both conduction and diffusion *along* the interface have been neglected. In configurations such as liquid bridges between two electrodes, the variation of the charge density due to surface compression/dilatation and convection is typically neglected, which allows to decouple the calculation of the electric field from that of the velocity field [84–86].

However, this approximation is not valid in tip streaming configurations such as electrospray or electrospinning, in which surface charge convection plays an important role.

When electric fields are applied, the balance of stresses at the interface (12) is completed by adding the Maxwell stresses

$$\tau_M^{(j)} = \epsilon^{(j)} \left(\mathbf{E}^{(j)} \mathbf{E}^{(j)} - \frac{1}{2} \mathbf{I} E^{(j)2} \right) \quad (17)$$

to the left-hand side of that equation ($\|\tau^{(j)}\| \rightarrow \|\tau^{(j)}\| + \|\tau_M^{(j)}\|$).

The equations presented above and in Sec. 2.1.2 allow one to describe electrohydrodynamic phenomena with net free charge both in the bulks and the interface. Typical examples of these phenomena are some flows driven by AC electric fields [87–90], the initial phase of ejections from charged liquid surfaces [91, 92], the oscillation of liquid menisci with periodic emissions of charged liquid droplets [93, 94], the free surface pinching in charged liquid jets [95], or the disintegration of very small drops [96]. Conroy et al. [97] presented an electrokinetic model to describe the breakup of a jet loaded with electrically charged surfactants. This model involves non-zero volumetric and surface charge densities, and, therefore, requires integrating the corresponding conservation equations (8) and (16) for the bulk and interface, respectively.

When the flow conditions are such that interfaces move slowly in comparison with the diffusion velocity of charges under the action of electric fields, charges accumulate onto those interfaces creating a layer where molecular diffusion is halted by electric drift (the so-called Debye layer). As mentioned above, the resolution of the Debye layer structure becomes computationally unaffordable in many cases due to the disparity between the layer thickness (the Debye length) and the system size. This problem has been obviated in coarse-grained simulations where molecular diffusion is not considered, the Debye layer is not resolved, and the electrical conductivity is assumed to be constant [92, 98, 99].

2.2.2. The leaky-dielectric model

The Taylor-Melcher leaky-dielectric model [20, 100–102] has become the most popular alternative to overcome the obstacle mentioned above. The fundamental approximation of this model is to assume that all the net free charge accumulates at the interface within a Debye layer much thinner than the system size. This implies that (i) the charge distribution can be described in terms of the surface charge density σ_e exclusively

($\rho_e = 0$), which accounts for the net free charge contained in the Debye layer, and (ii) the electrical conductivity can be regarded as a constant throughout the liquid domain (the Ohmic conduction model). Therefore, Eq. (8) is no longer necessary, and electric forces in the bulk can be neglected. One can probably state that Melcher and Taylor [20] defined through their pioneering work the field of electrohydrodynamics, where the interaction between low-conductivity liquids and strong electric fields continues to yield new and intriguing phenomena [103].

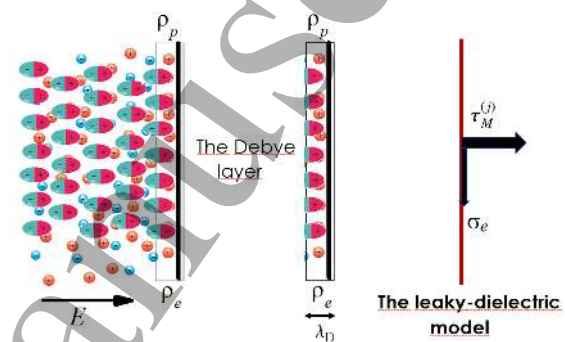


Figure 6: The simplification in the leaky-dielectric model. The Debye layer of thickness λ_D is reduced to a infinitely thin surface with a free charge density σ_e and subject to Maxwell stresses $\tau_M^{(j)}$. These stresses result from both the net free charge accumulated in the Debye layer (ρ_e) and the interfacial charge polarization (ρ_p). The net free charge is neglected in the bulk.

The leaky-dielectric model has proved to be a useful tool to examine the dynamical behavior of poorly conducting droplets in poorly conducting baths. In particular, it provides accurate predictions for the steady cone-jet mode of electrospray [104–112] and electrospinning [67, 77], two techniques reviewed in this paper. It has been used to describe AC electrospray phenomena [113, 114], and has been extended to simulate ionic liquid menisci undergoing evaporation of ions [115, 116].

The leaky-dielectric model is not exempt from severe limitations. For instance, its extension to include anisotropic and/or inhomogeneous conductivity can violate the conservation of volumetric charge ($\nabla \cdot \mathbf{j}^{(j)} = 0$, $\mathbf{j}^{(j)}$ is the current density), which is automatically satisfied for constant scalar conductivity ($\nabla \cdot \mathbf{j}^{(j)} = \nabla \cdot (K^{(j)} \mathbf{E}^{(j)}) = K^{(j)} \nabla \cdot \mathbf{E}^{(j)} = \rho_e^{(j)} / \epsilon^{(j)} = 0$). This implies that if the electrical conductivity is linked to, e.g., the state of dissolved polymers in a viscoelastic solution, then the volumetric charge density in the bulk must be calculated even if electric forces are neglected there.

2.2.3. Surfactants

Surfactants present in solution as monomers adsorb onto the interface. At equilibrium, the Langmuir adsorption isotherm relates the volumetric concentration $c^{(j)}$ and surface distribution Γ of surfactant if $c^{(j)} < \text{CMC}$. For $c^{(j)} > \text{CMC}$, the surface concentration Γ saturates to an approximately constant value Γ_c .

In a non-equilibrium state, Γ verifies the conservation equation [81]

$$\frac{\partial \Gamma}{\partial t} + \nabla_s(\Gamma \mathbf{v}_s) + \Gamma \mathbf{n} \cdot (\nabla_s \cdot \mathbf{n}) \mathbf{v} = \mathcal{D}_s \nabla_s^2 \Gamma + \mathcal{J}_{\Gamma_c}^{(i)} + \mathcal{J}_{\Gamma_c}^{(o)}, \quad (18)$$

where \mathcal{D}_s is the surface diffusion coefficient, and $\mathcal{J}_{\Gamma_c}^{(j)}$ denotes the net flux of surfactant from the bulk to the interface due to the adsorption/desorption process. To derive this equation, one supposes that the micelles do not adsorb directly onto the interface, but that they completely dissociate into bulk monomers prior to the adsorption process [81].

The adsorption/desorption net flux must equal the diffusive flux in the sublayer next to the interface, i.e.

$$\mathcal{D}_c^{(j)} \nabla c^{(j)} \cdot \mathbf{n} = \pm \mathcal{J}_{\Gamma_c}^{(j)}, \quad \mathcal{D}_m^{(j)} \nabla m^{(j)} \cdot \mathbf{n} = 0, \quad (19)$$

where the sign $+$ and $-$ applies to $j = o$ and i , respectively.

Due to the small values taken by surface diffusion coefficient \mathcal{D}_s for strong surfactants [117], the convection of these molecules over the interface is much more important than the diffusion mechanism in most microfluidic applications (the surface Péclet number is much greater than unity), and the latter is neglected.

In many configurations, the hydrodynamic characteristic time is much smaller than that characterizing the adsorption/desorption process, which implies that the surfactant can be regarded as insoluble. This considerably simplifies the analysis because it eliminates both Eqs. (10) and (11) and the (normally unknown) quantities $\{\mathcal{D}_c^{(j)}, \mathcal{D}_m^{(j)}, \mathcal{J}_{cm}^{(j)}, \mathcal{J}_{\Gamma_c}^{(j)}\}$ from the problem.

The opposite limit to insolubility is that in which the adsorption/desorption kinetics is sufficiently fast for the volumetric concentration at the interface, c_s , to be in local equilibrium with the surface concentration Γ [118]. In this case, c_s evolves according to the Langmuir equation

$$\frac{\Gamma}{\Gamma_\infty} = \frac{\hat{\beta}/\hat{\alpha} c_s}{1 + \hat{\beta}/\hat{\alpha} c_s}, \quad (20)$$

where Γ_∞ is the maximum packing density, and $\hat{\beta}$ and $\hat{\alpha}$ are the kinetic constants for adsorption and desorption, respectively. In this limit, the transport of surfactant molecules between the bulk and the interface is limited by diffusion in the sublayer next to that surface.

The dependence of the surface tension σ upon the surfactant surface concentration Γ is frequently calculate from the Langmuir equation of state [117]

$$\sigma = \sigma_0 + R_g T \Gamma_\infty \ln \left(1 - \frac{\Gamma}{\Gamma_\infty} \right), \quad (21)$$

where σ_0 is the surface tension of the clean interface, R_g the gas constant, and T the temperature. Experiments show that $\sigma(\Gamma)$ reaches a plateau at $\Gamma \simeq \Gamma_c$. This effect is not captured by Eq. (21), which must be replaced by an appropriate equation of state if the volumetric concentration $c^{(j)}$ is expected to reach values close to the CMC.

Fresh interfaces between two immiscible fluids are constantly formed in droplet emulsification produced by microfluidic devices. If the multiphase system contains surfactants with adsorption times larger than or comparable to the droplet formation time, the interface may be subjected to a dynamic interfacial tension different from that measured at equilibrium [Eq. (21)]. The balance of stresses at the interface, Eq. (12), involves now the local value of the surface tension (the so-called soluto-capillarity effect). In addition, this boundary condition is completed by adding the term $\tau_{st} + \tau_{sn} \mathbf{n}$ to the right-hand side of Eq. (12). Here, τ_{st} and τ_{sn} are the surface stresses tangential and normal to the interface, respectively, both associated with the existence of a surfactant monolayer at that surface.

The tangential component of the surface stress includes both the Marangoni stress due to the surface tension (surfactant concentration) gradient and the superficial viscous stress associated with the variation of the surface velocity \mathbf{v}_s . Marangoni and superficial viscous stresses tend to eliminate inhomogeneities of surfactant concentration and surface velocity, respectively.

The superficial viscous stress obeys different constitutive relationships depending on the surfactant molecule nature. For a Newtonian interface [119], the surface stress can be calculated as [120]

$$\tau_{st} = \nabla_s \sigma + \nabla_s [(\kappa^s - \mu^s) (\nabla_s \cdot \mathbf{v}_s)] + 2 \nabla_s \cdot (\mu^s \mathbf{D}_s), \quad (22)$$

where $\mathbf{D}_s = 1/2 [\nabla_s \mathbf{v}_s \cdot \mathbf{I}_s + \mathbf{I}_s \cdot (\nabla_s \mathbf{v}_s)^T]$ is the surface rate of deformation tensor, κ^s the dilatational surface viscosity, and μ^s the shear surface viscosity. These two surfactant properties depend on the surfactant surface concentration Γ [121]. Adsorbed surfactant monolayers at fluid surfaces usually exhibit rheological properties too. In fact, surface viscosities frequently depend on the timescale and amplitude of the deformation owing to surface relaxations and nonlinear responses [122].

The lack of precise information about the values taken by the surface viscosities, as well as the mathematical complexity of the calculation of the surface viscous stresses, has motivated that most of the experimental and theoretical works in microfluidics do not take into account those stresses. However, they may considerably affect the dynamics of interfaces even for surface viscosities much smaller than the bulk ones [123]. This may occur for two reasons: (i) surface viscous stresses may significantly alter the transport of surfactants over the interface, which may have important consequences in the resulting solutocapillarity effect and Marangoni stresses; and (ii) their relevance increases as the surface-to-volume ratio increases, as happens, for instance, during the interface breakup [123].

It is believed that foam and emulsion stability can be caused by the surface shear viscosity of the surfactant used to stabilize them. In fact, surface viscosity can significantly increase the drainage time during the coalescence of two bubbles/droplets [124]. However, there is no clear evidence that soluble and small-molecule surfactants have measurable surface shear viscosities [125]. This raises doubts about the role played by surface shear rheology in the stability of foams and emulsions treated with soluble surfactants. In fact, surfactants can stabilize emulsions through Marangoni stresses too. The surfactant depletion in the center of the gap between two approaching interfaces produces surface tension gradients. The resulting Marangoni stresses resist the outwards radial flow in the gap, thus preventing coalescence [126]. Surface diffusion of surfactant hinders this mechanism as the size of the coalescing droplets decreases. A similar effect is produced by the surfactant solubility when the adsorption-desorption time is comparable to that of the gap drainage.

2.3. Solid boundary conditions

The formulation of the problem is completed by imposing the noslip condition and zero diffusion flux of surfactants at the solid surfaces. In addition, triple contact lines must be pinned when they meet edges delimiting solid elements of microfluidic devices.

The triple contact line anchorage condition must also be imposed when studying the linear stability of capillary systems interacting with real surfaces, i.e., those exhibiting contact angle hysteresis. As discussed by Dussan [127], the contact angle of the unperturbed state takes a value in the interval delimited by the receding and advancing contact angles, for which the contact line velocity vanishes. Because linear perturbations produce only infinitesimal variations around that angle, the triple contact line remains fixed during the evolution of those

perturbations. In the nonlinear regime, the dynamic contact angle can take values outside the interval mentioned above. In this case, the triple contact line slips over the solid surface. The dynamic contact angle depends on the triple contact line speed, although it loses its sensitivity to that quantity as the latter increases in value [127].

When the triple contact line moves, the noslip boundary condition inevitably leads to a singularity at that line. For this reason, one usually adopts the so-called slip model [128–130],

$$\mathbf{v}^{(j)} \cdot \mathbf{e}_{\parallel} = s^{(j)} (\mathbf{e}_{\parallel} \cdot \boldsymbol{\tau}^{(j)} \cdot \mathbf{e}_{\perp}), \quad (23)$$

at the solid surface, where \mathbf{e}_{\parallel} stands for any of the two unit vectors on the solid surface, \mathbf{e}_{\perp} is the outward unit vector perpendicular to that surface, and $s^{(j)}$ is the slip coefficient.

2.4. The 1D approximation

The theoretical model described above can be greatly simplified when the inner fluid (typically a jet) adopts a slender shape along the streamwise direction z . In this case, the inner velocity profile is approximately parallel and uniform [131]. If one also considers the leaky-dielectric approximation, and neglects the dynamical effects of the outer medium, the 1D model for steady flow becomes [28, 66, 67, 132–134]

$$Q = \pi F^2 w, \quad (24)$$

$$I = \pi F^2 K^{(i)} E_z + 2\pi F w \sigma_e, \quad (25)$$

$$\begin{aligned} \rho^{(i)} w w' &= \rho^{(i)} g + \frac{T'}{\pi F^2} - \left(\frac{\sigma}{F} \right)' + \frac{\sigma_e \sigma_e'}{\varepsilon^{(o)}} \\ &+ (\varepsilon^{(i)} - \varepsilon^{(o)}) E_z E_z' + \frac{2\sigma_e E_z'}{F}, \\ &+ \frac{2\sigma'}{F} + \frac{(9\mu^S F w')'}{2F^2} + \frac{(\kappa^S F w')'}{2F^2}, \end{aligned} \quad (26)$$

where Q and I are the flow rate and electric current transported by the jet, respectively, $F(z)$ and $w(z)$ are the interface contour and jet velocity, respectively, $E_z(z)$ is the axial component of the electric field, and $T = \pi F^2 (\tau_{zz} - \tau_{rr})$ is the tensile force in the jet. The prime denotes the derivative with respect to the z coordinate. The elements τ_{zz} and τ_{rr} of the total extra stress tensor are given by the corresponding constitutive relationship: Navier-Poisson law [135], Olroyd-B model [67], FENE-P model [136], etc. The last three terms in Eq. (26) correspond to the Marangoni stress and the surface viscous stresses caused by a surfactant monolayer [134]. The shear and dilatational viscosity terms have the same

form, and, therefore, the relevant parameter to this order becomes $9\mu^S + \kappa^S$. Something similar occurs in the analysis of films, in which the two surface viscosities are indistinguishable from each other because they enter the problem through the single parameter $\mu^S + \kappa^S$ [137].

The 1D approximation provides useful predictions for many microfluidic configurations considered in this review, such as jets emitted at large enough flow rates in the gravitational [138], electrospray [109], electrospinning [67], coflowing [139] and flow focusing [140] configurations (in the last two cases, the dynamical effects of the outer medium are to be taken into account). However, important 2D effects can be erroneously neglected in the inception of the emitted jet and in the later stages of a viscoelastic filament thinning [70].

Equation (26) admits a twofold interpretation. In an Eulerian frame of reference, its spatial integration leads to the balance between the driving and resistant forces acting on the whole liquid thread. On the other hand, if one focuses on a liquid slice moving throughout the fluid domain, then the terms of Eq. (26) yields the kinetic energy supplied to or withdrawn from that slice between z and $z+dz$, which allows one to approximately compute the so-called “energy budget” for the flow.

2.5. Searching for scaling laws

Many microfluidic applications described in this review involve complex phenomena, for which theoretical analyses based on first principles may not lead to practical results. In this case, it is very useful to search for scaling laws that unify the description of similar experiments and allow one to identify the physical mechanisms governing the associated applications.

Little can be said, in general terms, about the above-mentioned purpose beyond what Barenblatt [141] explained in his remarkable text on dimensional analysis, self-similarity, intermediate asymptotics and scaling laws. In particular, the author devotes one of the chapters to the most general class of problems that exhibit scaling laws: those showing incomplete similarity. These problems are characterized by the existence of a canonical set $\{\chi_1, \chi_2, \dots, \chi_N\}$ of N non-dimensional parameters governing the analyzed variable a_0 when the latter is written in a *physically meaningful* non-dimensional form, $\chi_0 = a_0/\tilde{a}_0$, where $\tilde{a}_0 = \prod_{m=1}^M a_i^{\beta_m}$ is the characteristic scale of a_0 expressed in terms of M significant dimensional parameters $\{a_1, a_2, \dots, a_M\}$ and β_m are rational exponents.

The sought scaling law typically involves P fitting dimensionless parameters $\{\alpha_1, \alpha_2, \dots, \alpha_P\}$, i.e.

$$\chi_0 = f(\chi_1, \chi_2, \dots, \chi_N; \alpha_1, \alpha_2, \dots, \alpha_P). \quad (27)$$

To determine the values of those parameters, one may calculate the probability density function $\text{PDF}(\alpha_1, \alpha_2, \dots, \alpha_P)$ of the logarithmic errors

$$\epsilon^{(k)} = \log f(\chi_1^{(k)}, \chi_2^{(k)}, \dots, \chi_N^{(k)}; \alpha_1, \alpha_2, \dots, \alpha_P) - \log \chi_0^{(k)} \quad (k = 1, 2, \dots, K) \quad (28)$$

for different values of the set $\{\alpha_1, \alpha_2, \dots, \alpha_P\}$. Here, $\{\chi_0^{(k)}, \chi_1^{(k)}, \chi_2^{(k)}, \dots, \chi_N^{(k)}\}$ represent the values of the corresponding dimensionless variables measured in the k th experimental realization or numerical simulation. Then, the normal distribution with zero average is fitted to the resulting PDF. The optimum values of $\{\alpha_1, \alpha_2, \dots, \alpha_P\}$ are those leading to the normal distribution with minimum variance.

In most problems, this general guidance is hampered by the lack of sufficient experimental data or the limited physical knowledge of the problem. Nevertheless, these limitations do not pose insurmountable barriers in many areas of physics. This is the case of the particular field considered in this review, characterized by the existence of *motion* and *fluid interfaces*. The former always demands a source of energy, while the latter enables the concurrence of different types of surface energies. A finite amount or a continuous flow of energy can be supplied to the system depending on whether its motion is incipient or steady, respectively. In most cases, that motion is limited by either dissipative or mass (potential) forces. Typically, the balance between driving and resistant forces at a certain critical situation allows completing the set of equations that determine the exponents of the scaling laws. Most of the scaling laws reviewed here have been derived following these general ideas.

3. Stability analysis

In this section, we review some of the general ideas which underlie the stability analysis of the configurations considered in this work. Results related to those configurations are reviewed in Sec. 4.

3.1. Local stability analysis

The direct numerical simulation of the 3D model described in Sec. 2 constitutes a difficult task, even if simplifications like the leaky-dielectric model or the surfactant insolubility condition are taken into account. Nevertheless, relevant information can be extracted by conducting the linear stability analysis of the base flow. In this analysis, one avoids the time integration of the model by splitting the calculation into two parts: the

steady base flow and its linear modes. These modes describe the base flow response to small-amplitude perturbations, which determines the system stability in most cases.

The problem becomes analytically or semi-analytically tractable when the stability analysis is conducted locally. In this analysis, one assumes that the characteristic length of the perturbations is much smaller than the hydrodynamic length of the base flow in the streamwise direction (the symmetry axis). In this way, one supposes that this flow is locally homogeneous in that direction. This is commonly referred to as the WKBJ approximation and allows one to examine the stability of slowly spatially varying base flows. In this approximation, the evolution of perturbations in the linear regime at a given flow station can be described as the superposition of the normal modes

$$\Phi^{(j)}(r, \theta, z; t) = \phi^{(j)}(r) e^{i(m\theta + kz - \omega t)}, \quad (29)$$

where $\Phi^{(j)}$ represents any variable of the problem, (r, θ, z) is a cylindrical coordinate system whose z -axis is the base flow symmetry axis (the streamwise direction), $\omega = \omega_r + i\omega_i$ and $k = k_r + ik_i$ are the perturbation eigenfrequency and wavenumber, respectively, while m is the azimuthal mode number.

The fulfillment of the hydrodynamic equations and boundary conditions determines the spatial structure of the linear mode, $\phi^{(j)}(r)$, and, more importantly, leads to the (dimensionless) dispersion relationship

$$\mathcal{D}_m(k, \omega; \{\mathcal{P}_i\}) = 0, \quad (30)$$

which gives the eigenfrequency ω of a mode with azimuthal and axial wavenumber m and k , respectively, as a function of the parameters $\{\mathcal{P}_i\}$ ($i = 1, 2, \dots, N$) characterizing the problem. The dispersion relationship is applied throughout the flow considering the local values of the parameters $\{\mathcal{P}_i\}$ of the problem. The total growth of the perturbation results from the integration of the Eulerian growth rate $\omega_i(z)$ along Lagrangian paths, taking into account the variation of k and $\{\mathcal{P}_i\}$ along those paths (see, e.g., [138]).

The relative simplicity of the calculation of the dispersion relationship has favored the application of the local stability analysis to a plethora of problems, many of them with little connection with experiments or applications.

3.1.1. Temporal and spatial stability analyses

Most of the jets produced in microfluidic applications eventually break up, and, therefore, they are unstable in a strict sense. In this context, the adjective *stable*

means *convectively unstable*, as will be explained in the next section. In many cases, the shape of a stable (convectively unstable) jet is nearly indistinguishable from that corresponding to the base flow (unperturbed state) except close to the breakup region (Fig. 7). The fluid domain where perturbations are hardly noticeable is frequently called the *intact region*. There are certain situations in which strictly stable jets are formed; for instance, when a jet hits a downstream steady boundary condition that precludes the growth of perturbations (Fig. 7).



Figure 7: (Left) Gravitational-capillary water jet intercepted at a distance from the tap smaller than the breakup length. The jet is strictly stable. One may observe the classical small wavelength ripples formed right upstream of the interception point. (Right) The jet is intercepted beyond the breakup region, which does not alter its convectively unstable nature.

If a jet is convectively unstable, the temporal stability analysis allows one to predict the most important aspects of the breakup process. In this analysis, the growth rate ω_i is calculated as a function of the real wavenumber k and the parameters $\{\mathcal{P}_i\}$ characterizing the problem. One is typically interested in whether a certain factor (electric field, viscoelasticity, surfactant, ...) has a stabilizing or destabilizing effect. In the former case, the growth rates, the range of unstable wavenumbers and the most unstable wavenumber generally decrease, while the opposite occurs when destabilization takes place.

In the temporal stability analysis of a capillary jet,

the (dimensional) growth rate ω_i^{\max} and wavelength λ^{\max} of the most unstable mode are probably the most interesting quantities. They allow one to estimate the jet breakup length l_b and droplet diameter d_d as

$$l_b \sim V_j / \omega_i^{\max}, \quad \pi R_j^2 \lambda^{\max} \simeq \pi d_d^3 / 6, \quad (31)$$

where V_j and R_j are the jet's mean velocity and radius, respectively. In the first expression, one implicitly assumes that the perturbation responsible for the breakup is born next to the jet inception region, and that this perturbation is convected by the jet, i.e. the capillary velocity is much smaller than that of the jet. In the second expression, we take into account that the volume distribution after the jet breakup is essentially decided before nonlinear effects come into play.

Equation (31)-left has been used to calculate the breakup length of gravitational [138] and, more recently, electrified [142] jets. Equation (31)-right is the expression most commonly used to estimate the droplet diameter in the jetting regime. Castro-Hernández et al. [32] have proposed an alternative way to derive that expression, and have shown how to correct it to calculate the droplet diameter following the breakup of widening jets in the coflowing configuration.

The temporal stability approach may suggest that the breakup length should depend on the details of the ejection procedure and geometry, which are expected to play a relevant role in the excitation of the dominant capillary mode. However, both experimental and numerical results for different “smooth” ejectors indicate that the breakup length in well-controlled experimental realizations essentially depends on the liquid properties and operating parameters, which raises questions about the idea that the perturbation origin is located in the ejector. Gañán-Calvo et al. [143] have calculated the natural breakup length in terms of the transient growth of perturbations coming from the surface energy excess at the breakup [144]. This quasi-periodic source of energy may regularly feed the perturbations leading to each breakup event, which would explain the rather deterministic manner in which unforced capillary jets spontaneously break up. We will explain these results in more detail in Sec. 11.

The fact that perturbations in the temporal analysis are characterized by a real wavenumber k , implies that they grow at the same rate both in the vicinity of the nozzle and downstream. This unrealistic assumption is eliminated in the spatial stability analysis, where the complex wavenumber is calculated as a function of the real eigenfrequency. Keller et al. [145] claimed that there are spatial modes with growth rates larger than

the dominant temporal one, although they are not observed in the experiments probably because their wavelengths are too long to become established in a finite jet. However, and as explained by Eggers [28], the modes in question violate a radiation condition, and hence do not exist with proper boundary conditions at infinity. The spatial and temporal stability analyses are equivalent if the speed of the jet is much larger than that of the small-amplitude capillary waves [145].

3.1.2. The convective-to-absolute instability transition analysis

The breakup mode adopted by a fluid thread can be predicted in terms of the so-called convective-to-absolute instability transition, a concept widely used in instabilities of shear flows and wakes [146]. In convectively unstable jets, capillary waves are swept away downstream by the current, which keeps a considerable portion of the jet free of perturbations. Conversely, growing perturbations travel both downstream and upstream along absolutely unstable jets, precluding their formation.

Under certain conditions, the jetting-to-dripping transition of liquid [147, 148] and gaseous [149] jets has been successfully linked to the convective-to-absolute instability transition for axisymmetric ($m = 0$) perturbations (Fig. 8). However, and as will be explained below, we have to appeal to other instability mechanisms to explain many jetting-to-dripping transitions observed in microfluidic applications. In fact, the correspondence between convective instability and jetting is not always clear even in relatively simple cases. For example, inclined jets can suffer from self-sustained oscillations when they are convectively unstable throughout the entire fluid domain [150]. There can be significant discrepancies between the conditions leading to absolute instability and dripping in both plane liquid sheets [151] and round jets [152]. However, and despite of its limitations, the convective-to-absolute instability transition has proved to provide useful information on the relatively scarce occasions in which it has been applied.

The critical conditions leading to the convective-to-absolute instability transition are determined by the spatio-temporal analysis of the dispersion relationship (30). In this analysis, one explores the response of the system to perturbations characterized by a *complex* axial wavenumber k observed by a fixed observer anchored at the nozzle. The dispersion relationship is typically derived using the frame of reference travelling with the jet. To change the frame of reference from a travelling observer to a fixed one, one just needs to replace the wave frequency ω by $\omega' - V_j k$ in the dispersion re-

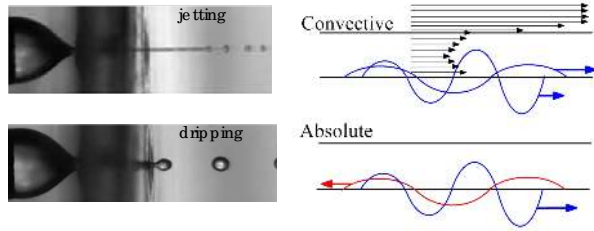


Figure 8: Relationship between the jetting-to-dripping and convective-to-absolute instability transitions. The images on the left side show the transition from jetting to dripping in gaseous flow focusing for small applied pressure drops [30]. The sketches on the right side represent the evolution of growing capillary waves in a convective and absolutely unstable jet.

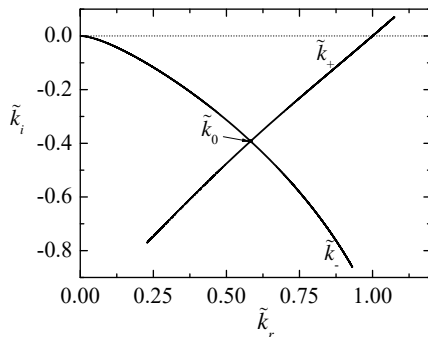


Figure 9: Spatial branches $\tilde{k}_{\pm}(\omega^*)$ for a jet moving in a vacuum [154]. These branches originated from the solution $\tilde{k}_0 = 0.5828 - 0.3921i$ and $\omega_0^* = 0.5757$ of the dispersion relation. As can be observed, the branch \tilde{k}_+ crosses the \tilde{k}_r axis at $\tilde{k}_r = 1$ (Rayleigh stability limit). Here, $\tilde{k} = kR_j$ and $\omega^* = \omega'R_j/V_j$.

lation (30). For fixed values of the control parameters $\{\mathcal{P}_i\}$ ($i = 2, \dots, N$), one calculates the critical value \mathcal{P}_{1c} for which Brigg's pinch condition [146, 153] is satisfied. This condition establishes that there must be at least one pinching of a k^+ and a k^- spatial branch with $\omega'_i = 0$, where the k^+ is the path of $\mathcal{D}_m = 0$ in the complex k plane which moves into the $k_i > 0$ half-plane as ω'_i increases, while the k^- branch always remains in the $k_i < 0$ half-plane as ω'_i increases (Fig. 9).

van Saarloos [155] proposed an alternative criterion for determining the convective-to-absolute instability transition based on the analysis of the propagation front velocity. Specifically, the system becomes absolutely unstable when the rear front velocity of a localized initial distortion becomes zero. This has been used by many researchers in capillary flows because is very intuitive and immediately understandable in physical terms. Montanero and Gañán-Calvo [156] showed the equivalence between this and the classical saddle-point criterion [146, 153].

3.2. Global stability analysis

One of the central problems in droplet-based microfluidics is to determine the parameter conditions leading to the dripping-to-jetting transition for the varied experimental configurations. In general, the existence of the jetting regime demands (i) enough mechanical energy to overcome the viscosity force and to create a large liquid-fluid interface, and (ii) the stability of the base flow sustaining the liquid ejection. This last condition involves the stability of both the fluid source and the emitted jet.

In many applications, the fluid source is a slender meniscus hanging on a feeding capillary. This fluid configuration can be seen as a simple upstream extension of the emitted jet, where the velocity field is quasi-parallel and the liquid velocity is smaller than that of the jet. Then, the system's stability essentially reduces to that of the jet, and the jetting-to-dripping transition can be explained in terms of the convective-to-absolute instability transition described above.

The above consideration does not apply to tip streaming. In this case, the source is a fluidic structure (in most cases, a cone-like meniscus) fundamentally different from the emitted jet, which can exhibit complex flow patterns including boundary layers, stagnation points and recirculation cells. In tip streaming, the jet's stability becomes a necessary but not sufficient condition for jetting. The determination of that sufficient condition requires the stability analysis of the entire base flow.

Tip streaming is not the only phenomenon which invalidates the local stability analysis. As explained above, the local spatio-temporal stability analysis is valid as long as the base flow explored by the perturbations is quasi-parallel and quasi-homogeneous in the streamwise direction (the WKBJ approximation). There are many applications where the hydrodynamic length characterizing the base flow is of the order of, or even much smaller than, that of the dominant perturbation. In this case, an accurate stability analysis of the steady base flow also requires the calculation of the so-called global modes.

Global modes are patterns of motion depending in an inhomogeneous way on two or three spatial directions, and in which the entire system oscillates harmonically with the same (complex) frequency ω and a fixed phase relation [157, 158]. This implies that space and time variables are separable when describing the system response to small-amplitude perturbations. The global modes are calculated from the ansatz

$$\Phi^{(j)}(\mathbf{r}; t) = \phi^{(j)}(r, z) e^{m\theta - i\omega t}, \quad (32)$$

where $\Phi^{(j)}$ represents any variable of the problem and m is the azimuthal mode number. The global modes (32) are calculated as the eigenfunctions of the linearized Navier-Stokes operator as applied to a given configuration (base flow). The base flow is linearly and *asymptotically* stable if the spectrum of eigenvalues is in the stable complex half-plane. In this case, any initial small-amplitude perturbation will decay exponentially on time for $t \rightarrow \infty$ (as long as the linear approximation applies). Global stability analysis has been rarely used in microfluidics, although one can expect its application to spread in the coming years [56, 109, 139, 159–163].

As mentioned in Sec. 3, capillary jets are almost always unstable because they eventually break up into droplets or suffer other types of convective instabilities. Therefore, the global stability analysis of a base flow unlimited in the downstream direction should show almost always the existence of unstable convective modes independently from the operating conditions. In practice, we set a boundary (cutoff) in the downstream direction to define the finite fluid domain considered in the analysis (Fig. 10). “Soft” boundary conditions, such as the so-called outflow or traction-free boundary condition, can be applied at that cutoff. In viscous systems, such as the liquid-liquid coflowing configuration [139, 162], global modes of convective nature can be subdominant, and the outlet boundary conditions are practically irrelevant provided that the cutoff length is much larger than the injector diameter [139, 160, 162]. For this reason, perturbations can be forced to vanish at the outlet and even so the results are accurate [159, 160, 162]. In any case, the analyzed fluid domain must contain an ejected fluid thread much longer than its diameter, and one needs to verify that the cutoff arbitrarily imposed in the analysis does not significantly affect the eigenvalues for a sufficiently large interval of jet lengths. When all the global modes of that finite system decay on time, the flow is assumed to operate in the jetting regime. On the contrary, the growth of axisymmetric ($m = 0$) modes is supposed to cause self-sustained oscillations when non-linear terms saturate the perturbation and dripping otherwise. In addition, the instability of nonaxisymmetric ($m \geq 1$) modes is assumed to produce the whipping (bending) of the emitted jet [164].

3.3. Short term response

It is frequently believed that global stability is a sufficient condition for the linear stability of the base flow. However, this is not necessarily true. If the linearized Navier-Stokes operator is non-normal, the short-term dynamics of the system can be the result of a “constructive interference” of stable global modes, which

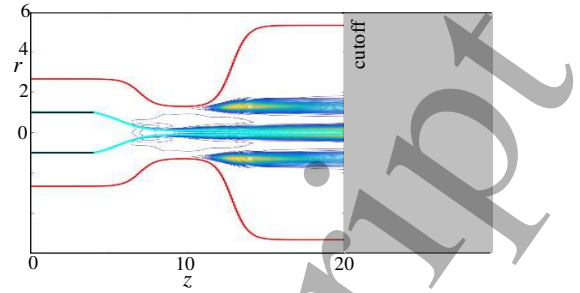


Figure 10: Energy per unit volume $e \equiv p^{(j)} + 1/2 \rho^{(j)} (|v_r^{(j)}|^2 + |v_z^{(j)}|^2)$ of the dominant eigenmode at marginal stability of a water stream focused by an air current [56]. The scalar fields $e(r, z)$ in the liquid and gas domains have been normalized with their corresponding maximum values (the maximum value in the liquid domain is around 132 that of the gas stream). Higher (lower) values of e correspond to the color yellow (blue).

can lead to a bifurcation before those modes are damped out [157, 165, 166]. In other words, the superposition of decaying small-amplitude perturbations introduced into a microfluidic configuration can destabilize the flow before those perturbations disappear, which prevents the system from reaching the jetting regime.

In the case described above, global stability becomes a necessary but not sufficient condition for jetting, and the stability analysis must be completed with direct numerical simulations of the system to examine its response to initial perturbations (the initial value problem). To speed up the calculation, the nonlinear terms can be dropped when integrating the hydrodynamic equations [56]. This allows one to see whether the superposition of linear global modes makes the resulting perturbation grow within the small-amplitude response regime. Of course, non-linear terms must be taken into account to study the subsequent evolution of that perturbation. In any case, this is a complex problem because the outcome can significantly depend on the type and location of the initial perturbation, something difficult to determine in an experiment.

The gaseous flow focusing configuration constitutes a good example of the situation described above. Cruz-Mazo et al. [56] has recently shown that there is a transient growth of linear perturbations before the asymptotic exponential regime is reached. This growth leads to dripping for small applied pressure drops. Figure 11 shows the free surface deformation at three instants for an asymptotically stable base flow. The superposition of decaying linear global modes triggered by the perturbation gives rise to the free surface pinch-off within the numerical domain.

In this section, we have described some general ideas

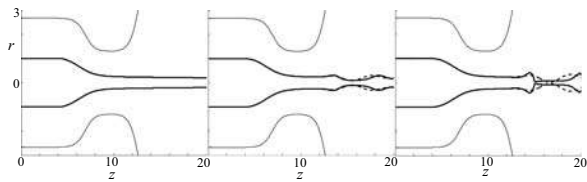


Figure 11: Free surface deformation calculated with the linearized (dash line) and nonlinear (solid line) hydrodynamic equations at three instants for an asymptotically stable base flow of gaseous flow focusing [56].

and methodological aspects of the stability analyses applied to the configurations considered in this work. In Secs. 4-7, we will show results for the convective-to-absolute instability (jetting-to-dripping) transition, and then we will describe the linear capillary instability and nonlinear breakup in the jetting regime. In this way, we first try to determine the conditions leading to jetting, and then we describe the evolution of the system in that regime. The results obtained from the global stability analysis of the microfluidic configurations considered in this review are presented in Sec. 11, once those configurations have been described in detail.

4. Results of spatio-temporal and global stability analyses

4.1. Convective-to-absolute instability transition

In the absence of viscosity effects, the convective-to-absolute instability transition of axisymmetric ($m = 0$) capillary perturbations growing along a fluid jet takes place for $V_j \approx \bar{V}_\sigma$ [154, 167], where V_j is the jet velocity, $\bar{V}_\sigma = [\sigma/(\bar{\rho}R_j)]^{1/2}$ is the inertio-capillary speed, and $\bar{\rho}$ is an effective density of the jet-environment ensemble. This result has a straightforward interpretation: for $V_j \gtrsim \bar{V}_\sigma$ the liquid sweeps away the growing capillary waves that swim against the current at a speed of the order of \bar{V}_σ .

The effective density $\bar{\rho}$ for a liquid jet surrounded by a gaseous ambient is essentially that of the jet. When the jet is directly extruded from a nozzle by the action of the upstream pressure, the condition $V_j \gtrsim \bar{V}_\sigma$ is generally satisfied because it coincides with $\rho_j V_j^2 \gtrsim \sigma/R_j$, which is a necessary condition for the jet extrusion. Therefore, absolute instability does not generally constitute an obstacle for the jet formation in this simple application.

The effective density $\bar{\rho}$ for gaseous jets moving in liquid baths is much smaller than that for the inverse case. Therefore, higher jet velocities are demanded to enable

convective instability in gaseous jets, which partially explains why is so difficult to produce them. In fact, direct injection of a gas into a quiescent pool of liquid has produced long jets only in the supersonic regime [168]. Long gaseous threads can be formed for lower injection velocities with the help of surfactants or mixtures reducing the surface tension [149, 169], and in the presence of a solid substrate/core [170, 171].

As explained in Sec. 3, the parameter surface corresponding to the convective-to-absolute instability transition for a specific configuration can be accurately determined by conducting the spatio-temporal analysis of the dispersion relationship derived from the linear stability analysis. This is a relatively complex calculation for capillary systems, which may explain why its use has not sufficiently spread in this context [172]. Leib and Goldstein [167] studied the absolute instability of a jet in a mechanically inert ambient, while Lin and Lian [173] took into account the effect of the surrounding medium. Subsequently, more complex configurations have been considered by several authors, including the effect of a small inner-to-outer density ratio [149, 174], a viscous coflowing current [31, 175, 176], confinement in various geometries [148, 177], jet swirling [178], a twofold interface [179, 180], viscoelasticity [179–181], and gravity [181] among others. In many cases, the dispersion relationship can be derived analytically, while in others the linearized equations are spatially discretized.

Figure 12 shows the curves V_j/V_σ corresponding to the convective-to-absolute instability transition for a liquid jet moving as solid body in a bath coflowing with the jet at the same velocity [154, 167]. Here, $V_\sigma = [\sigma/(\rho_j R_j)]^{1/2}$ is the inertio-capillary velocity defined in terms of the jet density ρ_j . The results were calculated for different values of the density and viscosity ratios, $\rho = \rho_o/\rho_j$ and $\mu = \mu_o/\mu_j$, where ρ_o and μ_o stand for the outer bath density and viscosity, respectively, while μ_j is the jet viscosity. The velocity ratio V_j/V_σ is represented as a function the jet Reynolds number

$$\text{Re}_j = \frac{\rho_j V_j R_j}{\mu_j}. \quad (33)$$

The figure also shows the ratio of V_j to the capillary-viscous velocity $V_\mu = \sigma/\mu_j$, which is the relevant characteristic quantity in the Stokes limit $\text{Re}_j \rightarrow 0$. The velocity ratios V_j/V_σ , V_j/V_μ and V_μ/V_σ are essentially the jet's Weber, Capillary and Ohnesorge numbers, respectively:

$$\text{We}_j = \left(\frac{V_j}{V_\sigma} \right)^2, \quad \text{Ca}_j = \frac{V_j}{V_\mu}, \quad \text{Oh}_j = \frac{V_\sigma}{V_\mu}. \quad (34)$$

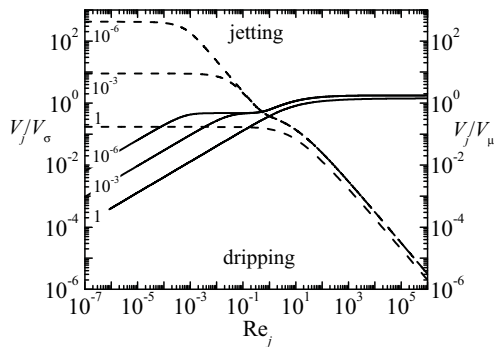


Figure 12: V_j/V_σ (solid lines) and V_j/V_μ (dashed lines) corresponding to the convective-to-absolute instability transition for a liquid jet moving with a uniform velocity in a fluid bath coflowing at the same [154]. The labels indicate the values of ρ . In all the cases, $\rho = \mu$.

As can be observed in Fig. 12, the critical ratios V_j/V_σ and V_j/V_μ reach constant values in the inviscid and viscous limits, respectively. In the former case, these values are similar for the liquid-gas and liquid-liquid systems. In the latter case, this threshold does not depend on the jet's radius, which means that infinitely thin jets can be formed (the so-called *unconditional jetting*) [182] provided that their velocities are larger than $K(\mu)V_\mu$, where the function $K(\mu)$ is expected to take values of order unity. The viscous limit must be taken with caution, because the effects of the outer medium cannot be neglected in that case even for very small density and viscosity ratios [174, 183].

Gañán-Calvo [182] realized that, in the Stokes limit, the convective-to-absolute instability transition does not depend on the jet and outer medium velocity profiles, but only on the interface speed V_s . In addition, the function $K(\mu)$ approximately scales as $\mu^{1/2}$. These results suggest expressing the instability transition in terms of the modified Capillary number

$$\overline{Ca} \equiv \mu^{1/2} \mu_j V_s / \sigma. \quad (35)$$

In a viscosity-dominated flow, a jet is convectively unstable if the interface velocity V_s is such as $\overline{Ca} \gtrsim \overline{Ca}^*$, where \overline{Ca}^* depends on the viscosity ratio μ and lies in the interval $0.14 \lesssim \overline{Ca}^* \lesssim 0.4$ [182].

The comparison with experimental data has shown that the analysis of the convective-to-absolute instability transition constitutes an accurate predictive tool provided that both the properties of the fluids involved and the base flow are correctly accounted for [30, 148, 149, 182, 184, 185]. However, it must be pointed out again that this analysis considers only the stability of the emitted jet. In general, and as mentioned above, the system's

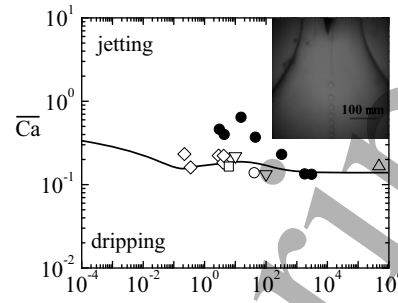


Figure 13: Modified Capillary number $\overline{Ca} \equiv \mu^{1/2} \mu_j V_s / \sigma$ below which a jet becomes absolutely unstable [40]. The line indicates the convective-to-absolute instability transition when the flow is dominated by viscosity [182]. Experimental values for the jetting-to-dripping transition (symbols). The data were taken from Acero et al. [40] (\bullet), Anna et al. [19] (\square), Anna and Mayer [186] (\circ), Utada et al. [187] (∇), Guillot et al. [148] and Herrada et al. [188] (\diamond), and Gañán-Calvo et al. [149] (\triangle). The inset shows a liquid-liquid viscosity-dominated jetting realization in a flow focusing device [40].

stability condition is twofold: the fluid source must be stable and the emitted jet must be convectively unstable.

Figure 13 shows the critical Capillary number \overline{Ca}^* below which a jet becomes absolutely unstable when the flow is dominated by viscosity [182]. The figure also shows the experimental values of that parameter measured in different microfluidic configurations at the jetting-to-dripping transition. The experimental value significantly exceeded the theoretical prediction in some cases, which probably means that the jetting-to-dripping transition was caused by the liquid source instability. Figure 14 also shows that convective instability is a necessary but not a sufficient condition to produce the cone-jet mode of electrospraying [109] or the steady jetting of gaseous flow focusing [183]. The convective-to-absolute instability transition curve calculated by Leib and Goldstein [167] overestimates the critical Reynolds number for very large and very small values of this parameter probably due to the existence of an inner boundary layer [33] and a gaseous environment [40] in flow focusing, as well as by electric field effects in electrospray.

The results described above refer to the convective-to-absolute instability transition for axisymmetric perturbations. As will be explained in more detail in Sec. 6, the mismatch between the jet and outer bath velocities, as well as the existence of free electric charges accumulated at the interface and subjected to strong electric fields, may make nonaxisymmetric perturbations grow despite the stabilizing effect of the surface tension (the so-called whipping instability). Experience shows that

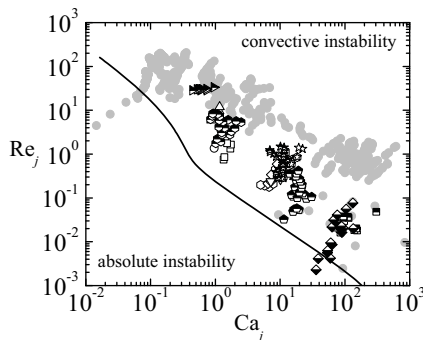


Figure 14: Capillary Ca_j and Reynolds Re_j numbers of jets produced with electrospray (open and grey symbols) [109] and gaseous flow focusing (half black symbols) [40]. The open and half black symbols correspond to steady jetting experiments where the flow rate was decreased down to the stability limit. The line corresponds to the convective-absolute instability transition for a non-electrified jet moving in a vacuum [167].

the capillary jets emitted in almost all microfluidics applications are either stable or at most convectively unstable when it comes to nonaxisymmetric perturbations. The lateral jet oscillations frequently observed in configurations like electrospray or flow focusing do not generally propagate upstream, and, therefore, they do not alter the tapering meniscus stability. Absolute whipping has been observed only in liquid jets focused by high-speed gaseous currents inside converging nozzles [189]. In fact, it seems that the gaseous radial flow in front of the discharge orifice of the original flow focusing configuration [18] constitutes a barrier for whipping perturbations. The conditions leading to absolute whipping have been barely studied [190].

4.2. Global stability

Global stability analyses have been frequently conducted to study problems such as wakes behind solid obstacles and detached single-phase flows [157, 158]. These studies are more scarce in the context of capillary systems. Here, we mention those related with the microfluidic configurations considered in this review. We will come back to these studies in Sec. 11.

Dizes [152] examined the global modes in falling capillary jets and discussed the relationship between global instability and the jetting-to-dripping transition. Sauter and Buggisch [159] carried out a global stability analysis of a gravitational jet using the long-wave (1D) approximation (see Sec. 2.4). The results for marginal stability and critical frequencies were in excellent agreement with direct numerical simulations. Rubio-Rubio et al. [161] showed the stabilizing effect of the axial curvature from the 1D model too.

Gordillo et al. [139] studied with the slender-body approximation the global stability of the tip streaming flow produced by a coflowing injector (see Sec. 9). The global stability of the axisymmetric flow produced in the coflowing configuration has recently been examined by Augello et al. [162]. For high external flow rates, the predictions almost coincide with those of the local convective-to-absolute instability transition theory [188]. However, the flow is slightly more stable than predicted by the local analysis for small external flow rate and/or a high degree of confinement.

As will be explained in Sec. 9, in the steady cone-jet mode of electrospray very thin jets are produced by tip streaming when strong electric fields are applied to low-conductivity droplets. Theoretical studies on the steady cone-jet mode of electrospray typically use the leaky-dielectric model [20, 101] (see Sec. 2), i.e. they assume that the liquid exhibits a uniform electrical conductivity (the Ohmic conduction model), and the net free charge accumulates onto the free surface so that the bulk electrostatic mass force is negligible as compared to the superficial one resulting from the Maxwell stresses [104, 106–108, 191, 192]. Dharmansh and Chokshi [193] studied the semi-global linear stability of the electrospray cone-jet mode with the 1D approximation. They subsequently extended this analysis to electrospinning by incorporating rheological effects described by the Olroyd-B and XPP models [194]. Ponce-Torres et al. [109] have calculated the minimum flow rate of the cone-jet mode of electrospray from the global stability of the solution to the 2D leaky-dielectric model, showing good agreement with experiments. Blanco-Trejo et al. [163] have recently extended this analysis to weakly viscoelastic liquids. The cone-jet mode of electrospray can be stabilized with a coflowing high-speed gas current [195]. The experimental minimum flow rates reasonably agree with the global stability predictions in this case as well [195].

In flow focusing (see Sec. 9), tip streaming is achieved with purely hydrodynamic means by making the focused fluid cross the discharge orifice together with an outer (focusing) gas/liquid current. Cruz-Mazo et al. [56] examined the global stability of the gaseous flow focusing axisymmetric configuration. They found good agreement with experimental values of the minimum liquid flow rate for sufficiently large gas velocities.

As explained in Sec. 3, linear *asymptotic* global stability does not necessarily imply linear stability. If the linearized Navier-Stokes operator is non-normal, then the perturbation energy may increase during the system's short-term response, and cause the solution bifur-

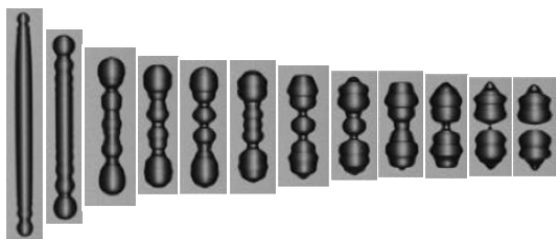


Figure 15: End-pinching in a liquid thread [201]. The thread aspect ratio is close to the critical value below which the thread recoils without breaking up.

cation in asymptotically stable systems. In fact, convective instabilities commonly arising in problems with inflow and outflow conditions are not typically dominated by long-term modal behavior. For instance, asymptotically stable gravitational jets eventually break up due to the growth of non-normal modes [166]. Cruz-Mazo et al. [56] have shown that flow focusing stability can be explained in terms of the system's short-term response for small gas velocities.

5. Capillary instabilities

In the jetting regime, the dispersed phase forms a cylindrical thread long compared with its diameter, which breaks up downstream into a collection of droplets/bubbles. This breakup can be due to the so-called end-pinching mechanism [196], the Rayleigh capillary instability [197], or a combination of both. In all the cases, the instability is triggered by interfacial energy release.

5.1. End-pinching instability

Liquid threads are produced in technological and natural processes such as DOD ink jet printing, crop spraying and atomization coating, or the fragmentation taking place in fountains and many types of sprays [62]. For sufficiently large values of the capillary Reynolds number and the thread aspect ratio, the free surface pinches off at the ends of the thread [196, 198–202], which results in a set of droplets (Fig. 15). This is the so-called end-pinching mechanism. Although the breakup is also driven by surface tension, this process and the Rayleigh capillary instability are clearly distinct.

The end-pinching phenomenon also occurs in a jet when it moves at speeds close to that of the jetting-to-dripping transition. In this case, the jet Weber number We_j takes values around unity, and the liquid inertia hardly overcomes the resistant force exerted by surface tension. In the end-pinching breakup of a jet, a bulb

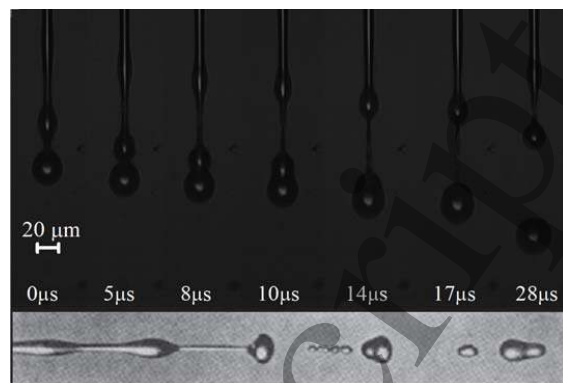


Figure 16: (Upper images) End-pinching in a jet emitted close to the minimum flow rate stability limit of electrospray [109]. (Lower image) The Rayleigh instability in a millimeter jet [203].

forms at the end of the jet. This bulb moves slower than the fluid in the thread located just behind it. For this reason, the fluid gets into the bulb and inflates it. The neck located between the bulb and the thread stretches due to the capillary pressure and becomes thinner and thinner until a droplet separates from the jet. Two bulbs can form simultaneously in a jet. When the jet is accelerated under the action of an external force, the rear bulb may catch the lead one, giving rise to the coalescence between them (Fig. 16).

5.2. Rayleigh instability

The Rayleigh capillary instability can be explained as follows. When the interface of a cylindrical fluid thread is perturbed with an infinitesimal sinusoidal deformation, the surface tension produces an axial pressure gradient in the thread. If the perturbation wavelength is larger than the thread perimeter, the pressure decreases/increases in the bulging/narrowing region, which favors the growth of that perturbation. The capillary wave breaks the interface, which gives rise to a quasi-monodisperse collection of droplets. Owing to mass conservation, the droplet diameter can be calculated as $d_d \approx 3/2 (R_j \lambda^{\max})^{1/3}$ [Eq. (31)-right], where λ^{\max} is the wavelength of the perturbation with the maximum growth rate, and, therefore, responsible for the jet breakup.

The phenomenon described above becomes the dominant breakup mechanism for well-established jetting realizations. In the absence of external actuation and viscosity forces, a jet moving in a still ambient breaks up owing to the Rayleigh capillary instability if [204]

$$We_j \gtrsim 4 \quad \text{and} \quad We_g \equiv \rho We_j \lesssim 0.2, \quad (36)$$

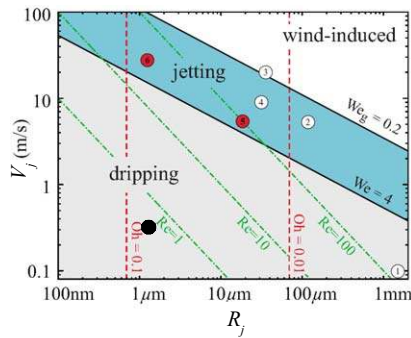


Figure 17: Breakup regimes for jets of pure water moving in still air [205]. The encircled numbers (1)-(4) refer to droplet formation studies performed by Ambravaneswaran et al. [206], Kalaaji et al. [207], González and García [208] and Pimbley and Lee [209], respectively, while the encircled numbers (5) and (6) refer to the diminutive Rayleigh jets produced by van Hoeve et al. [205]. The black circle corresponds to a 500-cSt silicone oil jet with $R_j = 1.5 \mu\text{m}$ and $V_j = 0.37 \text{ m/s}$ [183]. In this figure, Re , We and Oh correspond to the symbols Re_j , We_j and Oh_j defined in this review, respectively.

where ρ is the ratio of the ambient density to that of the jet. The first and last condition eliminates the possibility of dripping and whipping (wind-induced instability), respectively. Figure 17 shows the different breakup regimes for jets of pure water moving in still air.

An outer coflowing stream reduces the value of the Weber number above which Rayleigh capillary instability can be observed. In fact, this breakup mechanism can be found in viscous jets coflowing with high-speed gaseous streams for Weber numbers as low as 0.1 [183].

5.3. Rayleigh stability analysis

As explained in Sec. 3, the temporal linear stability analysis of the jetting mode leads to the dispersion relationship which determines the continuum spectrum of eigenfrequencies characterizing the axisymmetric normal modes (Fourier components) as a function of their (real) wavenumbers [210]. The decomposition of initial (spontaneous) perturbations into linear eigenmodes has proved to be useful for studying the short-term evolution of those perturbations. The local stability analysis (WKB approximation) assumes that the base flow is quasi-parallel and homogeneous in the streamwise direction over distances of the order of or larger than the perturbation wavelength. This approach has been and still is routinely applied to analyze the influence of all types of effects, on many occasions with very little connection with experiments due to the failure of the locality approximation. Nevertheless, it allows one to identify the stabilizing and destabilizing mechanisms that affect the Rayleigh instability.

Rayleigh's linear stability analysis [197] was based on three major simplifications: the jet moves uniformly, its viscosity has little influence, and the dynamical effects of the environment can be neglected. It predicts that the growth rates are imaginary numbers, which indicates that disturbances are convected downstream with the base flow velocity V_j . The maximum growth rate ω_i^{\max} is of the order of the inverse of the inertio-capillary time

$$\hat{t}_{ic} = (\rho_j R_j^3 / \sigma)^{1/2}, \quad (37)$$

which means that the jet breakup time scales as \hat{t}_{ic} . Therefore, the distance covered by the dominant perturbation before breakup is of the order of $V_j \hat{t}_{ic}$. The wavelength of the dominant perturbation is $\lambda_R^{\max} \approx 2.9\pi R_j$. These predictions have shown to be fairly accurate in many experiments with capillary jets [62, 208].

Rayleigh's basic analysis has finely been tuned to account for various additional effects, such as the existence of a shear boundary layer on the inner side of the interface [211], viscous damping [212], a non-negligible fluid environment [62], surfactants [213], viscoelasticity [214], electric effects [215–217], etc. These factors can be grouped into two categories: destabilizing and stabilizing. Typically, destabilizing factors increase the perturbation growth rates over the whole spectrum, the most unstable wavenumber and the range of unstable wavenumbers, while stabilizing factors produce the opposite effects. This has important practical implications because, according to Eqs. (31), destabilizing factors reduce not only the jet breakup length but also the size of the resulting droplets.

There are numerous studies on the temporal stability of jets that consider different effects and combinations of them. In this section, we will review those related to the microfluidic configurations considered in this work.

5.4. Boundary layer and viscosity effects

The mismatch between the velocities of a liquid jet and the surrounding gaseous medium significantly alters both the liquid and gas velocity profiles for large enough Weber numbers. The consideration of realistic velocity distributions unveils unstable non-axisymmetric modes that do not appear in the stability analysis of inviscid parallel and uniform streams. Those distributions are essential to explain atomization experiments at large enough Weber numbers [218].

Gañán-Calvo et al. [211] have analytically shown that a shear boundary layer on the inner side of the interface can be regarded as a destabilizing factor for distances from the boundary layer origin of the order of the jet's radius. For longer distances, the boundary layer does

not affect the jet's stability, and Rayleigh's dispersion relation is recovered. Figure 18 shows the growth rate as a function of the wavenumber for different values of the modified Weber number $We_s = (1 - V_s/V_j)^2 We_j$. The limit $We_s \rightarrow 0$ ($V_s/V_j \rightarrow 1$) corresponds to a vanishing boundary layer. The growth rate converges to that of the Rayleigh mode in that limit. These results suggest that the inner boundary layer growing in, for instance, gaseous flow focusing can decrease the droplet size and the distance between two consecutive droplets.

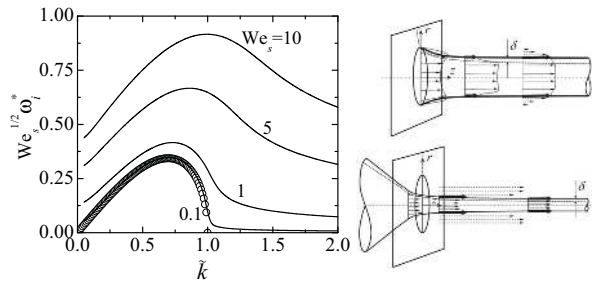


Figure 18: Temporal growth rate ω_i^* as a function of the (real) wavenumber \tilde{k} for $We_s = 0.1, 1, 5$, and 10 (and the additional constraint $\delta = Re_j^{-1/2}$) [211]. The circles correspond to Rayleigh's dispersion relation. Here, $\omega_i^* = \omega_i R_j / V_j$ and $\tilde{k} = k R_j$. The sketches on the right-side of the figure show two situations (discharge in a still ambient and flow focusing) where these results apply [211].

For large enough viscosities, radial diffusion of momentum ensures a quasi-uniform jet velocity profile right behind the nozzle. Jets moving with that velocity profile can be described from the Lagrangian frame of reference solidly moving with the jet. In this case, the velocity V_j no longer enters the problem, and viscous effects are quantified by the Ohnesorge number $Oh_j = \mu_j(\rho_j \sigma R_j)^{-1/2}$ [Eq. (34)]. Figure 19 shows the influence of this parameter on the temporal growth rate. As can be seen, both the perturbation growth rate and the most unstable wavenumber decrease as the Ohnesorge number increases, which shows the stabilizing effect of viscosity [212]. The maximum value $k = R_j^{-1}$ of unstable wavenumbers is not affected by this property. For viscous liquid jets, the growth factor scales with the inverse of the viscous-capillary time

$$\hat{t}_{vc} = \mu_j R_j / \sigma. \quad (38)$$

These results indicate that viscosity can significantly increase the droplet size and the distance between two consecutive droplets produced in jetting realizations.

When a liquid jet is ejected into a still gaseous ambient, the latter has little influence on the jet's stability under axisymmetric perturbations even for moderately

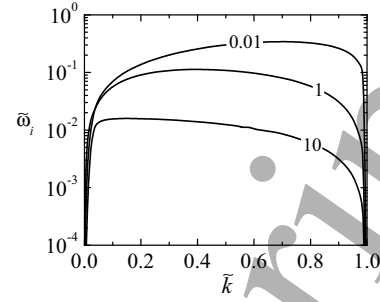


Figure 19: Temporal growth rate $\tilde{\omega}_i$ as a function of the wavenumber \tilde{k} for $\rho = \mu = 10^{-4}$ and different values of Oh_j as indicated by the labels [154]. Here, $\tilde{\omega}_i = \omega_i \hat{t}_{ic}$ and $\tilde{k} = k R_j$.

large Weber numbers. González and García [208] accurately measured the temporal growth rates of moderately viscous capillary jets emitted in a still atmosphere. The experimental data exhibited remarkable agreement with theoretical predictions calculated by translating spatial analysis [167] results into the temporal variables (Fig. 20).

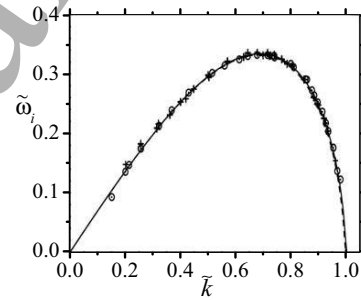


Figure 20: Temporal growth rate $\tilde{\omega}_i$ as a function of the wavenumber \tilde{k} [208]. The crosses and circles correspond to experimental results measured with the breakup time and amplitude-evolution method, respectively. The solid line is the theoretical predictions for $Oh_j = 0.021$ and $We_j = 59$, while the dashed line was calculated without the surrounding air effect. Here, $\tilde{\omega}_i = \omega_i \hat{t}_{ic}$ and $\tilde{k} = k R_j$.

5.5. Confinement effects

The stability of confined capillary jets is of great interest at both fundamental and practical levels, especially in channels with noncircular cross-sections, which are commonly used in microfluidics [219]. Cubaud and Mason [220] showed experimentally that the presence of external walls delays the breakup of liquid threads coflowing with an outer stream, and significantly increases the wavelength of the most unstable mode. In fact, capillary instability can be completely suppressed in a channel with a rectangular cross-section (Fig. 21) [221].

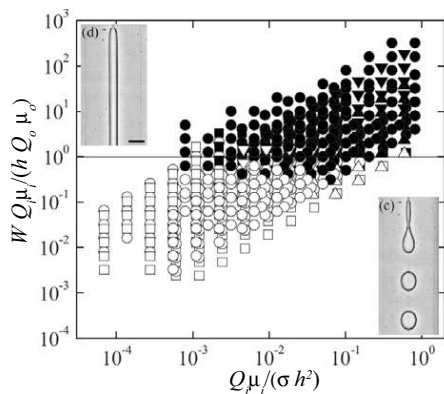


Figure 21: Stable jets (open symbols) and unstable jets or dripping (solid symbols) produced in a coflowing liquid-liquid configuration inside a rectangular channel of width W and height h [221]. Q_i and Q_o are the inner and outer flow rates, while μ_i and μ_o stand for the inner and outer viscosities, respectively.

Most theoretical works on the stability of confined capillary jets have considered the circular geometry [148, 177, 222, 223]. Hickox [222] studied analytically the stability of the pressure-driven jet in a tube for infinitely small wavenumbers. He found that the flow was unstable under axisymmetric perturbations in all the cases considered. The same conclusion can be derived from the spatio-temporal stability analysis of Guillot et al. [148] and Guillot et al. [177]. Using the approach of Hickox [222], Kashid et al. [223] found certain parameter conditions for which a jet confined in a circular tube becomes stable.

Janssen et al. [224] studied numerically the growth of small-amplitude varicose perturbations in jets flowing between parallel surfaces. Confinement did not completely stabilize the jet in any of the cases considered. A recent temporal stability analysis [225] suggests that a jet sliding over the channel wall is unconditionally stable, while a detached liquid thread can be stable only for very small distances between the interface and the wall, and sufficiently high viscosities or small enough interfacial tensions.

Overall, one can state that confinement inhibits capillary instabilities in microfluidic devices. Breakup takes place essentially by quasi-static mechanisms [36], which facilitates the control of the size and morphology of the produced fluidic entities.

5.6. Compound jets

Compound jets consist of an inner fluid surrounded by a liquid shell, both moving coaxially at the same velocity [180, 226, 227]. Their breakup results in compound drops whose morphology can be controlled by

adjusting the diameters and velocities of the inner and outer jets [18, 228]. The linear stability analysis of compound jets reveals the existence of the stretching and squeezing unstable modes, which correspond to an in-phase and out-of-phase deformation of the inner and outer interfaces, respectively [180, 226, 227, 229]. The stretching and squeezing modes are mainly driven by capillary forces at the inner and outer interfaces, respectively. The stretching mode dominates the breakup process because its maximum growth rate is larger than that of the squeezing mode [180, 226, 227]. The growth rates of the stretching mode match those calculated by Tomotika [212] when the radius of the outer jet takes sufficiently large values [227].

5.7. Viscoelasticity effects

Viscoelasticity is frequently quantified using the Oldroyd-B model [63], which provides reasonably accurate predictions while keeping certain simplicity [65] for Boger fluids. These fluids are dilute polymer solutions in viscous and low-viscosity solvents that hardly exhibit shear-thinning [59]. Non-Newtonian effects in an Oldroyd-B liquid are quantified by the stress relaxation and retardation times λ_s and λ_r , respectively (see Sec. 2).

Viscoelasticity has a destabilizing effect on relaxed jets: the axisymmetric capillary mode grows in a viscoelastic jet faster than in a Newtonian one with the same Ohnesorge number owing to the apparent shear thinning associated with elasticity [230–234]. This destabilizing effect translates into an increase of the minimum Weber number leading to convective instability [156]. These results have relatively little consequences at the practical level because viscoelastic stress is relaxed in the base flow of few applications.

The stretching suffered by the polymers in some microfluidic devices [67, 235–237] produces an unrelaxed axial stress in the emitted jet. Macromolecules are arranged along the axis of the thin emitted viscoelastic jets, which hinders their relaxation to the coiling state once the external elongational stresses have disappeared. The unrelaxed stress significantly reduces the growth rate of the varicose mode [214, 238] (Fig. 22). This effect explains the stability of long viscoelastic threads extruded in, for instance, electrospinning [77] or flow focusing [237]. Micrometer filaments with lengths up to 1 cm and Weber numbers of the order of 10^{-4} were formed in front of the discharge orifice of a gaseous flow focusing device [236], while extremely long threads were produced behind that orifice with relatively low polymer concentrations [237]. It must be noted that the

unrelaxed axial stress increases the speed at which capillary waves move over the jet's surface [239], which favors absolute instability despite the reduction of the growth rates [238].

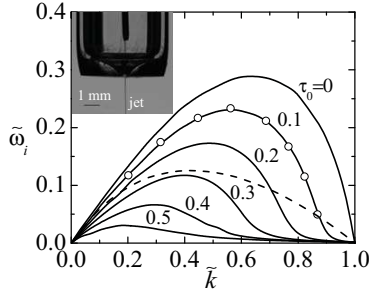


Figure 22: Temporal growth rate $\tilde{\omega}_i$ as a function of the wavenumber \tilde{k} for the stress relaxation time $\tilde{\lambda}_s = 100$, the retardation time $\tilde{\lambda}_r = 10$, the Ohnesorge number (defined in terms of the Newtonian viscosity) $Oh_j = 0.849$, and different values of the unrelaxed axial stress τ_0 [238]. The circles correspond to the solution obtained by Goren and Gottlieb [214] for $\tau_0 = 0.1$. The dashed line is the solution for a Newtonian jet ($\tilde{\lambda}_s = \tilde{\lambda}_r = \tau_0 = 0$). All the quantities have been made dimensionless with R_j , the inertio-capillary time (37) and capillary pressure σ/R_j , i.e. $\tilde{k} = kR_j$, $\tilde{\omega}_i = \omega_i \hat{t}_{ic}$, $\tilde{\lambda}_s = \lambda_s / \hat{t}_{ic}$ and $\tilde{\lambda}_r = \lambda_r / \hat{t}_{ic}$. The inset shows a microjet of a polyacrylamide aqueous solution at a concentration of 1000 ppm produced with gaseous flow focusing [236, 237].

5.8. Electrified jets

The stability analysis of electrified jets involves both the relative electrical permittivity and dimensionless electric relaxation time,

$$\varepsilon = \frac{\varepsilon_j}{\varepsilon_o}, \quad \tau_{ej} = \frac{\varepsilon_j}{K_j \hat{t}_{ic}}, \quad (39)$$

where ε_j and ε_o are the electrical permittivity of the liquid jet and outer medium, respectively, and K_j is the jet electrical conductivity. The perfect conductor and dielectric limits correspond to $\tau_{ej} \rightarrow 0$ and $\tau_{ej} \rightarrow \infty$, respectively. In the absence of an externally applied electric field, electric effects are accounted for by the Taylor number

$$\Gamma_e = \frac{R_j \varepsilon_o E_{on}^2}{\sigma}, \quad (40)$$

which measures the electric normal stress $\varepsilon_o E_{on}^2$ in terms of the capillary pressure σ/R_j . Here, E_{on} stands for the normal electric field on the outer side of the interface and produced by the surface charge density σ_e . In the absence of an inner electric field ($\tau_{ej} \rightarrow 0$), $E_{on} = \varepsilon_o \sigma_e$. If the jet is subjected to the action of an external electric field (like in electrospray), this last effect is quantified

through the dimensionless electric strength

$$\mathcal{E}_j = \frac{R_j \varepsilon_o E^2}{4\pi\sigma}, \quad (41)$$

where E is the axial/radial electric field intensity.

Linear stability analyses consistently show that both the surface charge and the externally applied DC radial electric field destabilize the jet by increasing the maximum growth rate and most unstable wavenumber [216, 240]. These factors also increase the minimum Weber number for convective instability [80]. These effects can be explained in terms of an increase of the effective surface tension produced by the electric normal stress. The opposite occurs when axial electric fields are applied on both conductor [241–243] and dielectric [242, 243] liquids (Fig. 23). In this case, the electric field stabilizes the jet. As will be explained in Sec. 12, these results have been used to calculate the breakup length in electrospray [142].

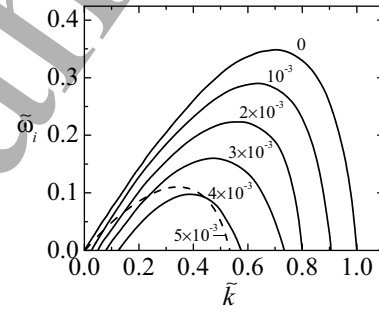


Figure 23: Temporal growth rate $\tilde{\omega}_i$ as a function of the wavenumber \tilde{k} for a conductor ($\tau_{ej} = 0$) inviscid jet with $\varepsilon = 78$ (solid lines) in an axial electric field [244]. The dashed line shows the results for the dielectric case ($\tau_{ej} = \infty$). The labels indicate the values of the electric strength \mathcal{E}_j . Here, $\tilde{\omega}_i = \omega_i \hat{t}_{ic}$ and $\tilde{k} = kR_j$.

The leaky-dielectric (low-conductivity) jet subject to an axial electric field is the most interesting configuration for the study of the electrospray cone-jet mode. In a leaky-dielectric jet, the surface charge evolves trying to screen the external electric field to eliminate the inner one. Saville [244] showed that this surface charge relaxation makes disturbances grow in an oscillatory manner, contrary to what happens in either perfect dielectrics or perfect conductors. The interaction between the electrical and viscous stresses at the electrohydrodynamic boundary layer next to the interface of nearly-inviscid threads can destabilize both asymmetric and axisymmetric perturbations (Fig. 24). Mestel [245, 246] derived the dispersion relationships corresponding to the low- and high-viscosity limits. However, the dependency of the temporal growth rates on the parameters of

the problem has not been explored for arbitrary viscosity values. The temporal stability analysis of a charged, leaky-dielectric, Oldroyd-B jet under an axial electric field shows that both the electric field [247] and the axial polymeric stress of the base state [248] inhibit the axisymmetric mode.

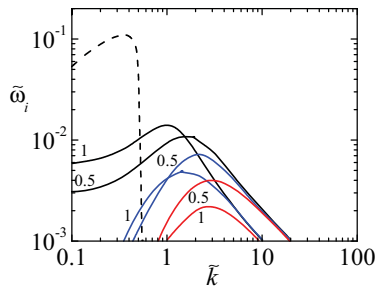


Figure 24: Temporal growth rate $\tilde{\omega}_i$ as a function of the wavenumber \tilde{k} for an inviscid jet with $\varepsilon = 78$ in an axial electric field of intensity $\mathcal{E}_j = 5 \times 10^{-3}$ [244]. The labels indicate the values of the electric relaxation time τ_{ej} . The dashed line corresponds to the dielectric case ($\tau_{ej} = \infty$). The black, blue and red lines correspond to the modes $m = 0, 1$ and 2 , respectively. Here, $\tilde{\omega}_i = \omega_i \hat{t}_{ic}$ and $\tilde{k} = kR_j$.

5.9. Surfactant effects

When the jet interface is loaded with a monolayer of a surface-active molecule (surfactant), both the outwards surfactant convection and the dilatation of the interface element make the surfactant surface density decrease in the necking region. This surfactant depletion increases the surface tension in that region, which causes Marangoni convection in the opposite direction. Marangoni convection gives rise to additional energy dissipation, which reduces the growth rates of the linear capillary oscillations.

In many microfluidic applications, the characteristic time of surfactant adsorption/desorption is much greater than the droplet production time, and surfactant solubility can be neglected at least in part of the process. As explained in Sec. 2, this approximation reduces significantly the dimension of the parameter space, which makes the problem more tractable [213, 249]. Figure 25 shows the temporal growth rate as a function of the wavenumber for a liquid thread loaded with an insoluble surfactant characterized by its elasticity $\beta = -(\Gamma_0/\sigma_0) d\sigma/d\Gamma|_{\Gamma=\Gamma_0}$ (Γ_0 and $\sigma_0 = \sigma(\Gamma_0)$ are the initial surfactant surface density and surface tension, respectively). The growth rate decreases as the surfactant elasticity (strength) increases [213]. As can be seen, \tilde{k}_{\max} does not depend monotonically on β .

The opposite limit to the insolubility case considered above is that in which the surfactant transport between

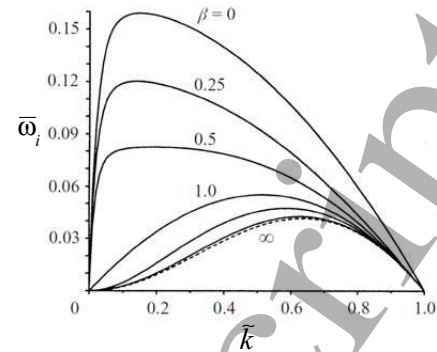


Figure 25: Temporal growth rate $\tilde{\omega}_i$ as a function of the wavenumber \tilde{k} for $Oh_j = 10$ and different values of the surfactant elasticity β [213]. Here, $\tilde{\omega}_i = \omega_i \hat{t}_{vc}$ and $\tilde{k} = kR_j$.

the interface and the bulk fluids is diffusion-limited (see Sec. 2). In this case, the stabilizing effects of surfactants are similar to those described for the insoluble one [250].

5.10. Relationship with the convective-absolute instability transition

One may think that the destabilizing factors described above necessarily increase the critical Weber numbers leading to the convective-to-absolute instability transition, while the stabilizing elements produce the opposite effect. This is so in most cases (see, e.g., Refs. [80, 156, 251]). However, there are two notable exceptions to this rule. The existence of a boundary layer on the inner side of the interface makes that surface “slip” over the jet’s inviscid core. This favors the motion of capillary waves in the current direction, which delays the jetting-to-dripping transition [211, 252]. The opposite situation arises in unrelaxed viscoelastic jets [238]. The speed at which growing waves travel over these jets increases with the elastic axial stress [239]. One may expect that if this stress, measured in terms of the dynamic (convective) pressure, exceeds a certain threshold, then the jet will fail to sweep downstream those waves (absolute instability). This explains the simultaneous reduction of the growth rates (Fig. 22) and the increase of the critical Weber numbers due to the unrelaxed stress [238].

5.11. Modulated capillary instability

In many jetting applications, there is a window of operational conditions within which the dependence of the perturbation growth rate on the wavelength exhibits a

sharp maximum. This constitutes a “natural wave filter” for the dominant perturbation, which favors the production of monodisperse collections of droplets. When this situation does not occur, external stimuli can be applied to trigger and control the jet breakup, which allows one not only to select the droplet diameter but also to narrow the size distribution. For instance, in continuous inkjet systems, the jet is broken into drops inside a chamber through a pulse produced by a piezoelectric crystal. The resulting droplets are electrically charged, expelled from a printhead nozzle, and positioned on the substrate by appropriately setting their speed and charge. A similar idea has been applied, for instance, to the axisymmetric gaseous [253] and liquid-liquid [254] flow focusing (Fig. 26), or to the bubble formation in forced co-axial air-water jets [255]. Pulsed stimulation can produce the detachment of a single drop or a group of drops in the middle of the jet [256]. The position and number of the drops can be controlled by adequately selecting the pulse parameters.

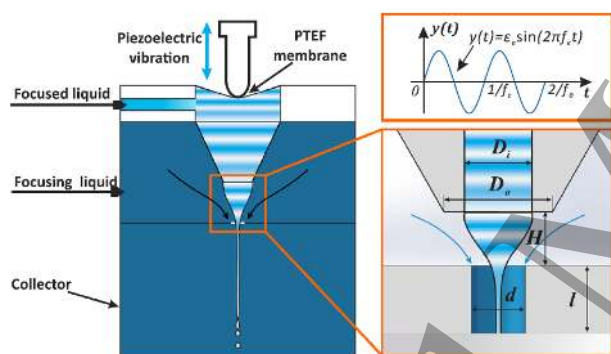


Figure 26: Sketch of the active flow focusing principle. The mechanical vibration acts on the focused liquid [254].

6. Whipping instabilities

As mentioned in the previous section, the existence of an outer fluid medium triggers the transition from the varicose to the whipping (bending, kink) mode for large enough Weber numbers (defined in terms of the jet velocity relative to that of the outer medium) [257]. In this case, surface tension has a stabilizing effect, and the destabilizing factor is purely aerodynamic: a perturbation at the interface causes the outer fluid to accelerate as it passes a crest, lowering the pressure at that point and encouraging the crest to increase in size (as in wind-generated ripples on a liquid free surface). An accurate calculation of the perturbation growth rate requires the consideration of the gas viscosity even for small values

of this parameter [258]. In fact, the existence of an outer boundary layer significantly affects the whipping of a jet discharging into a still gaseous atmosphere.

Electrically charged jets in a hydrodynamically passive dielectric medium may also develop the whipping instability for sufficiently large values of the Taylor number Γ_e [62, 259, 260]. The whipping instability in a perfectly conductor jet can be explained as follows: if a small portion of the jet moves slightly off its axis, the charge re-distributes instantaneously along the jet surface accumulating in the ridges and valleys of the deformed interface. This occurs in such a way that the electrical forces push that portion farther away from the axis [259]. In fact, while the Rayleigh axisymmetric instability reduces the liquid surface per unit volume, the whipping instability does the contrary. This lowers the surface charge density, separates the electric charges, and reduces the potential energy associated with Coulombic repulsion. For a perfectly conductor, apolar and inviscid cylinder in the absence of an externally applied electric field, whipping instability arises at the so-called Rayleigh limit $\Gamma_e = 3/2$ [261].

Both aerodynamic and electrical whipping (Fig. 27) is enhanced by the jet's viscosity, which damps out the varicose mode in favor of bending perturbations. As mentioned in Sec. 4, whipping almost always exhibits a convective character, and, therefore, it is observed far beyond the tapering liquid source. In fact, the convective-to-absolute instability transition for the lateral mode $m = 1$ has been found in very few works [180, 251].

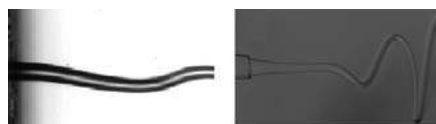


Figure 27: Whipping instability in a viscous microjet produced by gaseous flow focusing [189] (left) and liquid-liquid electrospray [262] (right).

Whipping arises in a number of microfluidic configurations, including electrospray/electrospinning [259, 263] and flow focusing [189]. The violent slashes characterizing the whipping regime are responsible for wider droplet size distributions with smaller average values. Whipping instability precludes the gentle deposition of the emitted jet or the droplets resulting from its breakup. It can be controlled by making the surrounding fluid coflow with the jet, as occurs in electro-coflowing [262] and electro-flow focusing [54] for ambient pressure mass spectrometry [264], or in electrohydrodynamic direct-writing [265] assisted with airflow [55].

External fields applied to the fiber extruded in near-field electrospinning allow controlling the fiber oscillation to build 3D structures [266]. Whipping usually has a positive effect in the production of polymeric fibers because the slashes mentioned above considerably reduce the diameter of the precursor jet before its solidification. Nevertheless, it can be suppressed by combining low and uniform electrical fields with the mechanical pulling exerted by the collector [267].

7. Jet breakup

7.1. Newtonian liquids

7.1.1. Satellite droplets

The linear (local or global) stability analysis describes only the early stage of the interface deformation during the jet breakup. Non-linear contributions to the hydrodynamic equations invalidate the predictions derived from this analysis for the late phase of the thread breakup. This occurs even in the Stokes limit (when the nonlinear convective term can be neglected) due to the nonlinearity of the capillary pressure.

Consider the Lagrangian frame of reference solidly moving with the jet. The growth of the unstable sinusoidal linear mode produces a neck and two bulges on the two sides of the neck. The liquid evacuates the neck towards the bulges driven by the capillary pressure, accelerating in the direction of motion. For $Oh_j \ll 1$, the acceleration takes its maximum value in a section located between the neck and the bulge, which makes the central neck symmetrically split into two ones. Each neck migrates towards the closest bulge until pinching the interface. This migration is responsible for the formation of a satellite droplet between the two parent drops [268]. Satellite droplets are an undesired effect in most microfluidic applications.

The formation of satellite droplets in Newtonian liquid jets has been studied since the early seventies. Goede and Yuen [269] compared their experiments with the weakly nonlinear analysis of Yuen [270]. Chaudhary and Maxworthy [271] determined the conditions to suppress the satellite droplets by forcing the precursor liquid jet. Direct numerical simulations of the Navier-Stokes equations were conducted by Mansour and Lundgren [272] and Ashgriz and Mashayek [273]. They found very good agreement between the computed droplet radii and the experimental values obtained by Rutland and Jameson [274] and Lafrance [275]. As will be explained below, subsequent works have considered the effect of electric fields [276–279] and surfactants [81, 123, 280–284] on the satellite droplet formation in

jets and similar configurations (liquid bridges, pendant drops, ...). To study these and other effects, accurate adaptive solvers [285], boundary fitted methods [286], and elliptic mesh generation techniques [284] have been developed.

7.1.2. The interface pinch-off

The pinching of a Newtonian liquid free surface constitutes a formidable problem that offers a unique opportunity to observe the behavior of fluids with arbitrarily small length and time scales. Theoretical and experimental studies have focused on the evolution of the free surface minimum radius, R_{\min} , to determine which forces are relevant in the vicinity of the pinching region.

For small viscous effects, the thinning of the liquid thread passes through an inertio-capillary regime characterized by the power law

$$R_{\min} = A \left(\frac{\sigma}{\rho} \right)^{1/3} \tau^{2/3}, \quad (42)$$

where τ is the time to the pinching [131, 287]. Different values of A have been determined experimentally [288, 289]. Recent experiments and numerical simulations with very low viscosity liquids have found that the dimensionless prefactor A exhibits a complex, non-monotonic behavior over many orders of magnitude in τ [290]. In those experiments and simulations, A never fully reached its asymptotic value $A \simeq 0.717$.

When viscous stresses are dominant, capillary pressure drives the flow against them during an intermediate phase, where the minimum radius verifies the equation [291]

$$R_{\min}(\tau) = 0.0709 \sigma / \mu_j \tau. \quad (43)$$

For lengths and times to the pinching of the order of or smaller than the intrinsic characteristic length $\ell_0 = \mu_j / (\sigma \rho_j)$ and time $\tau_0 = \mu_j^3 / (\sigma^2 \rho_j)$, the system is expected to reach an inertio-viscous-capillary regime in which all three forces are commensurate with each other. In this regime, the free surface minimum radius obeys the universal law [131]

$$R_{\min}(\tau) = 0.0304 \sigma / \mu_j \tau. \quad (44)$$

Figure 28 shows both the universality and validity of (42) and (44) [292].

The universal inertio-viscous-capillary regime is limited by the appearance of noticeable thermal fluctuations when the thermal length scale $\ell_T = k_B T / \sigma$ (k_B is the Boltzmann constant) is reached, which is of the order of 1 nm at room temperature T [293, 294]. Thermal fluctuations make nanojets adopt double-cone neck

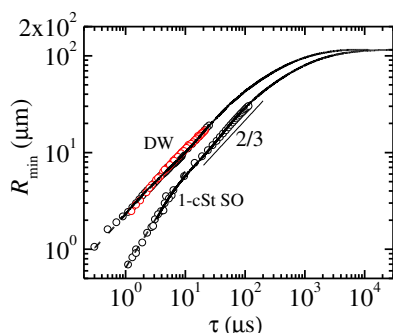


Figure 28: Free surface minimum radius R_{\min} as a function of the time to the pinching τ for deionized water (DW) and 1-cSt silicone oil (SO) [292]. The black and red symbols are the experimental data obtained from the breakup of a pendant drop hanging on a nozzle 115 and 205 μm in radius, respectively. The solid and dashed lines are the full numerical solution of the Navier-Stokes equations and the universal laws (42) with $A = 0.55$ for DW and (44) for SO.

shapes before breakup, which almost eliminates the formation of satellite droplets.

A complex scenario of intermediate transitions between the regimes (42)–(44) may take place before the liquid thread adopts the final inertial-viscous-capillary regime [295, 296]. Shi et al. [297] described the repeated formation of necks during the pinching of a viscous drop falling from a faucet. They explained this phenomenon in terms of the experimental noise. Long microthreads were observed by Kowalewski [298] during the breakup of jets around 50 cSt in viscosity. Interestingly, those microthreads stretched until their diameters fell down below approximately $1\text{ }\mu\text{m}$. Then, the thinning process stopped, and the microthread broke up due to the growth of capillary waves, which gave rise to micrometer subsatellite droplets.

The pinch-off of an inviscid bubble is qualitatively different from its droplet counterpart. The minimum radius follows a non-universal power law with irrational exponents in the interval 0.53–0.57 [299–301], which are not strictly constant but exhibit logarithmic corrections [302–305]. The shape of the singular region evolves from a conical shape to a slender cylinder over many decades in time of the pinch-off process. This behavior bifurcates from that of the droplet for a density ratio around 0.25 [306]. If there is a sufficiently intense gas flow across the pinching region so that the convective term in the momentum equation becomes of the order of that of the liquid, then the pinching region may become asymmetric and the scaling exponent becomes $1/3$ [304, 307].

When the external liquid viscosity, however small, is taken into account, then capillary stresses are asymptot-

ically balanced by viscous stresses in the two liquids, while inertia becomes negligible [308, 309]. The linear law (44) holds but with a prefactor which depends on the viscosity ratio. The presence of a viscous outer medium produces an exceptional form of singularity in which a long liquid thread forms before pinch-off, which violates universality and retains an imprint of the initial and boundary conditions [301, 303, 310]. This behavior was also found in bubbles quasi-statically injected in a moderately viscous bath [301, 303], whose pinch-off is characterized by a scaling exponent significantly larger than $1/2$. Pahlavan et al. [311] have recently shown that the pinch-off dynamics of a bubble confined in a cylindrical capillary go through an early-time self-similar regime which erases the system's memory of the initial conditions and restores universality to bubble pinch-off.

Recent experiments [292] have shown that fluid dynamics in the vicinity of the pinching are much more intricate than what one may expect for apparently Newtonian liquids. Subsatellite droplets arise upon closer inspection during the breakup of pendant droplets of silicone oils. It has been speculated that this phenomenon is produced by bulk viscoelasticity effects caused by the extraordinarily small length and time scales reached as the system approaches the free surface breakup (Fig. 29). For very small surface tensions, the pinch-off of the interface between two liquids can be dominated by diffusion in the bulk [312] before thermal fluctuations come into play [313, 314]. Rubio-Rubio et al. [315] have recently modeled the pinch-off dynamics in the presence of particulate suspensions. Ruth et al. [316] have shown that turbulent flow field freezes in the final stage of the bubble pinching of a bubble, which leads to a self-similar collapse close to that of the unperturbed configuration.

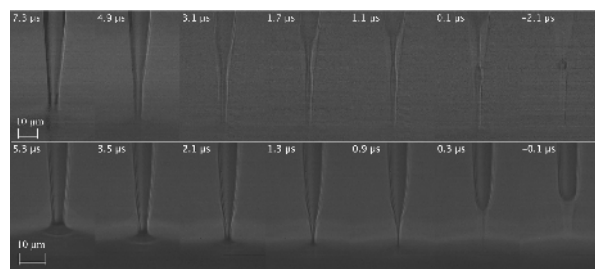


Figure 29: Pinch-off of a drop of 5-cSt silicone oil (upper images) and glycerol/water 48/52% (v/v) (lower images) [292]. The Ohnesorge number takes practically the same value in the two cases. The labels indicate the time to the pinching with an error of $\pm 100\text{ ns}$.

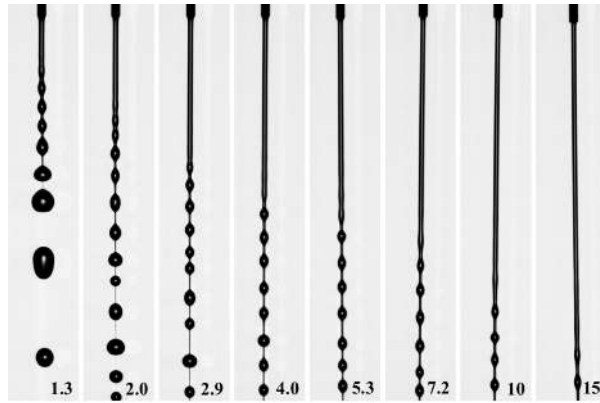


Figure 30: Breakup of a jet of 0.1 wt.% PEO solution emitted from a nozzle 0.15 mm in diameter for different Weber numbers as indicated in the bottom corner [320].

7.2. Viscoelasticity, electric fields and surfactants

The breakup of jets becomes a rich and intricate problem when complex liquids [36] are considered. The presence of tiny amounts of polymeric molecules drastically alters the breakup dynamics. In this case, two consecutive drops are connected by a thin thread right before the breakup of the viscoelastic jet (Fig. ??). These threads are subject to uniform axial stress caused by the elasticity of the dissolved polymeric molecules [317]. In the elasto-capillary regime, the thinning of the liquid thread is driven by surface tension and resisted by that axial stress [62]. Experiments show that the time evolution of the thread minimum radius obeys the exponential function [318]

$$R_{\min}(t) = \hat{A} \exp[-t/(3\lambda_{\text{ext}})]. \quad (45)$$

If one assumes that this evolution can be described by the Olroyd-B model (5), the extensional relaxation time λ_{ext} coincides with the stress relaxation time λ_s (see Sec. 2). Eggers et al. [319] have recently shown that the thread profile calculated from the Olroyd-B model and rescaled by the thread thickness converges to a similarity solution.

The beads-on-a-string structure is a drop-like pattern created on a viscoelastic thread by the capillary instability [71, 321]. During the later stage of the viscoelastic thread thinning, polymers come close to their full extension, the extensional viscosity reaches an almost constant value, the thread behaves as a viscous Newtonian filament subject to the capillary instability, and tiny beads start to appear on the filament, giving rise to the so-called *blistering* instability [322]. However, Sattler et al. [323] have observed experimentally growth rates that were greater by several orders of magnitude than

those expected from the capillary instability based on a Newtonian extensional viscosity. Eggers [324] has proposed an alternative explanation of the blistering phenomenon in terms of a demixing instability, which locally relaxes polymeric stress.

The integration of the full Navier-Stokes equations over the breakup of a perfectly conductor cylindrical jet immersed in a radial electric field shows that nonlinear terms generally delay the jet breakup [279]. The diameter of the primary (satellite) droplet decreases (increases) as the electric strength increases, especially for large values of the Ohnesorge number. Collins et al. [279] described how electrostatic stresses over the interface produce similar effects to those of inertia in producing satellite droplets, which leads to the formation of such droplets even in the Stokes limit. Finite conductivity effects significantly affect the breakup process [325]. In this case, electrokinetic effects may considerably alter the distribution of electric charges between primary and satellite droplets [95].

The electric field has no significant influence on the local pinch-off dynamics of a conductor liquid thread for low values of the Ohnesorge number [279]. Similar conclusions have been obtained in the Stokes limit [97, 326]. However, the asymptotic behavior might be affected by the electric stresses in this case, because the relative magnitude of the electrostatic stress versus the capillary one increases in the pinch point as the interface breakup approaches [279]. In some configurations, the pinch-off solution cannot be obtained if only the leading order term is used in the electrostatic problem [326].

Microthread cascades may arise during the breakup of jets loaded with surfactants [282] due to the action of Marangoni stresses [284]. These microthreads give rise to tiny subsatellite droplets following the free surface breakup (Fig. 31). It is a question of controversy whether surfactants are swept away from the pinching region, and, therefore, the system follows the self-similar dynamics of clean viscous jets at times close to the breakup [81, 97, 123, 280, 327, 328]. Martínez-Calvo et al. [329] have recently shown the existence of a discontinuous transition at a critical elasticity below which satellite droplets are not formed. Experimental studies have also quantified the effect of surfactants on the size of satellite droplets [123, 330, 331].

The breakup of jets of complex fluids is still an open problem. There are factors, such as surface viscous stresses associated with surfactant monolayers [123], whose relevance is yet to be determined. High-resolution experiments and numerical simulations show the importance of surface viscosity in the final stage of the breakup even for quasi-inviscid surfactants [332].

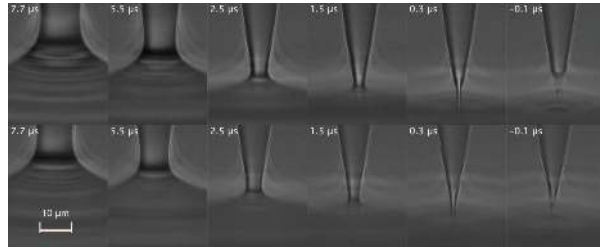


Figure 31: Pinch-off of a drop of water+SDS 0.8cmc (upper images) and water+SDS 2cmc (lower images) [332]. The labels indicate the time to the pinching with an error of ± 100 ns. The breakup of that microthread produces a subsatellite droplet 1-2 μm in diameter.

When Marangoni and surface viscous stresses are taken into account, the surfactant is not swept away from the thread neck. Surface viscous stresses eventually balance the driving capillary pressure in the pinching region.

Wee et al. [134] have recently extended the viscous law (43) to account for the effect of a viscous surfactant monolayer in the limit of infinite surface Peclet number. Bulk viscosity, surface viscosity and capillary pressure compete with each other, which results in the asymptotic law

$$R_{\min}(\tau) = \frac{0.0709}{1 + 5B_{s0}/3R_{\min0}^*} \frac{\sigma}{\mu_j} \tau, \quad (46)$$

where $B_{s0} = \mu^S/\mu R_0$ is the Boussinesq number, R_0 is the initial radius of the liquid thread, and $R_{\min0}^*$ the initial value of R_{\min} in terms of R_0 . When the free surface is flooded by surfactant [333], or in the limit of zero Peclet number [134], surface viscous stresses are predicted to cause the exponential thinning of the liquid thread right before its breakup. Surface viscoelasticity effects on the pinching of interfaces covered by surface-active bio-polymers have recently been considered too [334].

7.3. The 1D approximation

The results described above possess great interest at the fundamental level, but they have relatively little consequences in terms of microfluidic applications. At this level, attention is normally paid to the formation and size of satellite droplets. For this purpose, many theoretical studies make use of the 1D (slenderness) approximation (see Sec. 2.4) to simulate the breakup of a fluid thread whose length equals $\lambda^{\max}/2$ (λ^{\max} is the wavelength of the most unstable perturbation). Significant features of that process have been accurately described based on this approximation, even though the jet adopts non-slender shapes before its breakup.

Bhat et al. [321] plotted a phase diagram in the space defined by Deborah $De = \lambda_s/\hat{t}_{ic}$ and Ohnesorge numbers depicting the regions where the different beads-on-a-string morphologies can be found during the breakage of an Oldroyd-B filament.

The 1D approximation has been used to examine the nonlinear breakup of electrified jets. López-Herrera and Gañán-Calvo [278] and Collins et al. [279] calculated the diameter and charge of both the primary and satellite droplets formed after the breakup of a conducting jet subject to a radial electric field. The extended version of this model indicates that ionic surfactants and electrokinetic effects increase the size of satellite droplets but have little influence on the breakup time [97]. The breakup of highly-electrified jets can give rise to fascinating structures, including the formation of spikes which emit tens of ultra-fine jets from their periphery (Fig. 32) [335]. If a sufficiently intense radial electric field is applied to the jet, non-axisymmetric perturbations can grow and lead to the formation of Taylor cones evenly distributed at the equator of a droplet [336].

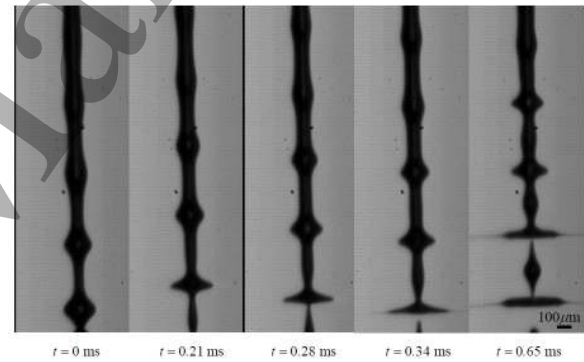


Figure 32: Formation of spikes on a jet of a mixture of ethanol and glycerol ejected at a flow rate of 3000 $\mu\text{L}/\text{min}$ and subjected to an electric voltage of 6.4 kV [335].

Numerical solutions of the 1D model have shown that large satellites may form during the breakup of jets laden with strong surfactants at concentrations above the CMC. This phenomenon is driven by Marangoni stresses instead of liquid inertia [81]. Experiments with liquid bridges indicate that the satellite droplet diameter can either increase or decrease due to the presence of surfactant depending on the Ohnesorge number [331].

8. Tip streaming in open systems

Viscosity and surface tension are the two forces which oppose the formation of droplets, bubbles and

jets in microfluidics. In standard dripping and jetting, the energy necessary to overcome those forces is injected into the dispersed phase somewhere upstream in the feeding system. In tip streaming, that source of energy is replaced by an external agent which gently pushes the fluid towards the tip of a parent drop or stretched meniscus attached to a feeding capillary [14, 16, 18, 22, 23, 26, 34, 35, 337–343]. In this way, the energy transmitted to the dispersed phase is literally focused on the critical region where the droplet/jet forms. The fluid accelerates in the drop/meniscus tip to the extent of overcoming the intense resistance offered by the viscous stress and capillary pressure, which allows the formation of tiny droplets/bubbles or a very thin jet. The tapering drop/meniscus becomes a complex fluidic structure, the product of a delicate balance between inertia, surface tension and viscosity, depending on the specific situation considered. The existence of a stagnation point right in front of the emission point is a common feature of tip streaming, which may have applications in analytical chemistry and life sciences [344].

Eggers and du Pont [345] studied numerically the appearance of tip streaming when drops, bubbles and films are deformed by strong viscous flows. They found that the interface near the tip exhibited universal features, independent of the outer flow and the system geometry considered. Tseng and Prosperetti [346] have argued that the tip streaming arising in different configurations is reducible to a common instability that can take place owing to a local convergence of streamlines in the vicinity of a zero-vorticity point or line on the interface.

Tip streaming exhibits a rich and interesting phenomenology. For large enough Reynolds numbers, the external driving force typically induces a recirculation pattern with a stagnation point next to the region where the droplets/bubbles or the jet are emitted [108, 347]. For sufficiently small Reynolds numbers, viscous stresses generally direct the fluid towards the source tip, precluding the growth of such a pattern [109, 348]. Interestingly, recirculation can also be found in the Stokes flow appearing in some tip streaming configurations [16, 349].

In this section, we present some results about tip streaming realizations in *open systems*. In these systems, the external fluid medium is not bounded or it does not affect the tip streaming (electrohydrodynamic tip streaming), and, more importantly, there is no control on the dispersed phase response (e.g., by injecting it at a prescribed flow rate). At least one of these conditions does not hold in the microfluidic configurations described in Sec. 9.

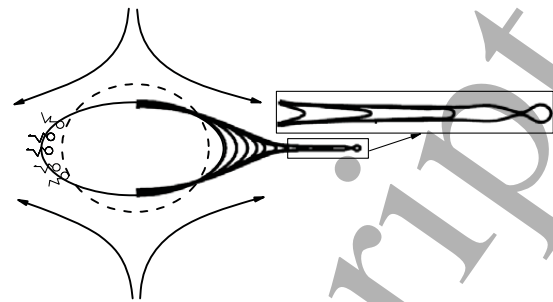


Figure 33: Breakup of a droplet loaded with an insoluble surfactant in the presence of a linear extensional flow [35]. The contours on the right side were calculated from the numerical simulation of the Stokes flow for $Ca_G = 0.065$, $\Gamma_{eq}/\Gamma_\infty = 0.1$ and $\mu_i/\mu_o = 0.05$.

8.0.1. Surfactant-driven tip streaming

In his pioneering work, Bruijn [34] described the tip streaming occurring in a surfactant-laden droplet submerged in a simple shear flow. He concluded that surfactants trigger tip streaming, which then disappears as surfactants are convected away from the tip.

Figure 33 shows the numerical simulation of the breakup of a droplet loaded with an insoluble surfactant in the presence of a linear extensional flow [35]. Surfactant molecules are dragged by the flow towards the poles of the droplet, which reduces the interfacial tension there. When the Capillary number

$$Ca_G = \frac{\mu_o G a}{\sigma_{eq}} \quad (47)$$

exceeds a critical value, the droplet ejects a thin liquid thread from its poles. Here, μ_o is the outer viscosity, G is the strain rate of the far-field flow, a is the droplet radius, and σ_{eq} is the equilibrium interfacial tension. For a given surfactant elasticity, the critical Capillary number in the Stokes regime depends on the inner-to-outer viscosity ratio μ_i/μ_o and the (dimensionless) surface surfactant concentration $\Gamma_{eq}/\Gamma_\infty$. Booty and Siegel [343] calculated the critical Capillary number when the dispersed phase is a gas.

Wang et al. [350] studied the effect of the surfactant solubility on the surfactant-driven tip streaming. The ejected filament becomes thinner as the Biot number (the ratio of the desorption time to the characteristic hydrodynamic time) increases. The parameter conditions for the appearance of tip streaming were determined.

To the best of our knowledge, tip streaming in the open systems described above has been observed neither experimentally nor numerically without adding surfactants to the interface. Therefore, surfactants are

probably necessary in these systems, while they simply facilitate tip streaming in confined hydrodynamic configurations such as coflowing and flow focusing [36, 186, 351]. This facilitator is important if one wants to produce steady jetting tip streaming with a gaseous dispersed phase [169].

8.0.2. Surfactant-free tip streaming

As described above, when a drop/bubble is loaded with an insoluble surfactant, the viscous stresses exerted by an outer shear or extensional stream push the surfactant molecules towards the poles of the drop. This reduces the surface tension in that region, which may result in the ejection of a fluid thread much smaller than the droplet/bubble size. This was one of the first mechanisms used to produce tip streaming in both droplets [34, 35] and bubbles [343].

In the absence of surfactants, Zhang [349] showed that the steady recirculating stream arising in a droplet attached to a capillary of radius R_i and submerged in an extensional (straining) flow evolves towards tip streaming when the Capillary number

$$Ca_G^* = \frac{2\mu_o G R_i}{\sigma} \quad (48)$$

exceeds a critical value (Fig. 34). This transition to tip streaming refers to the sharp reduction of the diameter of the ejected fluid thread when the Capillary number reaches its critical value. The above result indicates that steady tip streaming can be obtained by purely hydrodynamic means if the ejected volume is replaced through the feeding capillary at the appropriate rate (see Sec. 11). Other microfluidic techniques, such as electrospray and flow focusing, can be categorized as this type of flow too (see Secs. 12 and 13). Zhang [349] pointed out the importance of reaching tip streaming at the critical condition by reducing progressively the Capillary number, a requisite similar to that experimentally found for the injected flow rate in electrospray and flow focusing. It should be noted that these numerical results were based on the slender body theory, which is an uncontrolled approximation for a conical interface.

8.0.3. Electrohydrodynamic tip streaming

In his pioneering work, Rayleigh [261] predicted that an incompressible charged liquid droplet becomes unstable due to the growth of the quadrupole oscillation mode when the disruptive Coulomb force equals the attractive surface tension force (the so-called Rayleigh limit). He also claimed that higher multipole oscillations can cause the ejection of very fine jets. Taylor [14]

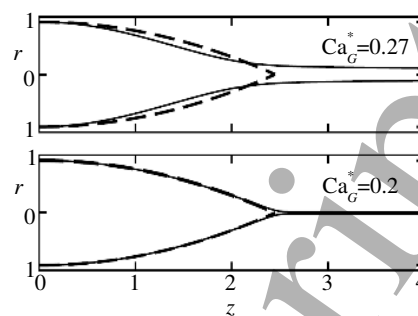


Figure 34: Numerical simulation of tip streaming in a droplet submerged in an extensional flow [349]. The solid lines represent the solutions when the Capillary number Ca_G^* is progressively reduced. The critical Capillary number is 0.2. The dashed line outlines the shape for $Ca_G^* = 0.2$ and zero ejected flow rate.

described experimentally the ejection of those jets from the conical points of electrified films. Duft et al. [342] observed the emission of Rayleigh jets from the tip streaming taking place in the poles of levitated droplets (Fig. 35) [352–354]. The problem has been numerically solved considering both the leaky-dielectric model [355, 356] and electrokinetic effects [92, 96, 357].

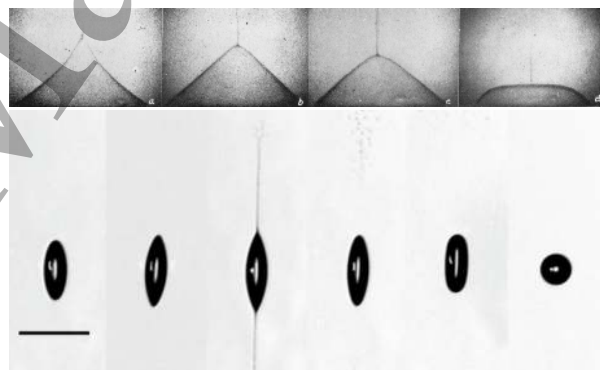


Figure 35: (Upper images) Jet formation and subsequent collapse of a soap film [14]. (Lower images) Disintegration of a levitated droplet of ethylene glycol charged to the Rayleigh limit. Scale bar, 100 μm [342].

The periodic or steady ejection produced by tip streaming in the microfluidic configurations described in Sec. 9 is preceded by an intrinsically unsteady process, where the drop/bubble/meniscus stretches until emitting the first droplet/bubble. The characteristics of the latter (size, velocity, electric charge, ...) significantly differ from those of the droplets/bubbles ejected when tip streaming is properly established (steady ejection). The size and velocity of the first-emitted droplet shown in, for instance, Fig. 33 is expected to be significantly different from those of the droplets emitted

under steady conditions. Steady tip streaming would be reached if the ejected liquid were replaced by injecting liquid into the droplet with a feeding capillary. In this case, the injected flow rate becomes a control parameter that allows tuning the size of the emitted jet.

The distinction between the first ejection and that taking place in the steady regime of tip streaming has been made clear for electrohydrodynamic tip streaming. Under certain conditions, a low-conductivity pendant droplet subject to a strong electric field ejects a thin liquid thread, which issues a stream of tiny drops (Fig. 36). The masses and charges of those droplets are essentially determined by the liquid properties and reflect the electrohydrodynamic history leading to them. The first droplet produced by this unsteady process is particularly important due to its very small diameter and large electric charge (per unit volume). After this first phase of the ejection process, the system reaches spontaneously a quasi-steady regime characterized by a natural (intrinsic) flow rate Q^* , electric current, and droplet diameter, which essentially depend upon the liquid properties too [358]. If a flow rate $Q \geq Q^*$ is prescribed by, for instance, injecting liquid across a feeding capillary, the above quasi-steady process gives rise to the steady cone-jet mode of electrospray.

Gañán-Calvo et al. [92] have studied the onset of electrohydrodynamic tip streaming by assuming that the hydrodynamic and electric relaxation times are commensurate with each other. This assumption, the self-similar collapse of the drop's tip, and the balance between inertia, axial viscous stresses, surface tension, and electrostatic suction during the liquid thread evolution, enable the calculation of the scales for the emitted droplet diameter d_d and electric charge q_d :

$$d_d = \delta_\mu^{-1/3} \varepsilon^{5/12} d_o, \quad q_d = \delta_\mu^{-2/3} \varepsilon^{7/12} q_o, \quad (49)$$

where $\delta_\mu = \rho d_o v_o / \mu$ is the electrohydrodynamic Reynolds number, ε is the liquid permittivity in terms of that of vacuum ε_o , and d_o , v_o , q_o and E_o are the characteristic quantities of the process given by the expressions $d_o = (\sigma \varepsilon_o^2 / \rho K^2)^{1/3}$, $v_o = (\sigma K / \rho \varepsilon_o)^{1/3}$, $q_o = \varepsilon_o E_o d_o^2$ and $E_o = (\sigma / d_o \varepsilon_o)^{1/2}$ (ρ , μ , and K are the liquid density, viscosity, and conductivity, respectively). Figure 37 shows the experimental and numerical validation of scaling laws (49).

The first ejection taking place in electrohydrodynamic tip streaming has also been considered in other works. Fontelos et al. [359] studied theoretically the unsteady elementary disintegration of charged and neutral conducting drops under externally applied electric fields. The onset of tip streaming in low-conductivity

drops after a step-change in the electric field magnitude has been examined both experimentally [98, 360–362] and theoretically [26, 92, 96, 98, 99, 355]. In the latter case, the analysis has been conducted both assuming perfect volumetric charge relaxation (the leaky-dielectric model) [26, 98, 355] and considering certain charge relaxation phenomena along the process [92, 96, 99].

Electrohydrodynamic tip streaming from an initially spherical droplet can be triggered by an electric field producing either oblate or prolate deformations on the droplet in the direction of the applied field. These deformations are due to the electrohydrodynamic flow pattern induced by the electric field [100]. In the Stokes regime, for a liquid droplet suspended in an immiscible liquid environment, the induced surface velocity depends on the ratios of inner to outer viscosities, electrical conductivities and permittivities. Brosseau and Vlahovska [363] demonstrated that an oblate deformation can eventually lead to tip streaming from the equatorial rim generated by the sustained non-linear deformation of the drop (Fig. 38). This phenomenon leads to the formation of a thin sheet that gives rise to thin toroidal rings by 2D capillary breakup, which eventually break up in the azimuthal direction [363]. This process generates beautiful arrangements of monodisperse droplets in the equatorial plane of the parent drop. Interestingly, the two-dimensional breakup can produce main and satellite rings, leading to a finite variety of droplet sizes.

Beroz et al. [364] have recently calculated the critical electric field at which a conducting droplet or bubble sitting on a conductor plate becomes unstable and emits a tiny jet from its apex. The result is

$$\chi = \frac{2}{\pi} \frac{R_i^3}{\mathcal{V}}, \quad (50)$$

where $\chi = \varepsilon_o E^2 R_i / \sigma$ is the electric Bond number, E is the applied electrical field, R_i is the triple contact line radius, and \mathcal{V} the droplet volume. The prefactor $2/\pi$ was determined experimentally.

The ejection of the first droplet in electrohydrodynamic tip streaming resembles other similar phenomena, like the formation of jets by the collapse of a free surface [366, 367]. Similar arguments to those presented here have been used to derive the universal scaling laws for the size and speed of the drop emanating from the breakup of a liquid jet generated by the collapse of a bubble [368].

As mentioned above, tip streaming can be sustained over time by replacing the fluid ejected at the appropriate rate using a certain microfluidic configuration. In

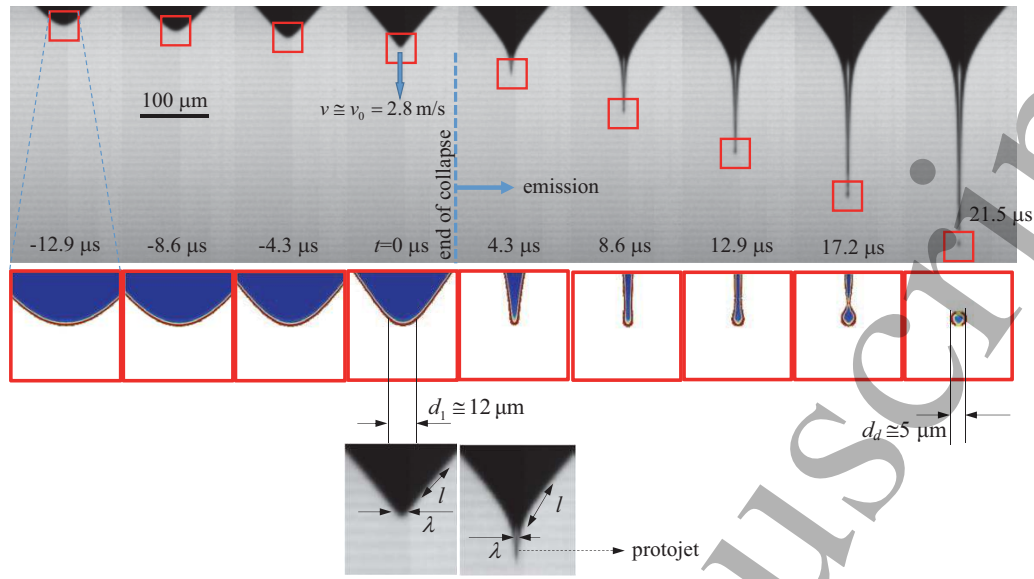


Figure 36: Global view of the first-droplet ejection process in electrohydrodynamic tip streaming [92]. The upper images correspond to an experiment with 1-octanol. The central graphs show the evolution of the front from the corresponding numerical simulations. The colors indicate the dimensionless volume charge density from 0 (blue) to 1 (red). The two lower images show the magnification of the meniscus tip for $t = 0$ and $t = 4.3 \mu\text{s}$. The process can be divided into two stages: the droplet tip collapse for $t < 0$, and the jet emission for $t > 0$.

this way, periodic or steady ejection is achieved. This phenomenon occurs within relatively narrow regions of the parameter space. Understanding the physical mechanisms that bound those regions is still an open problem, and constitutes an important challenge at a fundamental level. However, these aspects of the problem lag behind most applications, where the major interest is precisely the ejecta. In Secs. 10 and 11, we will focus on this facet of the problem for the microfluidic configurations considered in this review.

9. Microfluidic configurations and governing parameters

9.1. Axisymmetric injection

Axisymmetric devices have higher throughput and are more robust and resistant to aggressive chemical conditions than their 2D counterparts. They are typically made of hard materials such as metal [18, 31, 369] or borosilicate glass [21, 370], which do not swell and can easily be functionalized to control surface properties. Glass nozzles with the desired converging or diverging rate can be produced in a controlled manner with the fire shaping procedure [371, 372]. Needles manufactured by a laser beam welding process have been assembled to fabricate triaxial flow focusing devices [373]. Alternative fabrication processes of ax-

isymmetric devices include soft-lithography [374], ceramic [375] or polymer (Cellena®, OneNeb®, Ingeniatics Tec. S.L.) microinjection molding, and, more recently, 2-photon polymerization [376], which is a form of high-resolution 3D printing to manufacture devices with submicron resolution (Fig. 40).

In an axisymmetric microfluidic device (Fig. 41), a fluid stream of density ρ_i and viscosity μ_i is injected across a feeding capillary (nozzle) of inner radius R_i at a constant flow rate Q_i . The surrounding medium is another fluid phase of density ρ_o and viscosity μ_o , immiscible with the former, and separated from it by an interface with a surface tension σ . To simplify the analysis, we will assume that the end of the feeding capillary is sharpened, and the triple contact line anchors at its edge. It is worth mentioning that care must be taken when injecting gases in a microfluidic application, because pressure fluctuations taking place both upstream and downstream the injection circuit may lead to significant variations of the instantaneous flow rate.

The dimensionless numbers characterizing the fluid injection described above are the Weber and Reynolds numbers defined as

$$\text{We}_i = \frac{\rho_i V_i^2 R_i}{\sigma}, \quad \text{Re}_i = \frac{\rho_i V_i R_i}{\mu_i}, \quad (51)$$

where $V_i = Q_i/(\pi R_i^2)$ is the mean velocity in the capillary. The problem is also described in terms of the

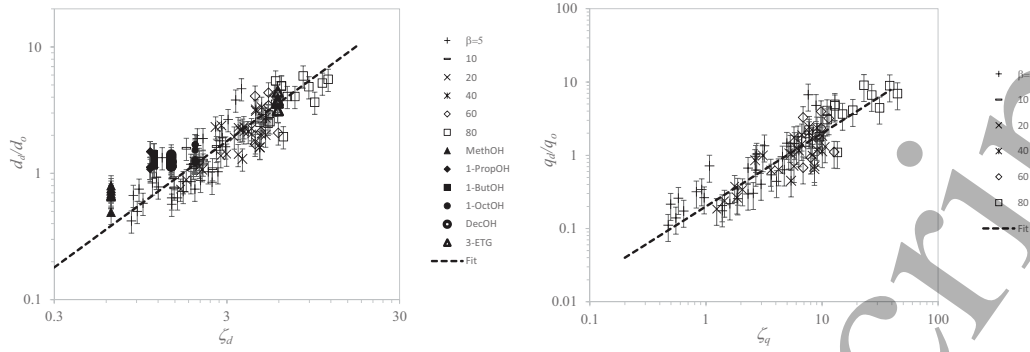


Figure 37: Dimensionless diameter d_d/d_o (left) and electric charge q_d/q_o (right) of the first droplet ejected in electrohydrodynamic tip streaming as a function of $\zeta_d \equiv \delta_\mu^{-1/3} \epsilon^{5/12}$ and $\zeta_q \equiv \delta_\mu^{-2/3} \epsilon^{7/12}$ [92]. The lines are the scaling laws (49). The open and solid symbols are the results obtained from numerical simulations and experiments, respectively. The labels indicate the value of ϵ in the numerical simulations, as well as the liquid used in the experiments.

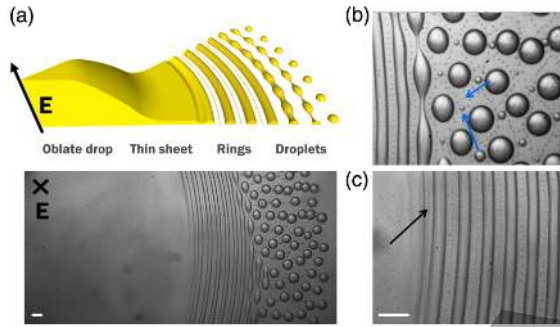


Figure 38: Electrohydrodynamic equatorial tip streaming [363]. (a) Three-dimensional rendering of the phenomenon. The thin sheet is the slightly brighter region right in front of the edge where the ring is forming. (b) Two generations of satellite droplets produced by the ring breakup (blue arrows). (c) Satellite ring that breaks up in droplets (black arrow). The scale bars are 100 μm .

density and viscosity ratios

$$\rho = \frac{\rho_o}{\rho_i}, \quad \mu = \frac{\mu_o}{\mu_i}. \quad (52)$$

For $\text{Re}_i \ll 1$, the inertia of the inner fluid becomes negligible, and the fluid injection can be described just in terms of the Capillary number

$$\text{Ca}_i = \frac{\text{We}_i}{\text{Re}_i} = \frac{\mu_i V_i}{\sigma} \quad (53)$$

and the viscosity ratio μ .

For sufficiently large values of the Weber and Reynolds numbers, inertia overcomes the resistance offered by both surface tension and viscosity during the fluid ejection, and the feeding capillary drips or emits a jet. When this condition does not hold, the collaboration of some kind of mass or superficial driving force is

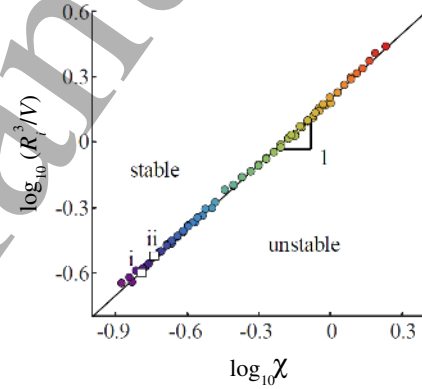


Figure 39: Critical value of the electrical Bond number χ as a function of the dimensionless drop volume V/R_i^3 [364]. The symbols and the line correspond to the experimental values and the prediction (50), respectively. The squares are the results of the experiments conducted by Wilson and Taylor [338] (i) and Basaran and Scriven [365] (ii).

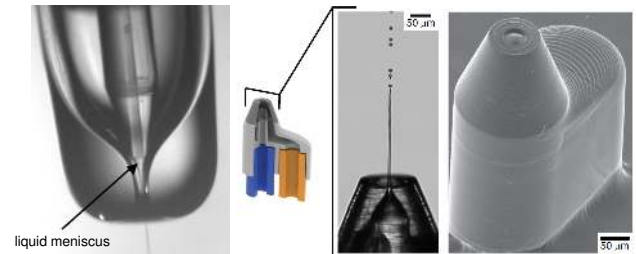


Figure 40: Gaseous flow focusing device fabricated from a flame polished glass capillary (left) [370] and an ultracompact nozzle printed with two-photon polymerization (Nanoscribe GmbH, Karlsruhe, Germany) (right) [377].

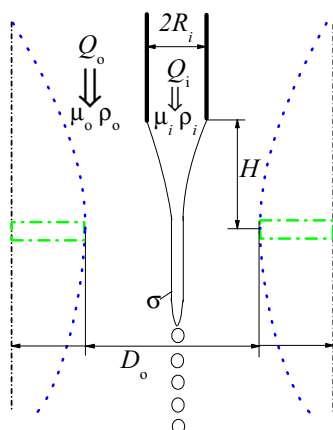


Figure 41: Sketch of an axisymmetric microfluidic configuration driven by hydrodynamic forces. The short-dashed (black), dotted (blue) and dashed (green) lines represent the shape of the outer channel in the co-flowing, nozzle flow focusing and plate-orifice flow focusing configurations, respectively.

required to produce that effect. Figure 41 sketches two of the most commonly used methods to generate that force.

9.2. Gravitational forces

In the gravitational ejection, the feeding capillary is placed vertically in a still ambient, and the fluid is expelled under the action of gravity g . The additional dimensionless number characterizing this process is the gravitational Bond number

$$B = \frac{|\rho_i - \rho_o| g R_i^2}{\sigma}, \quad (54)$$

which compares the capillary pressure σ/R_i with the variation of hydrostatic pressure across the interface, $|\rho_i - \rho_o| g R_i$, due to gravity.

9.3. Electrical force

At the submillimeter scale and/or for density-matched liquids, interfacial stresses dominate over gravity (the Bond number takes very small values), and the fluid ejection cannot rely on that force. The driving mass force can be augmented by applying an external electric field parallel to the feeding capillary.

9.3.1. Electrospray and electrospinning applications

Electrospray is an atomization technique characterized by the interaction between electrostatic, capillary and viscous stresses on a liquid meniscus, which gives

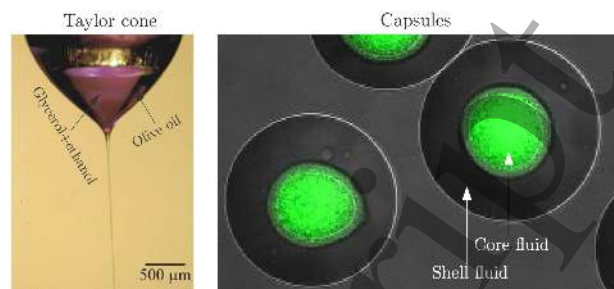


Figure 42: Microencapsulation via AC coaxial electrohydrodynamic atomization [391].

rise to the formation of charged jets and droplets. Electrospray can operate in dripping, jetting and tip streaming [378]. The steady cone-jet mode of electrospray and electrospinning is a classical example of tip streaming induced by electric fields.

The cone-jet mode of electrospray has been applied to produce charged droplets in mass spectrometry [379], to generate electric propulsion for spacecraft [380], to form capillary shapes and structures for drug encapsulation [381, 382] and tissue engineering [383], for high-resolution electrohydrodynamic jet printing [384], to enhance the quality and resolution in Electrostatic Inkjet Printing [385] with nanoparticle inks [142], to form emulsions and microparticles in food industry, and to fabricate compound and hollow fibers [47], among many other applications. New applications are continuously emerging. For instance, Bielecki *et al.* [386] have recently shown that, under certain conditions, electrospray can constitute an advantageous alternative to flow focusing for sample injection for single-particle imaging with X-ray lasers, because it reduces both the size and polydispersity of the aerosol droplets and, consequently, the nonvolatile contaminants.

Coaxial electrohydrodynamic atomization [25, 47, 79, 387] has been used for the formation of polymer coated starch-protein microspheres [388], preparation of suspensions containing microbubbles [389], and production of organic and inorganic macro and nano-sized emulsions [47], among other applications. Recent advances in coaxial electrohydrodynamic atomization have facilitated the use of this technique for fabrication of micro- and nano-sized drugs loaded biodegradable polymeric particles for controlled drug release and biochemical applications [382, 390]. In this case, AC actuation can be used to reduce the detrimental effect of charge content on some drug delivery applications, and enhance the stability of the ejection process [391] (Fig. 42).

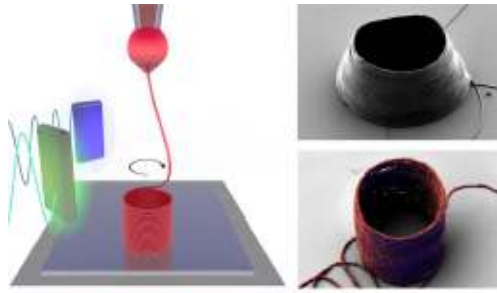


Figure 43: Ultrafast 3D printing of PEO cylindrical microstructures achieved by controlling the voltage applied to electrodes located around the jet emitted in electrospinning [266].

Electrospinning of polymers has become a highly recognized method for the preparation of polymer fibers with diameters ranging from tens of microns down to a few nanometers [73–79, 392–396]. A wide range of complex architectures and morphologies of nanofibers and nonwovens can be produced with electrospinning. The applications of this method include medical areas such as tissue engineering and drug delivery [397], as well as technical fields demanding nanofibers with specific electronic, photonic, photocatalytic and magnetic properties. Nanofiber-based architectures have a positive influence on the development of fuel cells, lithium ion batteries, solar cells, electronic sensors, energy storage systems. Other areas like textile and filter applications have benefited from electrospinning as well [398].

In traditional electrospinning, fibers are produced chaotically. This feature limits the applications of electrospinning in devices that demand arranged or patterned micro/nanoscale fibrous structures. Near-field electrospinning has been developed to deposit ultrafine fibers with unique physical and chemical properties in a direct, continuous, and controllable manner [399]. Fibers fabricated with near-field electrospinning can be used in electronic components, flexible sensors, energy harvesting, and tissue engineering [400]. Sophisticated versions of this technique are continuously emerging. For instance, Liashenko et al. [266] have recently shown that ultrafast 3D printing with submicrometer resolution can be achieved by electrostatically deflecting the emitted jet with electrodes located around it (Fig. 43).

Two key parameters controlling the quality of the electrospinning outcome are the polymer molecular weight and concentration, which somehow play similar roles. It has been observed that lower molecular weights and concentrations lead to thinner fibers, which is desirable because it enhances their functionality. However, decreasing the values of these parameters reduces

both the solution viscosity and elasticity (stress relaxation time), two inhibitors of the capillary instability (see Sec. 5) responsible for the appearance of the undesired droplets or beads. Therefore, uniform (bead-free) fibers are produced at the expense of increasing their diameters, and *viceversa*.

9.3.2. Electric dimensionless numbers

The effect of the electric field can be quantified through the electric Bond (Taylor) number (already introduced in Sec. 8)

$$\chi = \frac{\varepsilon_o E^2 R_i}{\sigma}, \quad (55)$$

where E is a characteristic electric field (typically, the ratio of the applied voltage to the characteristic length R_i) and ε_o the electrical permittivity of the outer medium (insulator). The electric Bond number is essentially the electric strength (41) used in the linear stability of jets. It measures the electrostatic pressure $\varepsilon_o E^2$ in terms of the capillary pressure σ/R_i .

The electrical properties of the dispersed phase are taken into account through the relative permittivity and dimensionless electrical conductivity:

$$\varepsilon = \frac{\varepsilon_i}{\varepsilon_o}, \quad \widehat{K}_i = K_i \left(\frac{\rho_i R_i^3}{\sigma \varepsilon_o^2} \right)^{1/2} = \frac{\varepsilon t_{ic}}{t_e}, \quad (56)$$

where $t_{ic} = (\rho_i R_i^3)/\sigma$ is the characteristic inertio-capillary time, and $t_e = \varepsilon_i/K_i$ is the electric relaxation time. The dimensionless electrical conductivity \widehat{K}_i is essentially the inverse of the dimensionless electric relaxation time τ_{ej} [Eq. (39)] used in the linear stability of jets.

For perfect conductor fluids, $t_e \ll t_{ic}$ ($\widehat{K}_i \gg 1$), the net free electrical charge accumulates “instantaneously” in the interface to cancel the voltage variations throughout the dispersed phase, and the problem becomes essentially independent from \widehat{K}_i . In a leaky-dielectric liquid [101], \widehat{K}_i is sufficiently small to affect the rate at which the net free charge is transferred to the interface. In this case, \widehat{K}_i is one of the governing parameters of the problem.

9.4. Coflowing

Hydrodynamic forces can be employed to control the pinching of the fluid-liquid interface, and to modify the droplet/bubble size, production frequency, etc. Microfluidic devices designed for this purpose can be grouped into three main classes: cross-flowing systems, co-flowing streams, and flow focusing [12]. Only the

last two classes can be realized in an axisymmetric configuration.

In a coflowing device, an outer liquid stream is coaxially injected across a tube of radius R_o to produce drops/bubbles. Tangential viscous stresses exerted by the outer stream constitute the major source of momentum in the liquid-liquid configuration. For this reason, the injection is typically described in terms of the inner Capillary number Ca_i [Eq. (53)], while the intensity of the driving force is quantified through the outer Capillary number

$$Ca_o = \frac{\mu_o V_o}{\sigma}, \quad (57)$$

where V_o is a characteristic velocity of the outer stream. The response of the dispersed phase also depends on the viscosity ratio μ .

The ratio of radii

$$R = R_i/R_o \quad (58)$$

is the only parameter that characterizes this simple geometry. The parameters of the problem can be combined to replace (57) with the ratio Q_r of the outer flow rate Q_o to the inner one Q_i [16]:

$$Q_r = \frac{Q_o}{Q_i} = \frac{R^2 - 1}{\mu} \frac{Ca_o}{Ca_i}, \quad (59)$$

where the thickness of the feeding capillary wall has been neglected. One can distinguish between coflowing configurations with R of order unity [16, 148, 177], and those characterized by $R \ll 1$ [175, 401]. Their behavior is substantially different due to the stabilizing role of confinement and the effect of this factor on the nonlinear phase of the jet breakup.

The production of liquid jets assisted by an outer gaseous stream in a coflowing geometry is much less popular than its liquid-liquid counterpart due to the limited force exerted by the gas in this geometry. Submicrometer fibers can be spun from polymeric solutions using the Solution Blow Spinning (SBS) [51, 57] or air-brushing technique [51], which constitutes an interesting example of a gaseous coflowing geometry. SBS has recently become a popular technique. The physics governing the flow in this configuration has been recently reviewed [402]. In SBS, a polymer solution is extruded across an inner nozzle at a constant flow rate. A pressure drop accelerates the gas current released from an outer nozzle. This current expands around the inner nozzle and creates a liquid meniscus similar to Taylor's cone in electrospinning (Fig. 44). For high enough applied pressure drops, a liquid jet tapers from the meniscus apex and flies towards the collection target. Then,

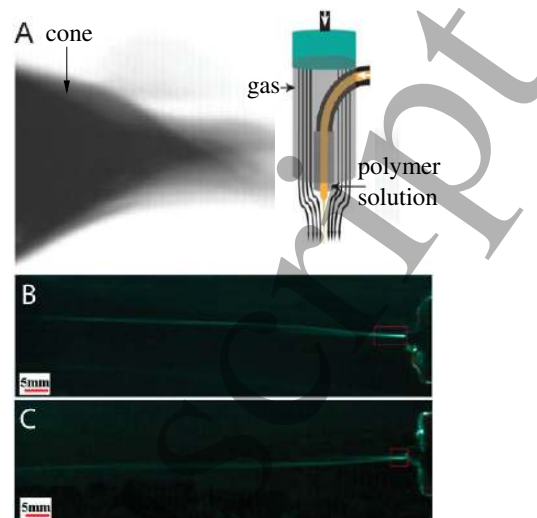


Figure 44: (A) Image of a polymer solution cone at the tip of a SBS device [51]. Image of the polymer jet produced by SBS at gas pressures of 1.121 bar (B) and 1.363 bar (C) [406]. The sketch in the upper-right corner shows the SBS configuration [57].

the solvent evaporates leaving behind polymer fibers. The Gas Jet Process [403] relies on a similar mechanism, although in this case the polymer solution drop is exposed to a high-speed gas stream ejected independently. Nanofibers can also be produced from gas-assisted polymer melt electrospinning [404, 405], where the drag force exerted by the coflowing gas can significantly reduce the fiber diameter.

A coflowing liquid stream can also be used to control the generation of bubbles both in the bubbling and jetting regimes. This configuration produces bubbles considerably smaller than those formed without coflow [407].

9.5. Flow focusing

9.5.1. Axisymmetric geometry and injection method

In flow focusing, the coflowing stream is forced to cross an orifice of diameter D_o located in front of the feeding capillary at a distance H from its end (Fig. 41). This originates favorable pressure gradients [18] and both shear [33] and extensional viscous stresses which stretch the fluid meniscus attached to the feeding capillary. The meniscus tip emits either drops/bubbles or a thin jet that coflows with the outer stream.

Different axisymmetric geometries have been employed to take advantage of the flow focusing principle. The original plate-orifice configuration [18] has been implemented in planar silicon microfluidic chips with multiple orifices keeping the axisymmetric geometry

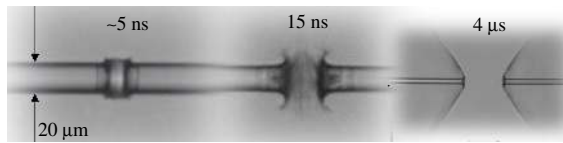


Figure 45: Evolution of the blast induced by a strong X-ray laser pulse (photon energy 8.2 KeV, 0.75 mJ, duration 30 fs) on a liquid microjet of 20 μm in diameter and discharged in a vacuum [417, 418].

per orifice [408]. Microfluidic devices with the axisymmetric flow focusing geometry have also been manufactured in PDMS [43] using stereolithography [409]. Experimenters have utilized glass [189, 370, 410] or ceramic [375] nozzles, and have made use of two-photon polymerization to manufacture the microfluidic device [376] (Fig. 40). Yobas et al. [411] have used an orifice with a cusp-like edge to maximize the stress exerted by the outer stream, which ensures the controlled breakup of droplets for a wide range of flow rates. The focusing effect can also be produced by locating the feeding capillary in front of another, both placed inside an external tube through which the focusing current is injected [412]. In the so-called non-embedded coflow-focusing configuration [413], a converging nozzle is placed in front of a collector tube to produce microemulsions in the dripping and jetting modes.

Different injection methods have been proposed to enhance the tip streaming stability in flow focusing. One of the essential ideas is to eliminate the recirculation pattern arising in the meniscus of the original configuration, which seems to stabilize the flow [40, 351, 414]. Stable jets with diameters down to 2.9 μm were emitted at speeds up to 80 m s^{-1} using conical tips and focusing the liquid with Helium [415].

9.5.2. Flow focusing applications

The configurations mentioned above include the focusing of liquid streams with either a high-speed gaseous current or another liquid stream with a similar velocity. Gaseous flow focusing has several important applications. Among them, it is of special relevance its use as a sample delivery system in the Serial Femtosecond Crystallography [58, 416], which has revolutionized the molecular determination of complex biochemical species by avoiding radiation damage through femtosecond-duration X-ray pulse (Fig. 45). Sub-micron jets with speeds exceeding 160 m/s have recently produced with gaseous flow focusing [377], which enables the use of megahertz Serial Femtosecond Crystallography repetition rates.

Gaseous flow focusing has also been used to produce

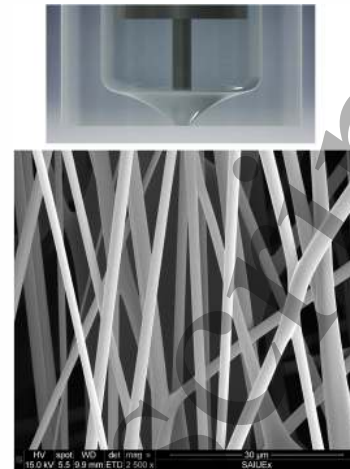


Figure 46: SEM images of fibers produced with gaseous flow focusing for a flow rate $Q = 5 \text{ ml/h}$ and an applied pressure drop $\Delta P = 115 \text{ mbar}$ [421]. The ejector is shown in the upper image. The liquid was a solution of 10 wt % of PVP in ethanol. The average diameter is 1.87 μm and the standard deviation is 0.7 μm .

microparticles of complex structures [5, 31, 419] by injecting coaxially two immiscible liquid streams [31]. More recently, the same principle has been applied to form viscoelastic threads [236, 420] for smooth printing and bioplotting [237], and to fabricate fibers with diameters ranging from a few microns down to hundreds of nanometers [421, 422] (Fig. 46). Si et al. [423] have developed a gaseous co-flow focusing process to produce stimuli-responsive microbubbles that comprise perfluorocarbon suspension of silver nanoparticles in a lipid. Gaseous flow focusing has been implemented not only in the original axisymmetric configuration but also in 2D and 3D geometries [424].

Gaseous flow focusing offers several attractive advantages over other atomization methods. One of them is that the collimated droplet streams acquire the velocity of the outer gas current in times of the order of $t_s = \rho_l d_d^2 / (18 \mu_g)$, where d_d is the droplet diameter and μ_g the gas viscosity. This means that a micrometer water droplet in a co-flowing subsonic air stream moving at the speed, say, $U_g = 200 \text{ m/s}$ can reach kinetic energies (per unit volume) as high as 20 MPa within distances from the source as small as $t_s U_g \sim 1 \text{ mm}$.

Electro-flow focusing [425] is a combination of electrospray and flow focusing where a relatively small voltage is applied to the focused liquid to charge the droplets produced via flow focusing. These droplets, with the proper combination of size, speed, and electrical charge, are perfect candidates for applications such as surface sample desorption [264, 426].

The liquid-liquid flow focusing configuration has received more attention than the gaseous one because of its very diverse applications. Here, we list some of them. Lee et al. [427] built a flow cytometer by focusing a liquid stream injected together with an outer one, both flowing across coaxial converging nozzles. Axisymmetric liquid-liquid flow focusing was proposed for the encapsulation and release of actives in the pioneering work of Utada et al. [21] and subsequent experimental studies [43, 428]. Tsuda et al. [429] described a method based on axisymmetric flow focusing to produce monodisperse cell-encapsulating microgel beads composed of a self-assembling peptide gel for 3D cell culture. Biodegradable Poly(Lactic Acid) particles have been fabricated using this technique [410]. Double flow focusing has been successfully used to produce monodisperse multiple-emulsions [430, 431], which are ideal microreactors or fine templates for synthesizing advanced particles [432]. Gu et al. [48] have reviewed the use of liquid-liquid flow focusing to produce emulsions with high throughput for encapsulation, chemical synthesis and biochemical assays. Wu et al. [433] have proposed multiplex coaxial flow focusing for single-step fabrication of multicompartment Janus microcapsules.

The applications of the liquid-liquid flow focusing are not limited to the fields mentioned above and can be extended to many others. For instance, the multiple-emulsions produced with a variant of this technique also allow the formation of PDMS microcapsules with tunable elastic properties [434]. Zhu et al. [435] have manufactured multi-compartment polymeric microcapsules in an axisymmetric flow focusing device for magnetic separation and synergistic delivery. Micrometer fibers can be formed when a viscoelastic liquid is focused with a Newtonian one [235, 436] or a viscoelastic stream [437].

Single-step generation of multi-core double emulsion droplets can be achieved by a specific class of axisymmetric flow focusing [433]. Utada et al. [21] first assembled a counter-current double emulsion flow focusing device by aligning glass capillaries. This configuration has been recently examined experimentally by Nabavi et al. [438]. Monodispersed emulsions down to $2\ \mu\text{m}$ in size were produced at a frequency of 20 kHz by using a similar configuration, the so-called “impinging flow-focusing” [439]. The counter-current flow focusing can exhibit a second-order transition which leads to extremely thin jets [440], which gives rise to silicone oil emulsions with a submicron particle radius.

9.5.3. Flow focusing dimensionless numbers

Two geometrical parameters enter the problem owing to the existence of a discharge orifice in flow focusing: the orifice diameter D_o and the orifice-to-capillary distance H . The diameter D_o is frequently chosen as the characteristic length because it determines the size of the region where the focusing effect takes place. Among the dimensionless parameters characterizing the flow focusing device, the ratio $\hat{H} = H/D_o$ is the most important because it considerably affects the meniscus slenderness and, therefore, its stability [185]. The ratio $2R_i/D_o$ generally takes values around unity and is not typically taken into account. The ratio (58) between the radii of the feeding and outer capillaries has little influence on the flow focusing effect, and is not considered in the analysis either.

The non-geometrical dimensionless numbers characterizing the Newtonian liquid-liquid flow focusing configuration are typically the same as those of a coflowing device, i.e., the outer Capillary number Ca_o [Eq. (57)], or the flow rate ratio Q_r [Eq. (59)], and the viscosity ratio μ . Inertial effects can be important in flow focusing because larger speeds can be reached. For this reason, the Reynolds number or the Weber number may enter the problem too. The density ratio always takes values of the order of unity, and, therefore, it plays a secondary role in the analysis.

The focusing of a liquid stream by an outer high-speed gas current [18] constitutes a phenomenon considerably different from that in the liquid-liquid case. The pressure drop ΔP caused by the gas acceleration becomes the force driving the liquid ejection in front of the discharge orifice. In the so-called monosized dripping mode [24], the magnitude of this force is quantified through the ratio of the pressure drop ΔP to the capillary stress σ/R_i , i.e.,

$$\mathcal{P} = \frac{R_i \Delta P}{\sigma} = \frac{R_i}{d_\sigma}, \quad (60)$$

where $d_\sigma = \sigma/\Delta P$. The steady jetting regime is typically analyzed considering the parameter plane defined by the Reynolds and Weber numbers

$$\text{Re}_{\text{FF}} = \frac{\rho_i V_{\text{FF}} R_{\text{FF}}}{\mu_i}, \quad \text{We}_{\text{FF}} = \frac{\rho_i V_{\text{FF}}^2 R_{\text{FF}}}{\sigma}, \quad (61)$$

where $V_{\text{FF}} = Q_i/(\pi R_{\text{FF}}^2)$ and

$$R_{\text{FF}} = \left(\frac{\rho Q_i^2}{2\pi^2 \Delta P} \right)^{1/4} \quad (62)$$

are the jet's velocity and radius calculated in terms of the injected flow rate Q_i and applied pressure drop ΔP assuming mass and energy conservation [18, 33].

The formula (62) does not apply to viscoelastic liquids. In this case, $\hat{H} \gg 1$, which means that the focusing effect is confined within a region much smaller than the liquid thread formed between the feeding capillary and the discharge orifice. The axial stress generated by the air stream next to the orifice is transmitted upstream by the stretched polymers, providing the fiber with the necessary consistency to avoid its breakup. That axial stress survives downstream far away from the orifice so that the liquid thread flies freely in front of the discharge orifice along distances hundreds of times its diameter [236].

Focusing a gaseous stream with an outer liquid current leads to a monodispersed bubbling regime [22, 23, 441, 442]. The strong oscillatory character of this phenomenon suggests the use of the flow rate ratio Q_r as the major governing parameter. The flow is essentially inviscid, and the density ratio takes very small values. Therefore, neither the Reynolds number nor the density ratio comes into play.

9.6. Selective withdrawal and electrified films

The production of drops/bubbles does not necessarily require a feeding capillary through which the dispersed phase is injected. In the selective withdrawal technique, a lower liquid layer is withdrawn by an upper one, which is suctioned across a cylindrical tube placed in front of the interface between them [29, 345, 443–445]. The interface forms a hump in front of the tube due to the viscous stresses exerted by the upper-layer liquid. When the upper-layer flow rate exceeds a certain threshold, those stresses overcome the resistance offered by surface tension, and the hump emits from its tip a jet much thinner than the collector tube. This visco-capillary phenomenon is governed by the Capillary number [445]

$$Ca_o^{sw} = \frac{\mu_o Q_o}{4\pi \hat{H} \sigma}, \quad (63)$$

where μ_o and Q_o are the upper-layer viscosity and flow rate, respectively, and \hat{H} is the distance between the capillary and the undisturbed interface. The selective withdrawal technique can be applied to produce monodisperse emulsions of micrometer droplets resulting from the capillary breakup of the jet. It can also be used to coat microparticles present in the withdrawn liquid [29]. A confined selective withdrawal geometry has been used to produce bubbles [446], emulsions [176], double emulsions and nematic shells [447] (Fig. 47), and micro-sized PDMS particles [351] in the tip streaming regime. In this geometry, the dispersed phase is in-

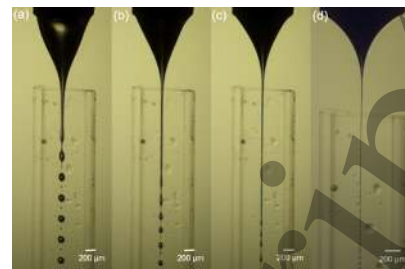


Figure 47: Shells produced with the confined selective withdrawal geometry for different speeds in the extraction tube. The shell diameter decreases as the speed decreases [447].

jected at a constant flow rate through a capillary/needle located in front of the collecting tube.

An electrohydrodynamic process analogous to the selective withdrawal takes place when an electrified collector tube is placed in front of a liquid film of finite conductivity [26, 360]. For small applied voltages, the free surface forms a hump in front of the tube owing to the action of the electric stresses. Above a certain critical voltage, the hump ejects a very thin liquid thread that moves into the tube. In this technique, the role of the Capillary number Ca_o^{sw} [Eq. (63)] is played by the electric Bond number χ [Eq. (55)].

10. Dripping and bubbling

We devote this and the next section to present some of the major results obtained using the droplet continuous production methods described above. We consider the dripping/bubbling and jetting modes separately. In each of those modes, we will distinguish the direct ejection method from that reached via tip streaming. Droplets/bubbles and jets are formed right after the feeding capillary in the former case. In tip streaming, the fluid is directed by some external actuation towards the tip of a deformed film, drop or stretched meniscus attached to a feeding capillary. Then, that tip emits small drops/bubbles either directly (Fig. 4) or through the breakage of a very thin jet (Fig. 5). In many cases, there is a gradual transition between dripping/bubbling and jetting on one side, and between direct ejection and that taking place via tip streaming on the other side. Then, the distinction between the different ejection modes is not always evident.

10.1. Direct dripping and bubbling

As mentioned in Sec. 9.2, gravitational dripping/bubbling is obtained for sufficiently large Bond

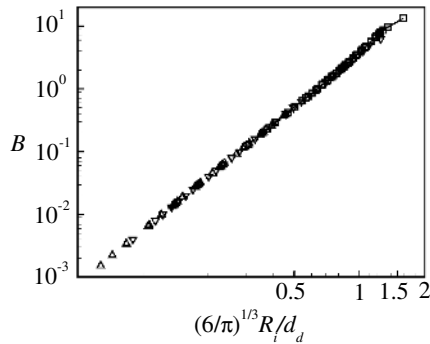


Figure 48: Diameter d_d of the primary droplet falling down from a vertical capillary as a function of the gravitational Bond number B [448]. The squares, up-triangles and down-triangles correspond to the experimental data obtained by Harkins and Brown [449] and Wilkinson [450], and the 1D numerical simulations conducted by Yildirim et al. [448], respectively. The fitting to the data yields (64).

numbers and small enough Weber numbers. At the incipience of a drop formation, a nearly spherical volume of fluid hangs on a thin filament attached to the feeding capillary. This filament eventually becomes unstable and breaks up driven by the surface tension force. For sufficiently small Weber numbers, the quasi-static dripping and bubbling processes are identical. In this regime, monodisperse collections of droplets/bubbles are produced with sizes of the order of or much larger than that of the feeding capillary.

The diameter d_d of the primary droplet/bubble that quasi-statically falls down from the capillary is given by the approximate formula

$$\frac{d_d}{R_i} = \alpha B^{-\beta}, \quad (64)$$

where $\alpha \simeq 4.46$ and $\beta \simeq 0.356$ [448] (Fig. 48). In the drop weight method for measuring the interfacial tension [449, 450], Eq. (64) provides the value of that quantity as a function of the droplet diameter measured in the experiment. There is a clear similarity between Eqs. (50) and (64), which characterize the instability conditions for droplets under the action of an electrical field and the gravitational force, respectively.

As the Weber number increases, dripping and bubbling become significantly different. Dripping evolves from a period-1 response to jetting, either directly or through several period doubling (halving) bifurcations [206]. On the contrary, bubbling persists producing bubbles with diameters d_b which depend on the injected gas flow rate Q_i as [23]

$$d_b \propto Q_i^{2/5}. \quad (65)$$

For sufficiently large values of the electric Bond number χ , a quasi-static dripping regime similar to the gravitational one can be produced in the absence of gravity. Consider a conductor droplet anchored to a feeding capillary placed on a face of a circular parallel-plate capacitor. If the intensity of the electric field is progressively increased, the droplet will detach from the capillary for $\chi \gtrsim 0.3$ [365].

A complex scenario appears when dynamical effects arise in electrified dripping. If the electric potential is increased while keeping the flow rate constant, the frequency of droplet formation increases and the drop volume decreases. If the electric Bond number is further increased, an electrified meniscus forms and emits varied liquid shapes operating in several periodic and aperiodic pulsating modes [451]. The periodic modes are the so-called electro-dripping, spindle, and intermittent cone-jet modes. A detailed description of them can be found in the recent review by Rosell-Llompart et al. [378]. Electrified dripping can also be produced by applying AC electric fields with characteristic times much larger than those of the system [452–456].

Viscous stresses exerted by the outer liquid stream in the coflowing configuration detach droplets from the feeding capillary in the dripping regime. For small values of the outer-to-inner flow rate ratio, Q_r , drop formation occurs in a slug flow regime in which drops are elongated axially and occupy almost the entire cross-section of the outer tube before their ejection. For larger flow rate ratios, the system adopts a proper monodisperse dripping regime [457]. The volume of the emitted droplets decreases as Q_r increases [16, 457].

In a typical gas-liquid coflowing configuration, the gas is injected with a velocity larger than that of the outer liquid stream, which leads to the periodic formation of bubbles near the nozzle exit [458]. The bubble diameter is typically larger than that of the nozzle. For a given velocity ratio, the bubbles produced when the injection pressure is kept constant are larger than those formed under the constant gas flow rate condition [53]. For outer stream velocities similar to that of the gas injection, the jetting regime can be produced [407]. Gaseous filaments can be elongated and pinched in converging microchannels [459]. The existence of a coflowing stream hinders the coalescence of bubbles, which constitutes an important technological advantage.

10.2. Dripping and bubbling from tip streaming

Gravity alone does not seem to be capable of producing dripping or bubbling from tip streaming, probably because of its inability to focus the flow towards the tip. du Pont and Eggers [460] conducted a nice experiment

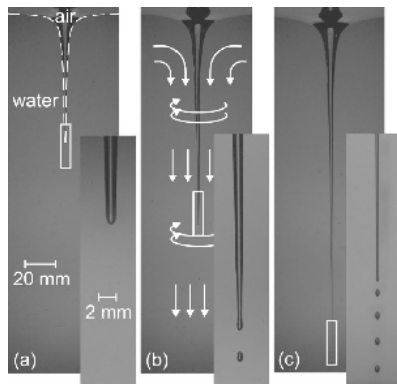


Figure 49: Bathtub vortex formed when the container rotates at 13.5 rpm (a), 24 rpm (b) and 30.5 rpm (c) [462].

where microbubbles were formed when the interface between a viscous liquid and air was deformed by a sink flow to form a sharp tip. Experiments did not elucidate whether bubbles were produced in the bubbling or jetting mode. This configuration can be categorized as a variant of selective withdrawal driven by gravity.

Gravity combined with the centrifugal force arising in a rotating cylindrical container produces a “bathtub vortex” as the liquid drains out through a small hole [461, 462]. Bubbling from tip streaming takes place at the tip of the needle-like surface depression for sufficiently high rotation speeds (Fig. 49). The frequency of bubble formation increases and the bubble size decreases as the rotation speed increases.

Under certain operational conditions, the tip of an electrified meniscus can drip [93, 463], giving rise to a monodisperse collection of microdrops with diameters much smaller than that of the feeding capillary. Hijano et al. [94] produced drops using this procedure with diameters down to $0.1R_i$. The diameter and generation frequency of the microdrops can be controlled by appropriately selecting the flow rate and applied voltage [464].

The planar liquid-liquid flow focusing configuration has been massively used since Anna et al. [19] implemented this technique using microchannels. In most cases, this configuration works in the dripping/bubble mode to produce emulsions [19], microparticles [465] and bubbles [466] with a very high degree of monodispersity. The use of the corresponding axisymmetric configuration has been much less frequent [49].

Utada et al. [21] applied the flow focusing principle to produce double emulsions in both the dripping and jetting regimes in glass micronozzles. The transition between the two regimes took place for Capillary numbers

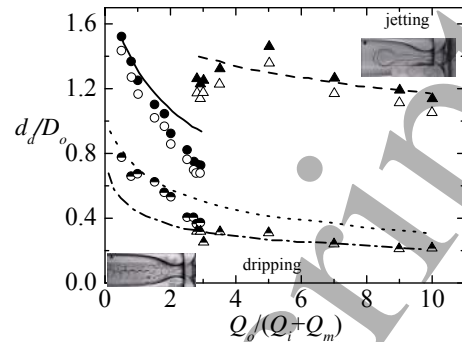


Figure 50: Diameter d_d of the droplets produced in a flow focusing device in terms of the orifice diameter D_o as a function of the outer liquid flow rate Q_o divided by the sum of the inner and middle liquid flow rates, $Q_i + Q_m$ [21]. The half-filled, white and black circles correspond to the precursor liquid thread diameter and the inner and outer droplet diameters in the dripping regime, respectively. The dotted and solid lines are the theoretical predictions (67) and (66) for the liquid thread and outer droplet diameter in this regime, respectively. The half-filled, white and black triangles correspond to the precursor jet diameter and the inner and outer droplet diameters in the jetting regime, respectively. The dashed-dotted and dash lines are the predictions for the liquid thread and outer droplet diameter [Eq. (74)], respectively.

around unity. The diameter d_d of the droplets produced in the dripping mode was estimated as

$$d_d \approx 1.9d_j, \quad (66)$$

where d_j is the diameter of the short liquid thread formed at the discharge orifice. This quantity can be easily estimated from the continuity equation assuming a flat velocity profile,

$$Q_r^{-1} + 1 = \frac{d_j^2}{D_o^2 - d_j^2}. \quad (67)$$

Interestingly, Rayleigh’s prediction (66), commonly used to predict the droplet diameter in the jetting mode, satisfactorily fitted experimental data of the dripping mode too [21], which indicates the sometimes subtle difference between the two regimes. The droplet inner diameter was slightly smaller than the outer one. Figure 50 shows the diameters of both the precursor liquid thread and the resulting droplets as a function of the outer liquid flow rate Q_o divided by the sum of the inner and middle liquid flow rates, $Q_i + Q_m$. The transition from the dripping to the jetting regime takes place for $Q_o / (Q_i + Q_m) \approx 0.3$.

The axisymmetric flow focusing configuration was originally conceived to produce droplets from the breakage of a liquid jet expelled due to the action of a high-speed gas stream [18]. However, Cruz-Mazo et al. [24]

have been recently shown that monodisperse dripping can also be obtained within relatively narrow intervals of viscosities, injected flow rates and applied pressure drops. In this regime, the applied pressure drop is balanced by the local acceleration of the fluid particle, which yields the scaling law for the droplet diameter

$$\frac{d_d}{R_i} = 2.4\mathcal{P}^{-1/2}. \quad (68)$$

This monosized dripping mode of axisymmetric flow focusing has been found for viscosities $1 \lesssim \mu \lesssim 25$ mPa, and leads to diameters smaller than that of the feeding capillary in most cases [24]. The ejection process differs substantially from that taking place in the micro-dripping mode of electrospray, where the electrified meniscus stretches and shrinks more notably.

As explained in Sec. 4, gaseous jets injected into a quiescent pool of liquid are prone to absolute instability owing to the high values of the capillary wave velocity. For this reason, most flow focusing experimental realizations produce bubbles in the bubbling mode [22]. The bubble diameter can be obtained by assuming that the unsteady and convective terms of the momentum equation for the gas phase are commensurate with each other, which yields [23]

$$\frac{d_b}{D_o} = 1.1Q_r^{-0.4}. \quad (69)$$

This scaling law remarkably agrees with experimental data obtained using both the plate-orifice [23] and nozzle [442] configurations (Fig. 51). Jensen et al. [441] analyzed numerically the bubbling in an axisymmetric flow focusing device. The results for the bubble volume were consistent with those obtained experimentally by Garstecki et al. [466] for the 2D topology.

11. Jetting

11.1. Direct jetting

11.1.1. Gravitational direct jetting

Capillary liquid jets can be formed by simply ejecting liquid across a vertical feeding capillary at high enough Weber numbers. Clanet and Lasheras [467] extended Taylor's model [468] for the recession speed of a free edge to obtain the critical injection velocity leading to the dripping-to-jetting transition in an inviscid gravity-driven flow. The Weber number above which dripping gives rise to jetting is given by the expression

$$\text{We}_i = 2\left(\frac{B_o}{B}\right)^{1/2} \left\{ 1 + K(B_o B)^{1/2} - \left[(1 + K(B_o B)^{1/2})^2 - 1 \right]^{1/2} \right\}^2, \quad (70)$$

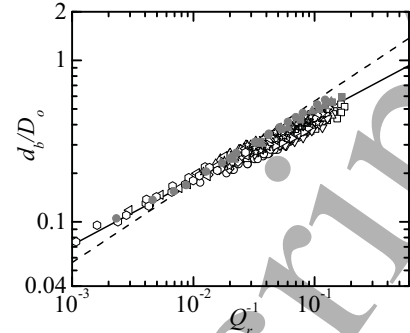


Figure 51: Diameter d_b/D_o of the bubbles produced with flow focusing as a function of the flow rate ratio Q_r [442]. The white and grey symbols correspond to experiments conducted with the plate-orifice [23] and nozzle [442] configuration, respectively. The solid and dashed lines correspond to Eq. (69) and $d_b/D = 1.77Q_r^{-0.5}$, respectively. The latter can be regarded as the version for this configuration of the classical flow-focusing formula [18].

where B_o is the Bond number based on the outer radius of the feeding capillary, and K is a dimensionless constant which depends on the fluids involved ($K = 0.72$ for water injected in the air). The viscosity of both the inner and outer fluids can significantly modify this result [469]. The gravitational dripping-to-jetting transition has also been analyzed in terms of the global stability of the base flow calculated from the 1D approximation (see Sec. 2.4) [159, 161].

For flow rates sufficiently larger than the minimum leading to jetting, the liquid jet adopts a slender shape which can be accurately described by the 1D model [62]. If one neglects the surface tension force, the exact solution of this model is [470, 471]

$$v = \frac{2^{-1/3}\text{Ai}^2(r)}{\text{Ai}'^2(r) - r\text{Ai}^2(r)}, \quad r = 2^{-1/3}(x - k), \quad (71)$$

where $v = w/v_0$ and $x = z/L_0$ are the velocity and distance to the feeding capillary scaled with $v_0 \equiv (L_0 g)^{1/2}$ and $L_0 \equiv 3^{2/3}(\mu_i^2/\rho_i^2 g)^{1/3}$, respectively [470]. In addition, Ai and Ai' are the Airy function and its derivative, respectively, and $k = 2.9455 \dots$ is the first zero of $\text{Ai}(-k/2^{1/3})$. Intriguingly, the power of this solution has been hardly exploited to date in microfluidics.

Javadi et al. [138] examined the breakup of a viscous gravitational jet using a WKB-type approach, in which disturbances locally have the form of plane waves. They showed that viscosity plays completely independent roles in the axial momentum balance of the steady base state and in the growth of perturbations about that state. Specifically, viscosity does affect the perturbation growth rates, although it does not influence the base

flow in most of the jets formed in many experiments. The same idea underlies, for instance, the stability analysis of a viscous electrified jet emitted in the cone-jet mode of electrospray [142].

The breakup length of a falling viscous jet can be estimated from the natural extension of Eqs. (31) to an accelerated jet. In the high-viscosity limit, the growth rate ω_i of an axisymmetric perturbation scales as the inverse of the viscous-capillary time (38). Because most of the jet accelerates in the inertial regime, $R_j \sim (Q_i^2/gz)^{1/4}$ and $t_f \sim (z/g)^{1/2}$, where z is the distance to the nozzle exit and t_f the time for a fluid element to reach that distance. Considering the scalings for R_j and t_f , and the visco-capillary time (38), one derives a simple scaling law for the jet breakup length:

$$l_b \sim \left(\frac{g Q_i^2 \mu_i^4}{\sigma^4} \right)^{1/3}. \quad (72)$$

The comparison between the prediction (72) and experimental data shows remarkable agreement when the base flow is dominated by inertia (Fig. 52).

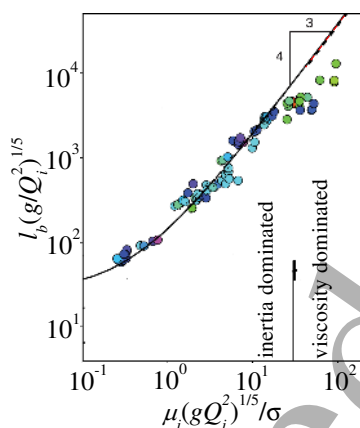


Figure 52: Breakup length l_b measured experimentally (symbols) and calculated theoretically (solid line) [138]. The dashed line is the prediction (72) for the high-viscosity limit.

11.1.2. Electrified direct jetting

When a liquid is emitted through a feeding capillary at Weber numbers in the range 1-10, the classical jetting regime is obtained. This regime can be manipulated by applying an electrical potential to the feeding capillary, which leads to the so-called simple-jet mode of electrospray [378, 472, 473]. For relatively small values of the electric Bond number χ [Eq. (55)], this mode does not substantially differ from the non-electrified case in terms of the jet diameter and velocity, breakup distance,

and size of the emitted droplets. The major effect is that Ohmic conduction charges the jet's free surface. That charge accumulates in the droplets resulting from the varicose jet breakup. As the electric Bond number increases, the electrostatic repulsion experienced by the droplets forms a plume [472]. Above a critical electric Bond number, which grows with the Weber number, the transition from axisymmetric breakup to whipping takes place.

11.1.3. Coflowing direct jetting

Liquid-liquid coflowing devices normally operate either in the direct dripping mode or in the direct jetting regime. Cramer et al. [401] showed experimentally that the limiting length of drops produced in these devices increases as the flow rate of the outer fluid increases. When this parameter exceeds a certain threshold (while keeping the rest constant), the system experiences a transition from dripping to jetting. The size of the droplets produced by a coflowing device in the jetting mode can simply be derived by neglecting inertia. In this case, the velocity profiles of both the continuous and dispersed phases are parabolic, and the dominant perturbation wavelength can be estimated from Tomotika's dispersion relationship [212]. Using these two ingredients, one obtains, for instance, $d_d/D_o = 1.44 Q_r^{-1/2}$ for $\mu = 1$ [474].

In the jetting regime of the coflowing configuration, the jet tapers directly from the feeding capillary, and, therefore, the system stability reduces to that of the jet itself. Guillot et al. [148] identified three dimensionless parameters governing the system behavior at low Reynolds numbers. The critical (re-defined) Capillary number for the convective-to-absolute instability transition (Sec. 3) marks the border between the dripping and jetting modes [148]. The global stability analysis leads to almost the same results for sufficiently high external flow rates [162].

Utada et al. [187] experimentally found that the dripping-to-jetting transition in coflowing liquid streams with moderate Reynolds numbers can be characterized by a state diagram that depends on both the Weber number We_i of the inner fluid and the Capillary number Ca_o of the outer one (Fig. 53). Dripping takes place when both parameters take small enough values, while jetting is obtained if the sum $Ca_o + We_i$ is at least of order unity, i.e. when inner inertia plus outer viscosity overcomes surface tension. The produced jets can either narrow or widen downstream depending on the values of Ca_o and We_i (Fig. 53). For Weber numbers at least of order unity, jets in the widening mode break up due to an absolute instability occurring for sufficiently

small values of Ca_o [175]. This instability produces droplets with diameters much larger than that of the precursor jet. Castro-Hernández et al. [32] found that the droplet diameter in both the narrowing and widening regimes can be approximately obtained from (31)-right, the only difference resides in the dependence of λ^{\max} and d_j on the governing parameters.

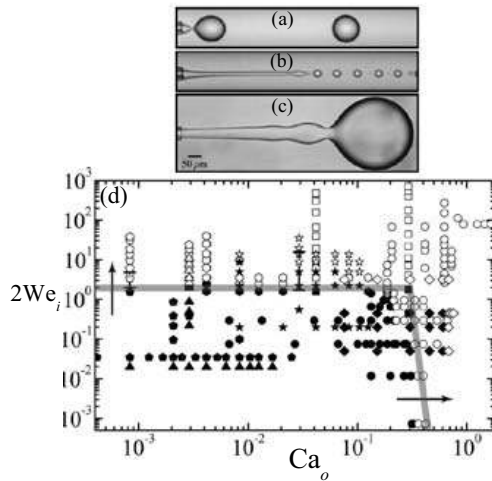


Figure 53: Dripping (a), narrowing (b) and widening (c) regimes. State diagram showing the dripping (solid symbols) and narrowing/widening (open symbols) experimental realizations for varied liquid-liquid configurations (d) [187].

The diameter of the bubbles produced in the jetting mode of a gas-liquid coflowing device can be estimated by assuming negligible inertia [474]. In this case, the bubble volume is calculated from the conservation of mass during the gaseous jet breakup under constant flow rate conditions, which gives

$$d_b \sim Q_r^\beta, \quad (73)$$

where the exponent β ranges from -0.5 to $-5/12$. These values correspond to the limits $Q_r^{-1} \rightarrow 0$ and $\mu^{-1} \rightarrow 0$, respectively. The exponent $-5/12$ has been observed experimentally by Castro-Hernández et al. [169].

11.1.4. Flow focusing direct jetting

Utada et al. [21] studied the jetting regime arising in the axisymmetric liquid-liquid flow focusing configuration for Capillary numbers Ca_o [Eq. (57)] larger than unity (Fig. 50). The formation of droplets in this regime was similar to that caused by the end-pinching mechanism rather than to the Rayleigh capillary instability (see Sec. 5). The droplet diameter d_d was calculated by assuming that the droplet is inflated by the precursor jet

during a time which scales with the viscous-capillary time (38). This leads to the expression

$$d_d = \left[\frac{60(Q_i + Q_o) d_j \mu_o}{\pi \sigma} \right]^{1/3}, \quad (74)$$

where d_j can be obtained from mass conservation by assuming parabolic velocity profiles [21]. The slowing down of the outer stream caused by the diverging character of the nozzle made the jet break up at a fixed location [475], which resulted in higher monodispersity degrees [189].

Figure 50 shows both the diameters of the precursor liquid jet and the inner and outer diameters of the resulting droplets formed in the double-emulsion flow focusing device developed by Utada et al. [21]. The dash-dotted and dashed lines are the predictions obtained from mass conservation and Eq. (74), respectively. The experimental results show that the liquid thread diameter in the dripping regime smoothly evolves into that of the jetting mode. The small difference between the trends in the two cases may be attributed to the development of the velocity profile rather than a true bifurcation. The dripping-to-jetting transition at $Q_o/(Q_i + Q_m) \approx 0.3$ becomes apparent due to the sharp increase of the ratio of the droplet diameter to that of the precursor thread.

When a viscoelastic stream is focused by a Newtonian outer current, the tensile stresses generated by the stretched polymers preclude the formation of a proper tip streaming regime. On the contrary, the viscoelastic liquid forms a slender jet which accelerates progressively until crossing the discharge orifice [235, 236, 436]. The outer stream keeps the dissolved polymers stretched, increasing the jet's extensional viscosity. This effect favors the damping of the varicose free surface perturbations.

11.2. Jetting from tip streaming

11.2.1. Gravity-driven steady tip streaming

A natural question is whether steady tip streaming can be produced by simply ejecting a liquid thread in a passive ambient under the action of the gravitational force. This force does not seem to be able to produce accelerations sufficiently localized to give rise to such a phenomenon. In fact, the recirculation patterns characteristic of tip streaming [346] cannot be produced by the gravity mass force. However, liquid shapes fairly similar to some of those regarded as tip streaming can be found very close to the system's global stability limit [161].

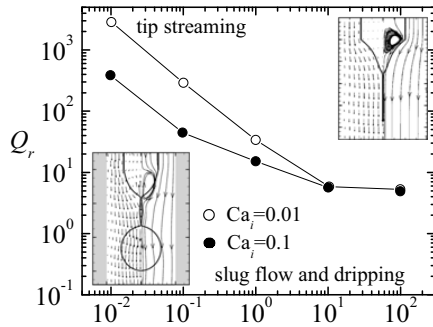


Figure 54: Critical value of the flow rate ratio Q_r as a function of the viscosity ratio μ calculated numerically [16].

As described in Sec. 10, gaseous tip streaming can also be produced by a variant of selective withdrawal driven by the gravitational force [460]. In this case, microbubbles only form when the tip is allowed to enter the tube. We will come back to this point in Sec. 11.2.3.

11.2.2. Coflowing steady tip streaming

Suryo and Basaran [16] analyzed the transition from dripping to tip streaming in a coflowing configuration. Viscous stresses exerted by the outer liquid increase as the ratio Q_r of the outer flow rate to the inner one increases. For sufficiently large values of this quantity, those stresses make the growing drop adopt a conical shape within which a recirculation pattern appears. For a relatively narrow region of the parameter space, a jet with a radius a few orders of magnitude smaller than that of the feeding capillary emanates steadily from the drop tip [32, 139]. Simple scaling analyses show that this transition takes place for [16]

$$Q_r \gtrsim (\mu Ca_i)^{-1}. \quad (75)$$

Numerical simulations agree with this prediction for small μ (Fig. 54). For moderate and large values of this parameter, the transitional flow rate ratio becomes independent of the viscosity ratio.

Gordillo et al. [139] concluded that the parameter conditions to obtain monodisperse micro-emulsions via tip streaming in coflows are those leading to the asymptotic global stability of this flow. It worths mentioning that it is not simple to distinguish tip streaming in a coflowing configuration from the narrowing jetting regime described in Sec. 11.1. In some experimental configurations, there seems to be a gradual transition from one mode to another, rather than a sharp steady flow bifurcation. This kind of bifurcation does take place in other tip streaming configurations. In fact,



Figure 55: Selective withdrawal for $\mu_i/\mu_o = 0.005$ and 20 [444].

Dong et al. [440] has recently introduced the concept of *second-order transition* to describe this phenomenon in a variant of flow focusing, which provides an intriguing insight into the physics of the problem.

11.2.3. Selective withdrawal steady tip streaming

Selective withdrawal has been studied on fewer occasions than other techniques such as electrospray or flow focusing. Cohen et al. [29] proposed selective withdrawal to coat small particles with polymer films. The method proved to be flexible in terms of the chemical composition and thickness of the conformal coatings.

The force exerted by the withdrawal stream produces a hump of the interface for flow rates smaller than that leading to tip streaming. Lister [443] modeled the flow in this configuration through a point sink in a two-layer unbounded system in which viscous forces dominate. In this way, he determined the conditions for the fluids to be withdrawn. Cohen and Nagel [476] showed that the steady-state profiles for humps at different flow rates and tube heights can be scaled onto a single similarity profile. This profile does not depend on the lower fluid viscosity [477]. Case and Nagel [444] discussed the influence of the viscosity ratio on the diameter of the spout at the transition. True tip streaming can be produced only for sufficiently small values of the lower-to-upper viscosity ratio (Fig. 55). Due to its local character, the flow in selective withdrawal exhibits universal features next to the interface tip [345].

In the classical selective withdrawal configuration, the tip formed by the dispersed phase does not enter the tube. du Pont and Eggers [460] showed that in this case a gaseous tip never becomes unstable. Their numerical simulations [345] for this configuration agreed remarkably well with the experiments [460]. Zhou and Feng [478] examined the role played by the polymer stress in the viscoelastic case. They found that there is a critical transition where the surface forms a cusp from which an air jet emanates toward the suction tube.

There has been certain controversy about the mechanism causing tip streaming in selective withdrawal. According to Blanchette and Zhang [445], the transition is not determined by the local flow in the interface tip, but

by a global balance between the upward force exerted by the withdrawal flow and the downwards force owing to interfacial tension. A similar idea was proposed by Montanero et al. [348] to explain the critical conditions for tip streaming in gaseous flow focusing operating with viscous liquids. The theory of Blanchette and Zhang [445] assumes that the failure of the interface is insensitive to the nature of the entrained phase. According to Eggers and du Pont [479], this assumption is not valid because there is no transition if the entrained phase is air, something corroborated by the experiments of Zhou and Feng [478].

The strong stretching experienced by the simple or compound liquid jets in confined selective withdrawal (Fig. 47) allows reducing the critical Capillary number above which steady tip streaming is obtained [176]. The diameter of the bubbles generated with this configuration have been calculated in terms of the Weber and Reynolds numbers, and the gas to liquid flow rate ratio [446].

Electrospray and flow focusing are probably the two techniques most frequently used to produce jets via steady tip streaming. We devote the next two sections to these configurations.

12. Electrospray steady tip streaming

12.1. The DC cone-jet mode of electrospray

Electrostatic fields have been used to spray liquids since the XVIIth century. In the most typical configuration of electrospray, the liquid is injected into a passive dielectric medium across a metallic capillary hundreds of microns in diameter at flow rates in the range 10^{-3} -10 ml. One imposes in the feeding capillary an electric potential of the order of kilovolts with respect to a grounded electrode located some millimeters downstream from the capillary. When both the liquid properties and control parameters are selected adequately, the cone-jet mode of electrospraying is obtained. This flow is a way to escape the singularity arising in the tip of the so-called Taylor cone, which results from the exact static balance between surface tension and electric forces. Among the varied electrospray regimes [93], the cone-jet mode has attracted attention because of its applicability in very diverse fields. The steady cone-jet is observed over a huge range of length scales. The increase of the conductivity allows reducing the jet diameter from tens of microns to a few nanometers [480, 481].

In the cone-jet mode, the meniscus adopts a stable quasi-conical shape whose apex steadily ejects a thin jet, which eventually breaks up into droplets due to capillary forces [197]. In general, the superficial charge

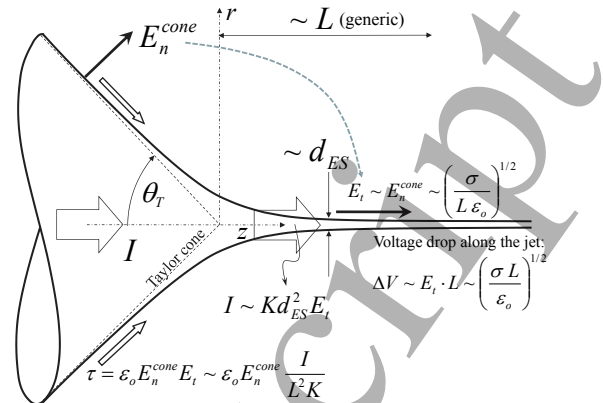


Figure 56: Sketch of the generic electrospray cone-jet configuration in which electrohydrodynamic steady tip streaming takes place. Its axial length scale L is small compared to the feeding capillary diameter.

is not relaxed to its electrostatic value within the cone-jet transition region [109, 111, 482, 483], so that inner electric fields arise in that region. However, those electric fields are not large enough to invalidate the scaling laws presented below.

Gañán-Calvo et al. [80] have recently reviewed both the conditions for the cone-jet mode to appear and the scaling laws for the droplet diameter d_d and emitted electric current I . The locality of the ejection process allows to describe it in terms of the liquid properties exclusively (independently of geometrical and electrical parameters). On this condition, the characteristic quantities of the problem are $d_{ES} = [\sigma \epsilon_o^2 / (\rho_i K_i^2)]^{1/3}$, $v_{ES} = [\sigma K_i / (\rho_i \epsilon_o)]^{1/3}$ and $I_{ES} = (\sigma K_i v_{ES} d_{ES}^2)^{1/2}$, and the dimensionless governing parameters are the relative permittivity ϵ , the electrohydrodynamic Reynolds number $\delta_\mu = \rho_i v_{ES} d_{ES} / \mu_i$, and the relative flow rate Q_i / Q_{ES} , where $Q_{ES} = v_{ES} d_{ES}^2$ [105, 132]. Naturally, the characteristic diameter and velocity d_{ES} and v_{ES} coincide with the corresponding quantities d_o and v_o introduced in Sec. 8 to describe the onset of electrospray. Figure 56 sketches the cone-jet mode of electrospray and the quantities involved in its analysis.

12.1.1. Droplet diameter and electric current

Most cone-jet mode realizations of electrospray correspond to the “I-E regime” identified by Gañán-Calvo [105], where the liquid electrical permittivity and viscosity have little influence on the outcome. In this regime, the scaling laws for the droplet diameter d_d and emitted electric current I are:

$$\frac{d_d}{d_{ES}} \simeq \left(\frac{Q_i}{Q_{ES}} \right)^{1/2}, \quad \frac{I}{I_{ES}} \simeq 2.5 \left(\frac{Q_i}{Q_{ES}} \right)^{1/2}; \quad (76)$$

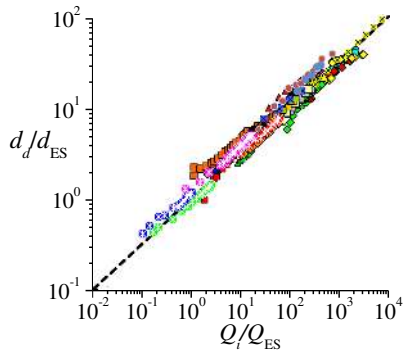


Figure 57: Diameter d_d of the droplet emitted in the cone-jet mode of electrospray and measured by different authors [80]. The dashed line is the scaling law (76).

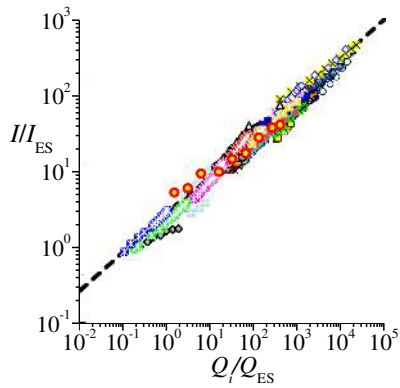


Figure 58: Current intensity I emitted in the cone-jet mode of electrospray and measured by different authors [80]. The dashed line is the scaling law (76).

or, in dimensional form:

$$d_d \approx \left(\frac{\rho_i \epsilon_0 Q_i^3}{\sigma K_i} \right)^{1/6}, \quad I \approx 2.5 (\sigma K_i Q_i)^{1/2}. \quad (77)$$

The scaling for the emitted current was first derived by Gañán-Calvo et al. [484], while that for the droplet was given by Gañán-Calvo [104]. Both scalings were also obtained from dimensional analysis [132] and numerical simulation [485]. These laws exhibit remarkable agreement with experimental data gathered from many authors (Figs. 57 and 58) [80]. Significant deviations from these laws can be expected in the viscous and polar regimes, corresponding to small and large values of δ_μ and β , respectively.

The scaling laws for the droplet diameter and current differ from those derived by Fernandez de la Mora and Loscertales [482], who assumed that the flow becomes a spherically symmetric sink in a region of the cone tip

with size of the order of d_j , and that the electric relaxation time is of the same order of magnitude as that of the fluid particle residence time in that region. This led these authors to include the permittivity of the liquid in their general scaling laws for electrospray. However, that is only valid for very polar liquids and close to the minimum flow rates for steady cone-jet mode, as shown by both experiments and dimensional analysis [105].

Gañán-Calvo and Montanero [33] showed that there is a simple analogy between electrospray in the I-E regime and gaseous flow focusing. The jet in electrospray is powered by an effective pressure drop

$$\Delta P = k_p \left(\frac{\sigma^2 K_i^2 \rho_i}{\epsilon_0^2} \right)^{1/3}, \quad (78)$$

where k_p is a constant of order unity. Interestingly, the pressure drop is not the major source of energy in many realizations of electrospray and gaseous flow focusing. However, its capacity to stretch the tapering meniscus tip and extrude the liquid filament from it renders this force an essential element of these two techniques.

12.1.2. Breakup length and whipping

The breakup length ℓ_b of a jet emitted in the cone-jet mode of electrospray has been estimated by using the approximation (31) and the maximum growth rate calculated by Saville [242] for a leaky-dielectric jet moving in an axial electric field [142]. The result for low and high Reynolds numbers is

$$\ell_b \approx 42 Z_v^{-1}, \quad \ell_b \approx 42 Z_i^{-1}, \quad (79)$$

respectively, where

$$Z_v \equiv \mu_i^{-1} \left[\left(\frac{\rho_i \sigma^5 \epsilon_0}{Q_i^3 K_i} \right)^{1/6} - \frac{1}{4\pi} \left(\frac{\rho_i^2 \sigma K_i}{\epsilon_0} \right)^{1/3} \right] \quad (80)$$

and

$$Z_i \equiv \left[\left(\frac{\sigma^5 \epsilon_0}{\rho_i^5 Q_i^9 K_i} \right)^{1/6} - \frac{1}{4\pi} \left(\frac{\sigma K_i}{\rho_i Q_i^3 \epsilon_0} \right)^{1/3} \right]^{1/2}. \quad (81)$$

The above theoretical predictions agree with experimental data of liquids with low polarity (Fig. 59). Using the scaling laws (77), Xia et al. [486] have found experimentally that whipping arises in the cone-jet mode of electrospray when the dimensionless number $G = \Gamma_e^2 \delta_\mu^{1/3}$ takes values above the threshold $G \approx 155$.

12.1.3. Minimum flow rate

The steady cone-jet mode of electrospray is adopted within a narrow parameter window [487, 488] (Fig. 60).

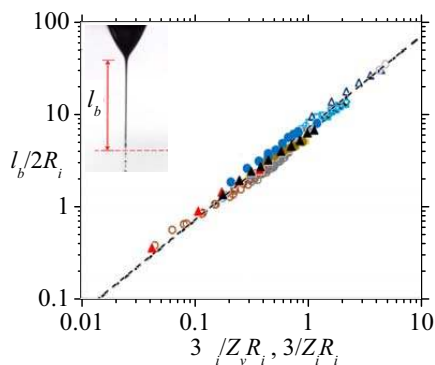


Figure 59: Experimental values of the breakup length l_b of a jet emitted in the cone-jet mode of electrospray for low (open symbols) and high (solid symbols) Reynolds numbers [142]. The dashed line is the law (79).

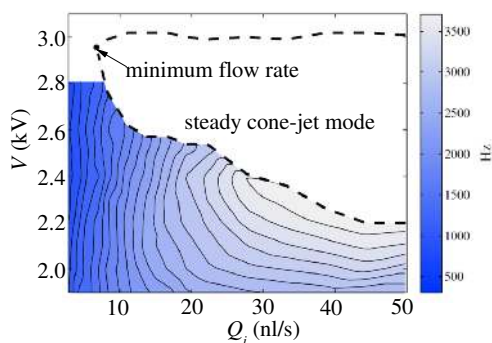


Figure 60: Parameter window for the steady cone-jet mode observed by Bober and Chen [488]. The contours show the frequency of the dripping mode (intermittent cone-jet) for flow rates below the minimum flow rate stability limit. The arrow indicates the absolute minimum flow rate for the configuration analyzed.

For a given applied voltage, if the flow rate falls below its minimum value, then the balance between the electric tangential stress driving the liquid ejection and the polarity/viscosity ones opposing it breaks down in the cone-jet transition region. As can be seen in Fig. 61, experimental results are consistent with the simple scaling laws

$$Q_{\min}/Q_{\text{ES}} \sim \varepsilon, \quad Q_{\min}/Q_{\text{ES}} \sim \delta_\mu^{-1} \quad (82)$$

for the minimum flow rate Q_{\min}/Q_{ES} of the cone-jet mode in the polar ($\varepsilon \gg \delta_\mu^{-1}$) and viscous ($\varepsilon \ll \delta_\mu^{-1}$) limits, respectively [358]. The figure also shows the stabilizing effect of the feeding capillary (Q_{\min}/Q_{ES} decreases as d_{ES}/R_i increases) [489].

Gamero-Castaño and Magnani [490] examined both experimentally and numerically the limit of the minimum flow rate of the cone-jet mode of electrospray. The major finding of their experiments is the fact that the

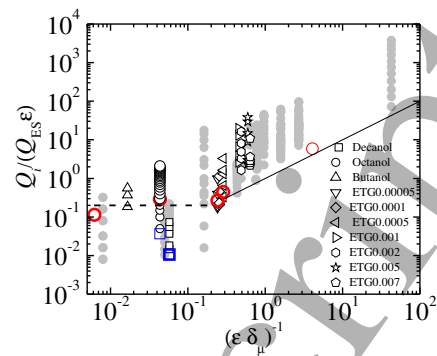


Figure 61: (Color online) Steady cone-jet mode realizations [109]. The grey symbols are the data gathered from different authors. The white symbols correspond to the experimental results obtained with a capillary $R_i = 105 \mu\text{m}$ in radius. The big white circles show the experiments conducted with 1-octanol and $R_i = 550 \mu\text{m}$. The red big circles and blue big squares are marginally stable basic flows corresponding to $R_i = 105 \mu\text{m}$ and $R_i = 550 \mu\text{m}$, respectively. The dashed and solid lines are the scaling laws $Q_{\min}/Q_{\text{ES}} = 0.2\varepsilon$ and $Q_{\min}/Q_{\text{ES}} = \delta_\mu^{-1}$ for the polar and viscous limits, respectively.

regime dominated by polarity was not reached even for realizations with $\varepsilon \gg \delta_\mu^{-1}$ because of the significant influence of viscosity in those cases. The numerical solution of the leaky-dielectric model allowed them to hypothesize that instability occurs because viscous dissipation takes place before shear electric stresses inject energy into the system.

Dharmansh and Chokshi [193] conducted the global linear stability analysis of a leaky-dielectric liquid in the framework of the 1D model. The jet thinning produces a stabilizing effect due to both the variation of the surface charge density and the extensional viscous stresses in the base flow. Ponce-Torres et al. [109] have recently shown that the minimum flow rate stability limit can be predicted from the global linear stability analysis of the solution to the full leaky-dielectric model (Fig. 61) [101].

Different methods have been proposed to stabilize the cone-jet mode in electrospray. These can be categorized into those modifying the applied electric field [491, 492] and the emitter geometry. In this latter case, use has been made of carbon fiber emitters [39], ballpoint pen nozzles [493] or hemispherical caps [494]. Cruz-Mazo et al. [195] have recently proposed a way to stabilize steady micro/nanoliquid jets issuing from Taylor cones by applying a coflowing gas stream. That stream is shown to promote the global stability of the Taylor cone-jet, thus reducing very significantly the minimum flow rate for a given set of geometrical parameters.

The maximum flow rate limit is very relevant in those applications where the droplet production rate must be

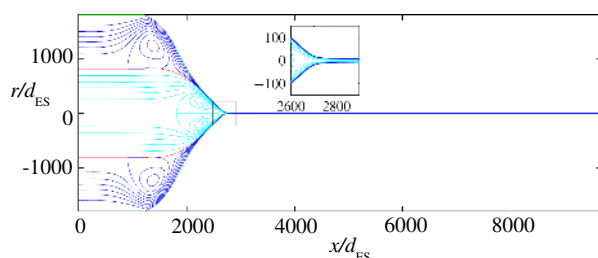


Figure 62: Shape and streamlines of a coaxial electrospray using deionized water and tributyl phosphate as the inner and outer fluids, respectively [500]. The inner and outer flow rates are 234 $\mu\text{l/h}$ and 60 $\mu\text{l/h}$, respectively, while the applied voltage is 4570 V.

maximized. Its analysis is complicated because it involves a wide variety of complex issues. The excess of the level of charge carried by the liquid jet limits the electric field on the cone surface [487, 495] and can cause the surrounding gas ionization. There can also be polarity effects related to the different mobility and nature of ions that transport the charge [496].

12.2. Coaxial electrospray

Coaxial electrified jets [25] have been produced in the cone-jet mode for producing complex fibers [497, 498], and, to a lesser extent, complex particles (see, e.g., [387]). The working modes of this configuration have been described by Chen et al. [499] in connection with those appearing in the single-phase electrospray. The ejection is driven by the liquid with the largest electrical conductivity, which typically is the external one. In this case, the differences between the coaxial and single-phase electrospray are minimal. In particular, the diameter of the compound jet is similar to that of the single-phase electrospray for the same flow rate as that of the driver, provided that the viscosities are commensurate with each other. López-Herrera et al. [500] have recently solved the 2D leaky-dielectric model for the cone-jet mode of coaxial electrospray (Fig. 62). They have shown an unexpected feature exhibited by this complex system: the possibility of the appearance of a segment of opposite charge (negative, if the polarity of the applied potential is positive, and vice versa) on the inner interface at the transition region.

12.3. AC electrospray

The cone-jet mode of electrospray can also be produced with AC electric fields at frequencies greater than 50 kHz. In this case, the cone is more slender and is sustained by the entrainment of net space free charge within the cone. This physical mechanism is completely different from that of DC electrospray, and cannot be

described in terms of the leaky-dielectric model [88]. AC electrospray can be used as an ionization source for mass spectrometry of biomolecules [90].

12.4. Electrospinning

Lauricella et al. [402] have recently reviewed the theoretical description and numerical simulation of electrospun jets from polymeric solutions, paying special attention to the critical role played by instability phenomena of electrical and hydrodynamic origin. Interested readers are referred to that excellent work to gain insight into the physical mechanisms governing the flow. Here, we only describe some results obtained from the global stability analysis of electrospinning.

When the electric field is applied to a viscoelastic liquid, the cone-jet mode of electrospinning can be produced [75–77, 79]. To analyze the linear stability of this mode, Dharmansh and Chokshi [194] extended their previous analysis for electrospray [193] incorporating rheological effects described by the Olroyd-B and XPP models. As in the Newtonian case, the results showed the stabilizing effect of the jet thinning. Blanco-Trejo et al. [163] have recently calculated the axisymmetric global modes of the cone-jet mode described by the 2D hydrodynamic equations and the Olroyd-B constitutive model. They have considered the physical properties of 1-octanol and added polymeric stresses characterized by relatively small relaxation times. The simulations of the base flow show that stress relaxation times of the order of some hundreds of microseconds are commensurate with the residence time in the cone-jet transition region. In this case, fluid particles undergo an extensional deformation in front of the meniscus tip intense enough for the dissolved polymers to continuously stretch, which prevents their relaxation to the coiling state. This produces axial polymeric stresses much larger than those caused by the solvent viscosity. These stresses pull from the liquid in front of the meniscus tip (Fig. 63). As a consequence, the liquid accelerates much faster than in the Newtonian case, which makes the electrified liquid meniscus shrink. The kinetic energy gained by the meniscus is lost in the jet region, where polymers relax to their coiling state. One may say that the liquid borrows energy from the polymers in the most unstable region and returns it when safely moving downstream. This stabilizes the flow and explains the reduction of the minimum flow rate. This theoretical study is just a first attempt to describe the electrospinning of viscoelastic liquids at a fundamental level. Factors like the possible anisotropy of electrical conduction or the finite extensibility of polymers must be taken into account in future studies.

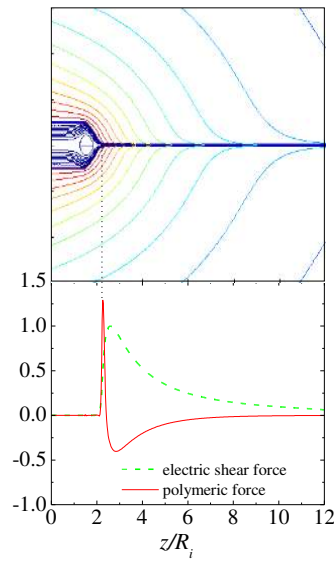


Figure 63: (Upper graph) Streamlines (inner domain) and equipotential lines (outer domain) calculated from the 2D leaky-dielectric Oldroyd-B model for $\varepsilon = 10$, $\delta_\mu = 2.29$, $Q_i/Q_{ES} = 7.72$, $\lambda_s^{(i)} = 2.656 t_e$ and $\lambda_r^{(i)} = 0.0926 \lambda_s^{(i)}$. (Lower graph) Electric shear force and polymeric force both per unit volume and normalized with the maximum value of the former [163].

13. Flow focusing steady tip streaming

13.1. Liquid-liquid flow focusing

Liquid-liquid flow-focusing devices induce a strong hydrodynamic focusing effect in front of the discharge orifice owing mainly to the action of high viscous stresses in that region, which favors the transition from dripping to steady tip streaming. In fact, the steady tip streaming regime is found in flow focusing for outer Capillary numbers much smaller than those leading to the dripping-to-jetting transition in an equivalent coflowing configuration [501, 502]. The viscous stresses in the focusing region scale as D_o^{-2} . As a consequence, the droplet formation is considerably affected by the orifice diameter, while it is practically insensitive to the orifice length [502].

According to Dong et al. [440], the use of the “opposed flow focusing” configuration may lead to a continuous reduction of the jet radius down to vanishing scales in what they termed as *second-order jetting transition*. This kind of transition was experimentally observed by Gañán-Calvo et al. [31] using an axisymmetric liquid-liquid-gas coaxial flow focusing configuration. As explained in Sec. 4, the existence of such a vanishing jetting condition was theoretically demonstrated for parallel flows from the analysis of the convective-to-absolute instability transition [31, 182]. Zhang [349]

was the first to demonstrate theoretically the existence of the second order transition in the case of a non-parallel flow (tip streaming), but without interrogating the found solution about its stability. The experimental evidence provided by Dong et al. [440] provides definitive support for this topological transition.

The theoretical analysis of the axisymmetric liquid-liquid flow focusing configuration has received little attention. Gañán-Calvo and Riesco-Chueca [184] studied both theoretically and experimentally the jetting-to-dripping transition taking place at the minimum flow rate stability limit. They compared the experimental minimum flow rates with those leading to the convective-to-absolute instability transition. As mentioned in Sec. 3.1, this comparison is pertinent only if the instability origin is located in the jet. The experimental stability limit in the (Re_j, We_j) plane exhibited an “elbow” for Weber numbers around unity. This elbow has probably to be explained in terms of the global stability analysis of the problem or the superposition at short times of asymptotically stable global modes. Recent results [164] indicate the existence of parameter islands in the (Q_r, μ) plane within which the base flow is globally stable. These islands are delimited by oscillatory/non-oscillatory and convective/absolute instabilities, and their location depends on the geometry and the rest of the governing parameters.

The stability of the axisymmetric liquid-liquid flow focusing configuration has been recently studied by Mu et al. [503] both experimentally and theoretically. They distinguish between the instability originated in the tapering meniscus and that localized in the emitted jet, as previously proposed for the gaseous configuration [185, 348]. In this way, they have successfully explained their experimental observations and direct numerical simulations.

Numerical solutions of the FENE-CR model show that viscoelasticity delays the dripping-to-jetting transition [504], which coincides with the prediction from the local stability analysis prediction for relaxed coflowing Oldroyd-B jets (Sec. 4) [156]. Moyle et al. [505] have proposed a model to predict the appearance of tip streaming in presence of soluble surfactant. Essentially, tip streaming occurs when the mass of surfactant adsorbed to the interface is that needed to maintain the interfacial conical shape. Wrobel et al. [506] have modeled the outer velocity field arising in an axisymmetric flow focusing configuration by combining an imposed uniaxial extension flow at infinity with two transverse, coaxial, annular baffles placed symmetrically to either side of the drop. They have described how a soluble surfactant and the focusing effect produced by the baf-

fles collaborate to produce tip streaming.

13.2. Gaseous flow focusing

13.2.1. Jet shape and size

When focusing a liquid meniscus with a high-speed gaseous current, the major source of energy generally comes from the pressure drop ΔP induced by that current. If one neglects the interfacial and viscous sinks of energy, the jet's radius is given by Eq. (62) [18]. The above result can be refined by considering the viscous stresses exerted by the outer stream, and the loss of kinetic energy due to the resistance offered by the liquid viscosity. Gañán-Calvo et al. [140] found that, when the experimental results are expressed in terms of conveniently scaled jet velocity and streamwise direction coordinate z , they approximately match the universal solution (71) of the 1D momentum equation for a constant driving force [470] (Fig. 64). This solution can be approximated by the simple expression [140]

$$v = \left[\frac{1}{(2x)^{1/2}} + \frac{2}{x^2} \right]^{-1}, \quad (83)$$

where

$$v = 2 \left(\frac{6\sqrt{2}R_\mu}{D_o} \right)^{-1/3} \left(\frac{R_{FF}}{R_j} \right)^2, \quad x = 2 \left(\frac{6\sqrt{2}R_\mu}{D_o} \right)^{-2/3} \frac{z}{D_o}, \quad (84)$$

are the scaled velocity and section coordinate, respectively, and $R_\mu = [\mu_i^2/(\rho_i\Delta P)]^{1/2}$. For $R_\mu \ll 1$ ($x \gg 1$) and $z = D_o$, Eq. (62) is recovered. For $R_\mu \gg 1$ ($x \ll 1$) and $z \sim D_o \sim H$, the viscous scaling law [507]

$$R_j \sim \left(\frac{\mu_i Q_i}{\Delta P H} \right)^{1/2} \quad (85)$$

is obtained.

13.2.2. Breakup length and whipping

The jet breakup length l_b is of great importance in applications such as Serial Femtosecond Crystallography [58]. Very recently [143], a scaling law for l_b in gaseous flow focusing has been derived from the analysis of the energy balance taking place in the jet breakup region. The essential idea is that the breakup length is determined by the transient growth of perturbations coming from the surface energy excess at breakup [144, 508, 509]. Based on this idea, Gañán-Calvo et al. [143] proposed the scaling law

$$l_b/d_\sigma = \alpha_p \xi, \quad (86)$$

$$\xi = \text{We}_{FF}^2 \left[\left(\text{We}_{FF} + \alpha_\mu^2 \text{Ca}_{FF}^2 \right)^{1/2} - \alpha_\mu \text{Ca}_{FF} \right]^{-1}, \quad (87)$$

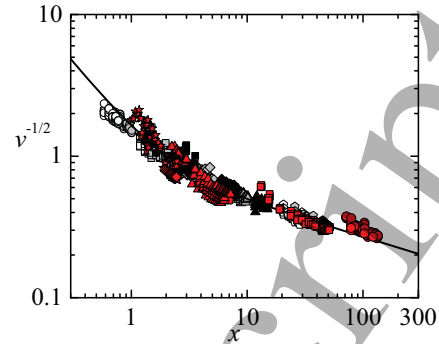


Figure 64: Universal jet shape $v^{-1/2}$ as a function of the scaled axial coordinate x [189]. The symbols correspond to different liquids. The white, grey and black symbols were measured with the plate-orifice configuration [140], while the red ones were obtained by focusing the liquid stream in a glass nozzle [189]. The solid and dashed lines correspond to (71) and (83), respectively (they practically overlap).

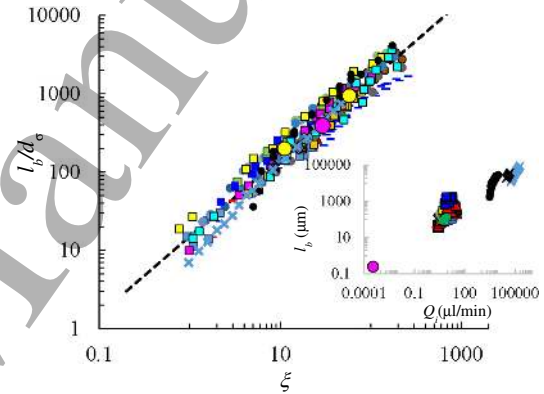


Figure 65: Breakup length l_b for different liquids and nozzles in both flow focused and ballistic jets experiments [143]. The figure shows the experimental data of Umemura [144], additional experiments for water issuing from capillary tubes, and a numerical simulation for this latter configuration.

$\text{We}_{FF} = d_G/d_\sigma$, $d_G = (8\rho_i Q_i^2/(\pi^2 \Delta P))^{1/4}$ and $\text{Ca}_{FF} = (\mu_i^2 \Delta P/(\sigma^2 \rho_i))^{1/2}$. The constants $\alpha_p = 15.015$ and $\alpha_\mu = 0.53$ have been determined experimentally. In their study, they gathered a collection of careful measurements from flow-focused jets [18] and capillary jets directly ejected from orifices (inertial jets). Figure 65 shows the breakup length measured from the nozzle exit for different liquids and nozzles in both flow focused and ballistic jets experiments. Strikingly, the scaling law (86) accurately predicts the breakup length of a nanojet [293] as well.

Direct numerical simulations of liquid microjets in free expanding high-speed co-flowing gas streams provide accurate predictions for both the tip streaming stability conditions and the jet diameter. However, they

overestimate the breakup jet's length [510]. This is probably due to the existence of external perturbations in the experiments.

Experimental studies on the whipping instability in flow-focused jets are still scarce. Acero et al. [189] have distinguished two types of whipping instabilities: that leading to the bending of the emitted jet while keeping the tapering meniscus stable, and that in which both the jet and the meniscus oscillate laterally (absolute whipping). Recent results [164] show the importance of the focusing geometry in the appearance of absolute whipping, and that this kind of instability is linked to the growth of the dominant $m = 1$ global mode.

13.2.3. Minimum flow rate

The stability of a liquid stream focused by a high-speed gas current has been studied both theoretically [30, 347, 511–513] and experimentally [185, 348]. For a fixed applied pressure drop ΔP , jetting becomes unstable when the injected flow rate Q_i falls below a critical value Q_{\min} . For small pressure drops, the instability is originated in the jet and has been described in terms of the convective-to-absolute instability transition (Fig. 14) [30, 182]. If ΔP takes sufficiently large values, the instability is associated with the flow in the tapering meniscus. In this case, the minimum flow rate Q_{\min} for sufficiently small and large Reynolds numbers scales as

$$Q_{\min} \sim Q_v \equiv \frac{R_i^2 \sigma}{\mu_i} \quad \text{and} \quad Q_{\min} \sim Q_D \equiv \frac{D_o \mu_i}{\rho_i}, \quad (88)$$

respectively (Fig. 66). In the former case, the stability limit was explained in terms of the axial component of the surface tension force [348], while the latter was linked to the growth of the recirculation cell inside the liquid meniscus [347].

Vega et al. [185] measured the minimum flow rates for low-viscosity liquids as a function of the capillary-to-orifice distance H in the original plate-orifice configuration. The minimum attainable flow rate Q_{opt} and the corresponding capillary-to-orifice distance H_{opt} obeyed the scaling laws:

$$Q_{\text{opt}}/Q_D \simeq 2.5(2R_i/D_o)^{1/3}, \quad H_{\text{opt}}/D_o \simeq 0.6(2R_i/D_o)^{1/4}. \quad (89)$$

These results are consistent with the numerical simulations conducted by Zahoor et al. [513].

As mentioned in Sec. 4, Cruz-Mazo et al. [56] found good agreement between the experimental minimum flow rates and those calculated from the asymptotic global stability for large applied pressure drops. As occurs in the liquid-liquid configuration, the projection of

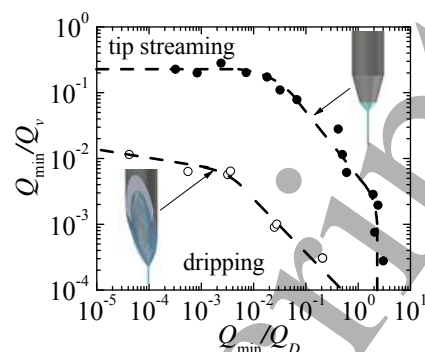


Figure 66: Minimum flow rate Q_{\min} in gaseous flow focusing [40]. The solid symbols are the results obtained when the liquid stream tapers from a capillary located in front of a plate orifice [348] or inside a glass nozzle [189]. The open symbols are the results obtained when the liquid is injected through a hypodermic needle inside a glass nozzle [40]. The dashed lines are to guide the eye.

the experimental stability limit onto the (Re_j, We_j) plane shows an “elbow” for Weber numbers around unity. This elbow can be explained neither in terms of the convective-to-absolute instability transition nor by the growth of the dominant global eigenmode. In this region of the parameter plane, instability is caused by the superposition of asymptotically stable global modes at short times [56] (Fig. 11). This superposition makes the jet break up without perturbing the tapering liquid meniscus, which indicates that somehow the instability is originated in the jet. Interestingly, this result coincides with the prediction obtained from the convective-to-absolute instability analysis [30, 185], which shows that the jet becomes absolutely unstable for Weber numbers around unity.

The minimum flow rates can be greatly reduced if the liquid meniscus is replaced with a film sliding over the tip of a hypodermic needle [40]. Figure 66 shows the minimum flow rates obtained when the liquid stream tapers from a capillary located either in front of a plate orifice or inside a nozzle, and when the liquid is injected through a hypodermic needle. A similar liquid injection system has been recently used by Muhlig et al. [514] to produce nanometre-sized droplets (comparable to those obtained by electrospray ionization) from a new operational regime for gaseous flow focusing.

13.3. Gaseous stream focused by a liquid current

Microbubbles were produced in an axisymmetric flow focusing device from the breakage of an air filament driven by a stream of ethanol-water [149] and glycerol-water [515]. Vega et al. [442] examined the production of microbubbles in the tip streaming

regime for moderate Reynolds numbers. A gaseous thread ejected from the meniscus tip broke up into a quasi-monodisperse collection of bubbles with diameters smaller than that of the discharge orifice. Those diameters are given by the formula

$$\frac{d_b}{D_o} = 1.77 Q_r^{-\beta}, \quad (90)$$

where β takes a value between 0.4 and 0.5 depending on the Reynolds number. Equation (90) with $\beta = 0.5$ can be regarded as the version for this fluid configuration of the classical flow-focusing formula [18]. It can be readily derived under two conditions: (i) neglecting both the energy dissipation in the gas meniscus and the gas kinetic energy at the feeding capillary end, and (ii) assuming that both the pinching location and the proportion between the precursor jet and resulting bubble diameters do not significantly depend on Q_r [442].

The experimental validation of Eq. (90) is shown in Fig. 51, where results for bubbling and jetting are mixed. In fact, it is difficult to determine whether a certain realization of this kind of experiment must be regarded as bubbling or jetting due to the short length of the precursor gaseous threads.

14. Prospectives and futures

The variety and complexity of phenomena associated with the presence of capillary, viscous, inertia and electric forces, bulk and interfacial rheology or certain geometrical conditions offer a multiverse for research, where just a few of its universes have been explored. The insights are impelled by either demanding applications or sheer curiosity and esthetic appeal. However, if one tries to find one overarching reason justifying the strong interest that this field stirs up, the common driver would very probably be our deep need to understand and control a wealth of phenomena normally appearing at the same scales as those of living matter, where not only liquids, soft matter and interfaces prevail, but also where all our experiences and needs originate. We conclude this review by enumerating a few lines where future research would be well justified.

14.1. Transient ejections

Owing to their elusive character, one of the areas with higher potential for newer developments is for sure the transient ejections due to the collapse, with stronger or weaker momentum, of axisymmetric converging radial flow patterns in the presence of a free surface (Fig. 67).

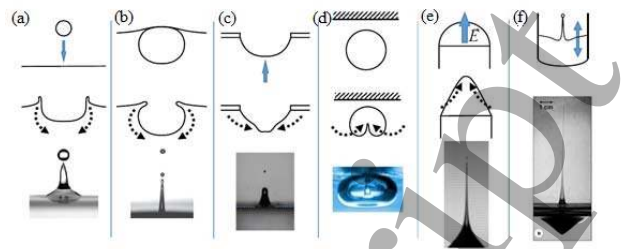


Figure 67: Examples of transient and fast ejections following the release of potential energy associated with the presence of an axisymmetric liquid free surface. The images show the collapse of a cavity produced after a droplet impact on a deep liquid pool (a), after bubble bursting on a free surface (b) and the hole on a plate (c), the bubble collapse by surrounding liquid volume oscillations close to a solid surface (d), the conical collapse of a suddenly electrified liquid droplet (e), and the collapse due to over-driven Faraday waves or the sudden vertical acceleration of a semi-enclosed cylindrical liquid volume (f).

Paradigmatic examples that can be included in this category are the ejections after (i) surface bubble bursting [368, 516–519], (ii) surface acceleration [6, 366, 520], (iii) cavity collapse [521, 522], and (iv) conical collapse of a suddenly electrified liquid droplet [92]. Although the collapsing angle of the converging flow may differ in these examples, the radial component of the liquid velocity causes a rapid change of the flow around a stagnation point located in the vicinity of the free surface. A fundamental question about this phenomenon is whether a spatiotemporal singularity is hidden somewhere in the parameter space governing the flow. In the case of bubble bursting, the existence of that singularity is relatively well established through the demonstrated existence of self-similar solutions [523], although the value of the governing parameter (the Ohnesorge number in this case) for which the singularity appears is still a matter of debate [368, 518, 524–526].

Gañán-Calvo [368] has postulated that the balance between a precise fraction of the driving energy and viscous dissipation should lead to the above-mentioned singularity. Interestingly, when this balance is not perfect, either by excess or defect of one of the factors, the flow may still show time intervals where self-similar solutions can be experimentally observed [523]. One may then postulate that each of the different above-mentioned flow classes, and probably many others leading to rapid transient ejections, would stem from a single class of singularity around which, closer or farther away in the parametrical sense, different flow realizations take place driven by different energy sources, geometries and initial conditions.

Inertia, viscous and surface tension forces compete in the presence of a liquid free surface during transient

ejections. In contrast to what most researchers currently believe based on their experience, there might be a perfect balance only between inertia and viscosity asymptotically close to the spatiotemporal singularity (surface tension becomes negligible). This hypothesis is based on the sheer consistency of the time power law that each term exhibits when a self-similar solution is sought for. This was neatly demonstrated by Eggers [131] in his pioneering work on the axisymmetric free surface pinch-off driven by capillarity. This problem differs from free surface collapse in three aspects: (i) the singularity comes up independently of the values of the parameters involved, (ii) the surface tension force is retained in the asymptotic regime because the free surface radius vanishes at the singularity, and (iii) the existence of an outer medium [308, 309] and bulk or interfacial rheology [71, 123, 292, 320, 527] prevents the system from reaching that regime.

Demonstrating the very existence of a time singularity in the parameter space for a given system and flow configuration would be extremely useful in the search for thinner and faster jets emissions for increasingly demanding applications in industry and research [396, 415, 528].

14.2. Natural breakup of capillary jets

Despite being a classic problem, the determination of the average natural breakup length of a capillary jet has resisted the insight of researchers. Experience teaches us that while global stability analysis predicts breakup lengths much above those experimentally observed, the initial value problem (IVP) analysis yields results strongly dependent on the location and amplitude of the initial perturbation. Thus, the only available tools to tackle this problem are experimental analysis and direct numerical simulation, both supported by dimensional analysis. However, and without a solid physical explanation of the results, the problem will remain open.

As mentioned in Sec. 13, Umemura [144] proposed a plausible physical picture of the above-mentioned problem when the breakup is dominated by capillarity and the jet issues from a circular orifice. The phenomenon is described in terms of Plateau-Rayleigh unstable waves emanating from the orifice, and a self-destabilizing loop associated with them. This could explain the collapse of data for capillary jets as a function of the Weber number. Gañán-Calvo et al. [143] have recently shown that the natural breakup of those jets and those produced by gaseous flow focusing can be predicted by the single physical model (86), which involves the Weber and Capillary numbers and two universal fitting parameters.

Given that encouraging generality, it is an open problem for future research whether the same boldly simple explanation is extendable to other configurations, such as gravitational jets. It is also of interest to determine the potential role of bulk and interfacial rheology in this phenomenon. In particular, the increasing extensional viscosity of weakly viscoelastic liquids may dramatically affect both the rate at which unstable waves are damped upstream and the global energy balances along the jet, which determines the natural breakup length. In some cases, the experimentally observed development of long-term cyclical periods [320, 527] could be predicted theoretically.

14.3. Steady tip streaming stability

As explained in Sec. 3.2, an accurate stability analysis of the steady tip streaming regime generally requires the calculation of the eigenvalues characterizing the linear global modes of the system [158], which constitutes a complex problem for a multiphase capillary system. In addition, global stability may fail to explain certain bifurcations of stability limits [165]. In this case, direct numerical simulations may be the only route to describe the problem theoretically. This scenario explains why the stability analysis of the steady jetting arising from tip streaming has been frequently carried out by splitting the fluid domain into the source and the emitted jet. This steady jetting is assumed to be stable if none of the mechanisms that destabilize each region separately comes into play. The source stability is commonly examined by rationalizing experimental results in terms of simple scaling laws, while the jet behavior is described in terms of the convective-to-absolute instability (Sec. 4).

Global stability of simple-jet tip streaming configurations [56, 109, 139, 163] has been systematically studied only until the recent development of numerical tools for this task [286]. Current developments in simulation methods for flows in the presence of free surfaces promise a wealth of possibilities for applied research. The experimental stability limits of gaseous flow focusing have been rationalized in terms of three instability mechanisms: the jet absolute instability, the growth of the dominant global mode, and the superposition at short times of asymptotically stable global modes [56]. The competition and relationship among these mechanisms should be elucidated for other tip streaming configurations, such as liquid-liquid flow focusing or electrospinning.

14.4. Coaxial capillary jets

Coaxial jets can be driven by coflowing gas streams [18], electric fields [25], pressure gradients [180], etc. The number of parameters governing these flows considerably increases, which makes their systematic study a difficult task. The formation of coaxial jets involves the stability of the upstream flow from which they issue, which usually takes place in a compound capillary meniscus. The breakup of these jets is also strongly affected by the stability of the upstream flow, since the inner jet may break up and drip before the outer jet reaches its own breakup region. Again, the complexity associated with competing effects of different forces appearing in the inner and outer jets, together with the usual presence of bulk and interfacial rheology, keeps this field full of untrodden regions. Therefore, one may consider this area of study in its infancy.

14.5. Surfactant-driven tip streaming in microfluidics

The mechanisms triggered by the presence of surfactants in tip streaming have not been well elucidated yet. It is believed that the major effect is the reduction of the surface tension due to the accumulation of surfactant molecules in the tapering droplet/meniscus tip (the so-called soluto-capillarity effect). However, many questions have not been addressed so far. Do convection and interface expansion empty the tip of the tapering droplet/meniscus? Do Marangoni stress and surface viscosity play a relevant role in the process?

The theoretical analysis of tip streaming in the presence of soluble surfactants is a complicated problem. As happens in the absence of these molecules, there are numerical difficulties associated with the disparity between the time and spatial scales characterizing the flow in the tip and the rest of the fluid domain. In addition, the analysis requires not only solving the convective-diffusive transport of the surfactant across the bulks but also calculating the surfactant distribution over the interface, which involves modeling accurately the adsorption-desorption process. In many cases, the parameters necessary to feed the model are unknown. The analysis may be simplified in some particular cases. If diffusion over the interface ensures a quasi-uniform surfactant distribution, Marangoni stress can be neglected. If the adsorption-desorption characteristic time is much larger than the hydrodynamic time characterizing the tip streaming, the surfactant can be regarded as insoluble during the fluid ejection, and neither the surfactant transport across the bulk nor the adsorption/desorption process needs to be taken into account.

14.6. Other worth noting geometrical and driving effects in jetting

A fertile ground for nonlinear phenomena and unexpected results appears when additional effects are introduced in capillary jetting. Some of those effects have been already considered in the literature. Some possible research lines are listed below. In all of them, bulk and interfacial rheology will enhance the complexity and interest of further studies.

- *Vibration and pulsation.* A wide variety of phenomena have been described depending on the relative weight of the energy introduced by vibration and pulsation compared to inertia, viscous and capillary forces. The influence of the ratio of vibration period over capillary time has also been examined [529, 530]. The extreme cases in which the above-mentioned parameters take values of the order unity or larger still offer an ample field for research.
- *Rotation.* The effect of rotation on the jet dynamics was reviewed by Eggers and Villermaux [62]. Several works have described how non-axisymmetric instabilities with increasing azimuthal wavenumber may prevail for a single-phase liquid jet as the rotation factor is increased. One may consider rotated coaxial jets to favor specific features in microencapsulation. For this purpose, rotation can be combined with, for example, vibration or pulsation.
- *Non-round discharge sections.* This is also a classical effect [531] which can produce potentially unexpected results in combination with other factors.
- *Impinging free jets.* This configuration has attracted the attention of some researchers for its intrinsic esthetic features [532]. It has recently raised the interest of the Serial Femtosecond Crystallography community due to the extremely thin liquid sheets that can be produced [533].

Partial support from the Ministerio de Economía y Competitividad through Grant No. DPI2016-78887 and Junta de Extremadura (Spain) through Grant No. GR18175 is gratefully acknowledged.

References

- [1] S. Xu, Z. Nie, M. Seo, P. Lewis, E. Kumacheva, H. A. Stone, P. Garstecki, D. B. Weibel, I. Gitlin, and G. M. Whitesides.

- Generation of monodisperse particles by using microfluidics: Control over size, shape, and composition. *Angew. Chem.*, 117: 734–738, 2005.
- [2] N. Bhardwaj and S. C. Kundu. Electrospinning: A fascinating fiber fabrication technique. *Biotechnol. Adv.*, 28:325–347, 2010.
 - [3] J. K. Nunes, S. S. H. Tsai, J. Wan, and H. A. Stone. Dripping and jetting in microfluidic multiphase flows applied to particle and fiber synthesis. *J. Phys. D Appl. Phys.*, 46:114002, 2013.
 - [4] J. Rosell-Llompart and A. M. Gañán-Calvo. Turbulence in pneumatic flow focusing and flow blurring regimes. *Phys. Rev. E*, 77:036321, 2008.
 - [5] A. M. Gañán-Calvo, J. M. Montanero, L. Martín-Banderas, and M. Flores-Mosquera. Building functional materials for health care and pharmacy from microfluidic principles and Flow Focusing. *Adv. Drug Delivery Rev.*, 65:1447–1469, 2013.
 - [6] O. A. Basaran. Small-scale free surface flows with breakup: Drop formation and emerging applications. *AIChE J.*, 48: 1842–1848, 2002.
 - [7] H. Wijshoff. The dynamics of the piezo inkjet printhead operation. *Phys. Rep.*, 491:77–177, 2010.
 - [8] N. J. Nielsen. History of the inkjet printhead development. *Hewlett-Packard J.*, 36:4–10, 1985.
 - [9] J. E. Fromm. Numerical calculation of the fluid dynamics of drop-on-demand jets. *IBM J. Res. Dev.*, 28:322–333, 1984.
 - [10] A. U. Chen and O. A. Basaran. A new method for significantly reducing drop radius without reducing nozzle radius in drop-on-demand drop production. *Phys. Fluids*, 14:L1–L4, 2002.
 - [11] T. Boland, T. Xu, B. Damon, and X. Cui. Application of inkjet printing to tissue engineering. *Biotechnol. J.*, 1:910.917, 2006.
 - [12] G. F. Christopher and S. L. Anna. Microfluidic methods for generating continuous droplet streams. *J. Phys. D: Appl. Phys.*, 40:R319–R336, 2007.
 - [13] B. Ambravaneswaran, H. J. Subramani, S. D. Phillips, and O. A. Basaran. Dripping-jetting transitions in a dripping faucet. *Phys. Rev. Lett.*, 93:034501, 2004.
 - [14] G. Taylor. Disintegration of water drops in electric field. *Proc. R. Soc. Lond. A*, 280:383–397, 1964.
 - [15] J. Zeleny. The electrical discharge from liquid points, and a hydrostatic method of measuring the electric intensity at their surfaces. *Phys. Rev.*, 3:69–91, 1914.
 - [16] R. Suryo and O. A. Basaran. Tip streaming from a liquid drop forming from a tube in a co-flowing outer fluid. *Phys. Fluids*, 18:082102, 2006.
 - [17] J. B. Knight, A. Vishwanath, J. P. Brody, and R. H. Austin. Hydrodynamic focusing on a silicon chip: Mixing nanoliters in microseconds. *Phys. Rev. Lett.*, 80:3863–3866, 1998.
 - [18] A. M. Gañán-Calvo. Generation of steady liquid microthreads and micron-sized monodisperse sprays in gas streams. *Phys. Rev. Lett.*, 80:285–288, 1998.
 - [19] S. L. Anna, N. Bontoux, and H. A. Stone. Formation of dispersions using flow focusing in microchannels. *Appl. Phys. Lett.*, 82:364–366, 2003.
 - [20] J. R. Melcher and G. I. Taylor. Electrohydrodynamics: a review of the role of interfacial shear stresses. *Annu. Rev. Fluid Mech.*, 1:111–146, 1969.
 - [21] A. S. Utada, E. Lorenceau, D. R. Link, P. D. Kaplan, H. A. Stone, and D. A. Weitz. Monodisperse double emulsions generated from a microcapillary device. *Science*, 308:537–541, 2005.
 - [22] A. M. Gañán-Calvo and J. M. Gordillo. Perfectly monodisperse microbubbling by capillary flow focusing. *Phys. Rev. Lett.*, 87:274501, 2001.
 - [23] A. M. Gañán-Calvo. Perfectly monodisperse microbubbling by capillary flow focusing: An alternate physical description and universal scaling. *Phys. Rev. E*, 69:027301, 2004.
 - [24] F. Cruz-Mazo, J. M. Montanero, and A. M. Gañán-Calvo. Monosized dripping mode of axisymmetric flow focusing. *Phys. Rev. E*, 94:053122, 2016.
 - [25] I. G. Loscertales, A. Barrero, I. Guerrero, R. Cortijo, M. Marquez, and A. M. Gañán-Calvo. Micro/nano encapsulation via electrified coaxial liquid jets. *Science*, 295:1695–1698, 2002.
 - [26] R. T. Collins, J. J. Jones, M. T. Harris, and O. A. Basaran. Electrohydrodynamic tip streaming and emission of charged drops from liquid cones. *Nature Phys.*, 4:149–154, 2008.
 - [27] R. D. Schroll, R. Wunenburger, A. Casner, W. W. Zhang, and J.-P. Delville. Liquid transport due to light scattering. *Phys. Rev. Lett.*, 98:133601, 2007.
 - [28] J. Eggers. Nonlinear dynamics and breakup of free-surface flows. *Rev. Mod. Phys.*, 69:865–929, 1997.
 - [29] I. Cohen, H. Li, J. L. Houglund, M. Mrksich, and S. R. Nagel. Using selective withdrawal to coat microparticles. *Science*, 292:265–267, 2001.
 - [30] T. Si, F. Li, X.-Y. Yin, and X.-Z. Yin. Modes in flow focusing and instability of coaxial liquid-gas jets. *J. Fluid Mech.*, 629: 1–23, 2009.
 - [31] A. M. Gañán-Calvo, R. González-Prieto, P. Riesco-Chueca, M. A. Herrada, and M. Flores-Mosquera. Focusing capillary jets close to the continuum limit. *Nature Phys.*, 3:737–742, 2007.
 - [32] E. Castro-Hernández, V. Gundabala, A. Fernández-Nieves, and J. M. Gordillo. Scaling the drop size in coflow experiments. *New J. Phys.*, 11:075021, 2009.
 - [33] A. M. Gañán-Calvo and J. M. Montanero. Revision of capillary cone-jet physics: Electro spray and flow focusing. *Phys. Rev. E*, 79:066305, 2009.
 - [34] R. A. De Bruijn. Tipstreaming of drops in simple shear flows. *Chem. Eng. Sci.*, 48:277–284, 1993.
 - [35] C. D. Eggleton, T.-M. Tsai, and K. J. Stebe. Tip streaming from a drop in the presence of surfactants. *Phys. Rev. Lett.*, 87: 048302, 2001.
 - [36] S. L. Anna. Droplets and bubbles in microfluidic devices. *Annu. Rev. Fluid Mech.*, 48:285–309, 2016.
 - [37] P. Lozano and M. Martínez-Sánchez. On the dynamic response of externally wetted ionic liquid ion sources. *J. Phys. D: Appl. Phys.*, 38:2371–2377, 2005.
 - [38] C. M. Whitehouse, R. N. Dreyer, M. Yamashita, and J. B. Fenn. Electrospray interface for liquid chromatographs and mass spectrometers. *Anal. Chem.*, 57:675–679, 1985.
 - [39] A. K. Sen, J. Darabi, D. R. Knapp, and J. Liu. Modeling and characterization of a carbon fiber emitter for electrospray ionization. *J. Micromech. Microeng.*, 16:620–630, 2006.
 - [40] A. J. Acero, N. Rebollo-Muñoz, J. M. Montanero, A. M. Gañán-Calvo, and E. J. Vega. A new flow focusing technique to produce very thin jets. *J. Micromech. Microeng.*, 23:065009, 2013.
 - [41] D. C. Duffy, J. C. McDonald, O. J. A. Schueller, and G. M. Whitesides. Rapid prototyping of microfluidic systems in poly(dimethylsiloxane). *Anal. Chem.*, 70:4974–4984, 1998.
 - [42] M. A. Unger, H. P. Chou, T. Thorsen, A. Scherer, and S. R. Quake. Monolithic microfabricated valves and pumps by multilayer soft lithography. *Science*, 288:113–116, 2000.
 - [43] S. Takeuchi, P. Garstecki, D. B. Weibel, and G. M. Whitesides. An axisymmetric flow-focusing microfluidic device. *Adv. Mater.*, 17:1067–1072, 2005.
 - [44] H. A. Stone, A. D. Stroock, and A. Ajdari. Engineering flows in small devices: Microfluidics toward a lab-on-a-chip. *Annu. Rev. Fluid Mech.*, 36:381–411, 2004.
 - [45] V. Cristini and Y.-C. Tan. Theory and numerical simulation of droplet dynamics in complex flows—a review. *Lab Chip*, 4:

- 257–264, 2004.
- [46] G. M. Whitesides. The origins and the future of microfluidics. *Nature*, 442:368–373, 2006.
- [47] A. Barrero and I. G. Loscertales. Micro and nanoparticles via capillary flows. *Annu. Rev. Fluid Mech.*, 39:89–106, 2007.
- [48] H. Gu, M. H. G. Duits, and F. Mugele. Droplets formation and merging in two-phase flow microfluidics. *Int. J. Mol. Sci.*, 12: 2572–2597, 2011.
- [49] G. T. Vladisavljevic, I. Kobayashi, and M. Nakajima. Production of uniform droplets using membrane, microchannel and microfluidic emulsification devices. *Microfluid. Nanofluid.*, 13: 151–178, 2012.
- [50] P. Zhuab and L. Wang. Passive and active droplet generation with microfluidics: a review. *Lab Chip*, 17:34–75, 2017.
- [51] J. E. Oliveira, E. A. Moraes, R. G. F. Costa, A. S. Afonso, L. H. C. Mattoso, W. J. Orts, and E. S. Medeiros. Nano and submicrometric fibers of poly(d,l-lactide) obtained by solution blow spinning: Process and solution variables. *J. Appl. Polym. Sci.*, 122:3396–3405, 2011.
- [52] B. Wang, Y. Yao, J. Peng, Y. Lin, W. Liu, Y. Luo, R. Xiang, R. Li, and D. Wu. Preparation of poly(ester imide) ultrafine fibers by gas-jet/electrospinning. *J. Appl. Polym. Sci.*, 114: 883–891, 2009.
- [53] J. Rodríguez-Rodríguez, A. Sevilla, C. Martínez-Bazán, and J. M. Gordillo. Generation of microbubbles with applications to industry and medicine. *Annu. Rev. Fluid Mech.*, 47:405–429, 2015.
- [54] A. M. Gañán-Calvo. Electro-flow focusing: The high-conductivity low-viscosity limit. *Phys. Rev. Lett.*, 98:134503, 2007.
- [55] J. Jiang, X. Wang, W. Li, J. Liu, Y. Liu, and G. Zheng. Electrohydrodynamic direct-writing micropatterns with assisted air-flow. *Micromachines*, 9:456, 2018.
- [56] F. Cruz-Mazo, M. A. Herrada, A. M. Gañán-Calvo, and J. M. Montanero. Global stability of axisymmetric flow focusing. *J. Fluid Mech.*, 832:329–344, 2017.
- [57] J. L. Daristotle, A. M. Behrens, A. D. Sandler, and P. Kofinas. A review of the fundamental principles and applications of solution blow spinning. *ACS Appl. Mater. Interfaces*, 8:34951–34963, 2016.
- [58] H. N. Chapman *et al.* Femtosecond X-ray protein nanocrystallography. *Nature*, 470:73–79, 2011.
- [59] D. F. James. Boger fluids. *Annu. Rev. Fluid Mech.*, 41:129–142, 2009.
- [60] C. Clasen, J. P. Plog, W.-M. Kulicke, M. Owens, C. Macosko, L. E. Scriven, M. Verani, and G. H. McKinley. How dilute are dilute solutions in extensional flows? *J. Rheol.*, 50:849–881, 2006.
- [61] J. G. Oldroyd. On the formulation of rheological equations of state. *Proc. Roy. Soc. Lond.*, 200:523–541, 1950.
- [62] J. Eggers and E. Villermaux. Physics of liquid jets. *Rep. Prog. Phys.*, 71:036601, 2008.
- [63] R. B. Bird, R. C. Armstrong, and O. Hassager. *Dynamics of Polymeric Liquids*. John Wiley & Sons, Inc., United States of America, 1987.
- [64] J. H. Snoeijer, A. Pandey, M. A. Herrada, and J. Eggers. The relationship between viscoelasticity and elasticity. submitted, 2019.
- [65] A. V. Bazilevskii, V. M. Entov, and A. N. Rozhkov. Breakup of an Oldroyd liquid bridge as a method for testing the rheological properties of polymer solutions. *Polym. Sci. Ser. A*, 42:716–726, 2001.
- [66] J. J. Feng. The stretching of an electrified non-Newtonian jet: A model for electrospinning. *Phys. Fluids*, 14:3912–3926, 2002.
- [67] C. P. Carroll and Y. L. Joo. Electrospinning of viscoelastic boger fluids: Modeling and experiments. *Phys. Fluids*, 18: 053102, 2006.
- [68] D. Zhou and J. J. Feng. Selective withdrawal of polymer solutions: Computations. *J. Non-Newtonian Fluid Mech.*, 165: 839–851, 2010.
- [69] A. Ponce-Torres, A. J. Acero, M. A. Herrada, and J. M. Montanero. On the validity of the Jeffreys (Oldroyd-B) model to describe the oscillations of a viscoelastic pendant drop. *J. Non-Newtonian Fluid Mech.*, 260:69–75, 2018.
- [70] E. Turkoz, J. M. López-Herrera, J. Eggers, C. B. Arnold, and L. Deike. Axisymmetric simulation of viscoelastic filament thinning with the oldroyd-b model. *J. Fluid Mech.*, 851:R2, 2018.
- [71] C. Clasen, J. Eggers, M. A. Fontelos, J. Li, and G. H. McKinley. The beads-on-string structure of viscoelastic threads. *J. Fluid Mech.*, 556:283–308, 2006.
- [72] J. Doshi and D. R. Reneker. Electrospinning process and applications of electrospun fibers. *J. Electrostat.*, 35:151–60, 1995.
- [73] A. L. Yarin, S. Koombhongse, and D. H. Reneker. Bending instability in electrospinning of nanofibers. *J. Appl. Phys.*, 89: 3018–3026, 2001.
- [74] A. L. Yarin, S. Koombhongse, and D. H. Reneker. Taylor cone and jetting from liquid droplets in electrospinning of nanofibers. *J. Appl. Phys.*, 90:4836–4846, 2001.
- [75] S. A. Theron, E. Zussman, and A. L. Yarin. Experimental investigation of the governing parameters in the electrospinning of polymer solutions. *Polymer*, 45:2017–2030, 2004.
- [76] C. J. Thompson, G. G. Chase, A. L. Yarin, and D. H. Reneker. Effects of parameters on nanofiber diameter determined from electrospinning model. *Polymer*, 48:6913–6922, 2007.
- [77] D. H. Reneker and A. L. Yarin. Electrospinning jets and polymer nanofibers. *Polymer*, 49:2387–2425, 2008.
- [78] T. Han, A. L. Yarin, and D. H. Reneker. Viscoelastic electrospun jets: Initial stresses and elongational rheometry. *Polymer*, 49:1651–1658, 2008.
- [79] A. L. Yarin. Coaxial electrospinning and emulsion electrospinning of core-shell fibers. *Polym. Advan. Technol.*, 22:310–317, 2011.
- [80] A. M. Gañán-Calvo, J. M. López-Herrera, M. A. Herrada, A. Ramos, and J. M. Montanero. Review on the physics of electrospray: from electrokinetics to the operating conditions of single and coaxial Taylor cone-jets, and AC electrospray. *J. Aerosol Sci.*, 125:32–56, 2018.
- [81] R. V. Craster, O. K. Matar, and D. T. Papageorgiou. Breakup of surfactant-laden jets above the critical micelle concentration. *J. Fluid Mech.*, 629:195–219, 2009.
- [82] W. J. Rider and D. B. Kothe. Reconstructing volume tracking. *J. Comput. Phys.*, 141:112–152, 1998.
- [83] J. F. Thompson and Z. U. A. Warsi. Boundary-fitted coordinate systems for numerical solution of partial differential equations—a review. *J. Comput. Phys.*, 47:1–108, 1982.
- [84] N. A. Pelekasis, K. Economou, and J. A. Tsamopoulos. Linear oscillations and stability of a liquid bridge in an axial electric field. *Phys. Fluids*, 13:3564–3581, 2001.
- [85] C. L. Burcham and D. A. Saville. Electrohydrodynamic stability: Taylor-Melcher theory for a liquid bridge suspended in a dielectric gas. *J. Fluid Mech.*, 452:163–187, 2002.
- [86] J. M. Montanero and A. Ponce-Torres. Review on the dynamics of isothermal liquid bridges. *Appl. Mech. Rev.*, 72:010803, 2020.
- [87] L. Y. Yeo, Z. Gagnon, and H.-C. Chang. AC electrospray biomaterials synthesis. *Biomaterials*, 26:6122–6128, 2005.
- [88] N. Chetwani, S. Maheshwari, and H.-C. Chang. Universal cone angle of AC electrosprays due to net charge entrainment. *Phys.*

- Rev. Lett.*, 101:204501, 2008.
- [89] S. Maheshwari and H.-C. Chang. Assembly of multi-stranded nanofiber threads through AC electrospinning. *Adv. Mater.*, 21: 349–354, 2009.
- [90] N. Chetwani, C. Cassou, D. Go, and H.-C. Chang. High-frequency AC electrospray ionization source for mass spectrometry of biomolecules. *J. Am. Soc. Mass Spectrom.*, 21: 1852–1856, 2010.
- [91] A. Gomez and K. Tang. Charge and fission of droplets in electrostatic sprays. *Phys. Fluids*, 6:404–414, 1994.
- [92] A. M. Gañán-Calvo, J. M. López-Herrera, N. Rebollo-Muñoz, and J. M. Montanero. The onset of electrospray: the universal scaling laws of the first ejection. *Sci. Rep.*, 6:32357, 2016.
- [93] A. Jaworek and A. Krupa. Classification of the modes of EHD spraying. *J. Aerosol Sci.*, 30:873–893, 1999.
- [94] A. J. Híjano, I. G. Loscertales, S. E. Ibáñez, and F. J. Higuera. Periodic emission of droplets from an oscillating electrified meniscus of a low-viscosity, highly conductive liquid. *Phys. Rev. E*, 91:013011, 2015.
- [95] J. M. López-Herrera, A. M. Gañán-Calvo, S. Popinet, and M. A. Herrada. Electrokinetic effects in the breakup of electrified jets: A Volume-Of-Fluid numerical study. *Int. J. Multi-phase Flow*, 71:14–21, 2015.
- [96] R. Pillai, J. D. Berry, D. J. E. Harvie, and M. R. Davidson. Electrokinetics of isolated electrified drops. *Soft Matter*, 12: 3310–3325, 2016.
- [97] D. T. Conroy, K. Matar, R. V. Craster, and D. T. Papageorgiou. Breakup of an electrified viscous thread with charged surfactants. *Phys. Fluids*, 23:022103, 2011.
- [98] C. Ferrera, J. M. López-Herrera, M. A. Herrada, J. M. Montanero, and A. J. Acero. Dynamical behavior of electrified pendant drops. *Phys. Fluids*, 25:012104, 2013.
- [99] H. Dastourani, M. R. Jahannama, and A. Eslami-Majd. A physical insight into electrospray process in cone-jet mode: Role of operating parameters. *Int. J. Heat Fluid Flow*, 70:315–335, 2018.
- [100] G. Taylor. Studies in electrohydrodynamics. i. The circulation produced in a drop by electrical field. *Proc. R. Soc. Lond. A*, 291:159–166, 1966.
- [101] D. A. Saville. Electrohydrodynamics: The Taylor-Melcher leaky dielectric model. *Annu. Rev. Fluid Mech.*, 29:27–64, 1997.
- [102] O. Schnitzer and E. Yariv. The Taylor-Melcher leaky dielectric model as a macroscale electrokinetic description. *J. Fluid Mech.*, 773:1–13, 2015.
- [103] P. M. Vlahovska. Electrohydrodynamics of drops and vesicles. *Annu. Rev. Fluid Mech.*, 51:305–330, 2019.
- [104] A. M. Gañán-Calvo. Cone-jet analytical extension of Taylor’s electrostatic solution and the asymptotic universal scaling laws in electrospraying. *Phys. Rev. Lett.*, 79:217–220, 1997.
- [105] A. M. Gañán-Calvo. On the general scaling theory for electrospraying. *J. Fluid Mech.*, 507:203–212, 2004.
- [106] J. Fernández de la Mora. The fluid dynamics of Taylor cones. *Annu. Rev. Fluid Mech.*, 39:217–243, 2007.
- [107] F. J. Higuera. Numerical computation of the domain of operation of an electrospray of a very viscous liquid. *J. Fluid Mech.*, 648:35–52, 2010.
- [108] M. A. Herrada, J. M. López-Herrera, A. M. Gañán-Calvo, E. J. Vega, J. M. Montanero, and S. Popinet. Numerical simulation of electrospray in the cone-jet mode. *Phys. Rev. E*, 86:026305, 2012.
- [109] A. Ponce-Torres, N. Rebollo-Muñoz, M. A. Herrada, A. M. Gañán-Calvo, and J. M. Montanero. The steady cone-jet mode of electrospraying close to the minimum volume stability limit. *J. Fluid Mech.*, 857:142–172, 2018.
- [110] J.-P. Borra. Review on water electro-sprays and applications of charged drops with focus on the corona-assisted cone-jet mode for High Efficiency Air Filtration by wet electro-scrubbing of aerosols. *J. Aerosol Sci.*, 125:208–236, 2018.
- [111] M. Gamero-Castaño and M. Magnani. Numerical simulation of electrospraying in the cone-jet mode. *J. Fluid Mech.*, in press, 2018.
- [112] Z. Jiang, Y. Gan, and Y. Shi. An improved model for prediction of the cone-jet formation in electrospray with the effect of space charge. *J. Aerosol Sci.*, 139:105463, 2020.
- [113] L. Y. Yeo, D. Lastochkin, S.-C. Wang, and H.-C. Chang. A new AC electrospray mechanism by Maxwell-Wagner polarization and capillary resonance. *Phys. Rev. Lett.*, 92:133902, 2004.
- [114] E. Demekhin, S. Polyanskikh, and A. Ramos. Taylor cones in a leaky dielectric liquid under an AC electric field. *Phys. Rev. E*, 84:035301(R), 2011.
- [115] F. J. Higuera. Model of the meniscus of an ionic-liquid ion source. *Phys. Rev. E*, 77:026308, 2008.
- [116] C. S. Coffman, M. Martínez-Sánchez, and P. C. Lozano. Electrohydrodynamics of an ionic liquid meniscus during evaporation of ions in a regime of high electric field. *Phys. Rev. E*, 99: 063108, 2019.
- [117] Y.-M. Tricot. *Surfactants: static and dynamic surface tension*, volume 1 of *Liquid Film Coating*, pages 100–136. Chapman and Hall, 1997.
- [118] F. Jin and K. J. Stebe. The effects of a diffusion controlled surfactant on a viscous drop injected into a viscous medium. *Phys. Fluids*, 19:112103, 2007.
- [119] L. E. Scriven. Dynamics of a fluid interface. Equation of motion for Newtonian surface fluids. *Chem. Eng. Sci.*, 12:98–108, 1960.
- [120] J. M. Lopez and A. Hirska. Direct determination of the dependence of the surface shear and dilatational viscosities on the thermodynamic state of the interface: theoretical foundations. *J. Colloid Interface Sci.*, 206:231–239, 1998.
- [121] Z. Y. Luo, X. L. Shang, and B. F. Bai. Influence of pressure-dependent surface viscosity on dynamics of surfactant-laden drops in shear flow. *J. Fluid Mech.*, 858:91–121, 2019.
- [122] D. Langevin. Rheology of adsorbed surfactant monolayers at fluid surfaces. *Annu. Rev. Fluid Mech.*, 46:4765, 2014.
- [123] A. Ponce-Torres, J. M. Montanero, M. A. Herrada, E. J. Vega, and J. M. Vega. Influence of the surface viscosity on the breakup of a surfactant-laden drop. *Phys. Rev. Lett.*, 118: 024501, 2017.
- [124] S. C. Ozan and H. A. Jakobsen. On the role of the surface rheology in film drainage between fluid particles. *Int. J. Multi-phase Flow*, 120:103103, 2019.
- [125] Z. A. Zell, A. Nowbahar, V. Mansard, L. G. Leal, S. S. Deshmukh, J. M. Mecca, C. J. Tucker, and T. M. Squires. Surface shear inviscidity of soluble surfactants. *Proc. Natl. Acad. Sci.*, 111:3677–3682, 2014.
- [126] D. A. Edwards, H. Brenner, and D. T. Wasan. *Interfacial Transport Processes and Rheology*. Butterworth-Heinemann, 1991.
- [127] E. B. Dussan. On the spreading of liquids on solid surfaces: static and dynamic contact lines. *Ann. Rev. Fluid Mech.*, 11: 371–400, 1979.
- [128] H. P. Greenspan. On the motion of a small viscous droplet that wets a surface. *J. Fluid Mech.*, 84:125–143, 1978.
- [129] M. M. Denn. Continuous drawing of liquids to form fibers. *Annu. Rev. Fluid Mech.*, 12:365–387, 1980.
- [130] G. W. Young and S. H. Davis. Rivulet instabilities. *J. Fluid Mech.*, 176:1–31, 1987.
- [131] J. Eggers. Universal pinching of 3D axisymmetric free-surface flow. *Phys. Rev. Lett.*, 71:3458–3460, 1993.

- [132] A. M. Gañán-Calvo. The surface charge in electrospraying: Its nature and its universal scaling laws. *J. Aerosol Sci.*, 30: 863–872, 1999.
- [133] J. J. Feng. Stretching of a straight electrically charged viscoelastic jet. *J. Non-Newtonian Fluid Mech.*, 116:55–70, 2003.
- [134] H. Wee, B. W. Wagoner, P. M. Kamat, and O. A. Basaran. Effects of surface viscosity on breakup of viscous threads. *Phys. Rev. Lett.*, 124:204501, 2020.
- [135] A. M. Gañán-Calvo. The electrohydrodynamic atomization of liquids today. *J. Aerosol Sci.*, 30:S547–S548, 1999.
- [136] S. Gadkari. Influence of polymer relaxation time on the electrospinning process: Numerical investigation. *Polymers*, 9: 501, 2017.
- [137] T. Hu, Q. Fu, and L. Yang. Falling film with insoluble surfactants: effects of surface elasticity and surface viscosities. *J. Fluid Mech.*, 889:A16, 2020.
- [138] A. Javadi, J. Eggers, D. Bonn, M. Habibi, and N. M. Ribe. Delayed capillary breakup of falling viscous jets. *Phys. Rev. Lett.*, 110:144501, 2013.
- [139] J. M. Gordillo, A. Sevilla, and F. Campo-Cortés. Global stability of stretched jets: conditions for the generation of monodisperse micro-emulsions using coflows. *J. Fluid Mech.*, 738: 335–357, 2014.
- [140] A. M. Gañán-Calvo, C. Ferrera, and J. M. Montanero. Universal size and shape of viscous capillary jets: application to gas-focused microjets. *J. Fluid Mech.*, 670:427–438, 2011.
- [141] G. I. Barenblatt. *Scaling*. Cambridge University Press, Cambridge, UK, 2003.
- [142] A. S. Ismail, J. Yao, H. H. Xia, and J. P. W. Stark. Breakup length of electrified liquid jets: Scaling laws and applications. *Phys. Rev. Appl.*, 10:064010, 2018.
- [143] A. M. Gañán-Calvo, H. N. Chapman, M. Heymann, M. O. Wiedorn, J. Knoska, Y. Du, B. Gañán-Riesco, M. A. Herrada, J. M. López-Herrera, F. Cruz-Mazo, S. Bajt, and J. M. Montanero. The natural breakup length of a steady capillary jet. *arXiv:1908.10841*, 2019.
- [144] A. Umemura. Self-destabilising loop of a low-speed water jet emanating from an orifice in microgravity. *J. Fluid Mech.*, 25: 146–180, 2016.
- [145] J. B. Keller, S. I. Rubinov, and Y. O. Tu. Spatial instability of a jet. *Phys. Fluids*, 16:2052–2055, 1973.
- [146] P. Huerre and P. A. Monkewitz. Local and global instabilities in spatially developing flows. *Annu. Rev. Fluid Mech.*, 22:473–537, 1990.
- [147] S. P. Lin. *Breakup of liquid sheets and jets*. Cambridge University Press, New York, USA, 2003.
- [148] P. Guillot, A. Colin, A. S. Utada, and A. Ajdari. Stability of a jet in confined pressure-driven biphasic flows at low Reynolds numbers. *Phys. Rev. Lett.*, 99:104502, 2007.
- [149] A. M. Gañán-Calvo, M. A. Herrada, and P. Garstecki. Bubbling in unbounded coflowing liquids. *Phys. Rev. Lett.*, 96: 124504, 2006.
- [150] P. A. Yakubenko. Global capillary instability of an inclined jet. *J. Fluid Mech.*, 346:181–200, 1997.
- [151] L. de Luca. Experimental investigation of the global instability of plane sheet flows. *J. Fluid Mech.*, 399:355–376, 1999.
- [152] S. Le Dizes. Global modes in falling capillary jets. *Eur. J. Mech. B/Fluids*, 16:761–778, 1997.
- [153] R. J. Briggs. *Electron-Stream Interaction with Plasmas*. MIT Press, Cambridge, 1964.
- [154] J. M. Montanero and A. M. Gañán-Calvo. Stability of coflowing capillary jets under non-axisymmetric perturbations. *Phys. Rev. E*, 77:046301, 2008.
- [155] W. van Saarloos. Dynamical velocity selection: Marginal stability. *Phys. Rev. Lett.*, 58:2571–2574, 1987.
- [156] J. M. Montanero and A. M. Gañán-Calvo. Viscoelastic effects on the jetting-dripping transition in co-flowing capillary jets. *J. Fluid Mech.*, 610:249–260, 2008.
- [157] J. Chomaz. Global instabilities in spatially developing flows. *Annu. Rev. Fluid Mech.*, 37:357–392, 2005.
- [158] V. Theofilis. Global linear instability. *Annu. Rev. Fluid Mech.*, 43:319–352, 2011.
- [159] U. S. Sauter and H. W. Buggisch. Stability of initially slow viscous jets driven by gravity. *J. Fluid Mech.*, 533:237–257, 2005.
- [160] O. Tammisola, F. Lundell, and L. D. Soderberg. Surface tension-induced global instability of planar jets and wakes. *J. Fluid Mech.*, 713:632–658, 2012.
- [161] M. Rubio-Rubio, A. Sevilla, and J. M. Gordillo. On the thinnest steady threads obtained by gravitational stretching of capillary jets. *J. Fluid Mech.*, 729:471–483, 2013.
- [162] L. Augello, A. Fani, and F. Gallaire. The influence of the entry region on the instability of a coflowing injector device. *J. Phys.: Condens. Matter*, 30:284003, 2018.
- [163] S. Blanco-Trejo, M. A. Herrada, A. M. Gañán-Calvo, and J. M. Montanero. Electrospray cone-jet mode for weakly viscoelastic liquids. *Phys. Rev. E*, 100:043114, 2019.
- [164] S. Blanco-Trejo, M. A. Herrada, A. M. Gañán-Calvo, A. Rubio, M. G. Cabezas, and J. M. Montanero. Whipping in gaseous flow focusing. *Int. J. Multiphase Flow*, 130:103367, 2020.
- [165] P. J. Schmid. Nonmodal stability theory. *Annu. Rev. Fluid Mech.*, 39:129–162, 2007.
- [166] L. de Luca, M. Costa, and C. Caramiello. Energy growth of initial perturbations in two-dimensional gravitational jets. *Phys. Fluids*, 14:289–299, 2002.
- [167] S. J. Leib and M. E. Goldstein. Convective and absolute instability of a viscous liquid jet. *Phys. Fluids*, 29:952–954, 1986.
- [168] K. Chen and H. Richter. Instability analysis of the transition from bubbling to jetting in a gas injected into a liquid. *Int. J. Multiphase Flow*, 23:699–712, 1997.
- [169] E. Castro-Hernández, W. van Hoeve, D. Lohse, and J. M. Gordillo. Microbubble generation in a co-flow device operated in a new regime. *Lab Chip*, 11:2023–2029, 2011.
- [170] R. Xiong, M. Bai, and J. N. Chung. Formation of bubbles in a simple co-flowing micro-channel. *J. Micromech. Microeng.*, 17:1002–1011, 2007.
- [171] M. A. Herrada, A. M. Gañán-Calvo, and J. M. Montanero. Theoretical investigation of a technique to produce microbubbles by a microfluidic T-junction. *Phys. Rev. E*, 88:033027, 2013.
- [172] S. P. Lin and R. D. Reitz. Drop and spray formation from a liquid jet. *Annu. Rev. Fluid Mech.*, 30:85–105, 1998.
- [173] S. P. Lin and Z. W. Lian. Absolute instability of a liquid jet in a gas. *Phys. Fluids A*, 1:490–493, 1989.
- [174] A. M. Gañán-Calvo. Absolute instability of a viscous hollow jet. *Phys. Rev. E*, 75:027301, 2007.
- [175] A. S. Utada, A. Fernandez-Nieves, J. M. Gordillo, and D. A. Weitz. Absolute instability of a liquid jet in a coflowing stream. *Phys. Rev. Lett.*, 100:014502, 2008.
- [176] A. Evangelio, F. Campo-Cortés, and J. M. Gordillo. Simple and double microemulsions via the capillary breakup of highly stretched liquid jets. *J. Fluid Mech.*, 804:550–577, 2016.
- [177] P. Guillot, A. Colin, and A. Ajdari. Stability of a jet in confined pressure-driven biphasic flows at low Reynolds number in various geometries. *Phys. Rev. E*, 78:016307, 2008.
- [178] J. J. Healey. Inviscid axisymmetric absolute instability of swirling jets. *J. Fluid Mech.*, 613:1–33, 2008.
- [179] A. Chauhan, C. Maldarelli, D. T. Papageorgiou, and D. S. Rumschitzki. The absolute instability of an inviscid compound

- jet. *J. Fluid Mech.*, 549:81–98, 2006.
- [180] M. A. Herrada, J. M. Montanero, C. Ferrera, and A. M. Gañán-Calvo. Analysis of the dripping-jetting transition in compound capillary jets. *J. Fluid Mech.*, 649:523–536, 2010.
- [181] A. Alhushaybari and J. Uddin. Convective and absolute instability of viscoelastic liquid jets in the presence of gravity. *Phys. Fluids*, 31:044106, 2019.
- [182] A. M. Gañán-Calvo. Unconditional jetting. *Phys. Rev. E*, 78:026304, 2008.
- [183] N. Rebollo-Muñoz, A. J. Acero, J. Z. Marcos de León, J.M. Montanero, and A.M. Gañán-Calvo. A hybrid flow focusing nozzle design to produce micron and sub-micron capillary jets. *Int. J. Mass Spectrom.*, 403:32–38, 2016.
- [184] A. M. Gañán-Calvo and P. Riesco-Chueca. Jetting-dripping transition of a liquid jet in a lower viscosity co-flowing immiscible liquid: the minimum flow rate in flow focusing. *J. Fluid Mech.*, 553:75–84, 2006.
- [185] E. J. Vega, J. M. Montanero, M. A. Herrada, and A. M. Gañán-Calvo. Global and local instability of flow focusing: The influence of the geometry. *Phys. Fluids*, 22:064105, 2010.
- [186] S. L. Anna and H. C. Mayer. Microscale tipstreaming in a microfluidic flow focusing device. *Phys. Fluids*, 18:121512, 2006.
- [187] A. S. Utada, A. Fernandez-Nieves, H. A. Stone, and D. A. Weitz. Dripping to jetting transitions in coflowing liquid streams. *Phys. Rev. Lett.*, 99:094502, 2007.
- [188] M. A. Herrada, A. M. Gañán-Calvo, and P. Guillot. Spatiotemporal instability of a confined capillary jet. *Phys. Rev. E*, 78:046312, 2008.
- [189] A. J. Acero, C. Ferrera, J. M. Montanero, and A. M. Gañán-Calvo. Focusing liquid microjets with nozzles. *J. Micromech. Microeng.*, 22:065011, 2012.
- [190] M. A. Herrada, C. Ferrera, J. M. Montanero, and A. M. Gañán-Calvo. Absolute lateral instability in capillary coflowing jets. *Phys. Fluids*, 22:064104, 2010.
- [191] F. J. Higuera. Flow rate and electric current emitted by a Taylor cone. *J. Fluid Mech.*, 484:303–327, 2003.
- [192] M. Gamero-Castaño. Energy dissipation in electrosprays and the geometric scaling of the transition region of cone-jets. *J. Fluid Mech.*, 662:493–513, 2010.
- [193] D. Dharmansh and P. Chokshi. Axisymmetric instability in a thinning electrified jet. *Phys. Rev E*, 93:043124, 2016.
- [194] D. Dharmansh and P. Chokshi. Stability analysis of an electrospinning jet of a polymeric fluid. *Polymer*, 131:34–49, 2017.
- [195] F. Cruz-Mazo, M. O. Wiedorn, M. A. Herrada, S. Bajt, H. N. Chapman, and A. M. Gañán-Calvo. Aerodynamically stabilized Taylor cone jets. *Phys. Rev. E*, 100:031101(R), 2019.
- [196] H. A. Stone, B. J. Bentley, and L. G. Leal. An experimental study of transient effects in the breakup of viscous drops. *J. Fluid Mech.*, 173:131–158, 1986.
- [197] L. Rayleigh. On the instability of jets. *Proc. London Math. Soc.*, s1-10:4–13, 1878.
- [198] G. K. Batchelor. *Collected Works of G. I. Taylor*. Cambridge University Press., Cambride, UK, 1958.
- [199] T. Driessen, R. Jeurissen, H. Wijshoff, F. Toschi, and D. Lohse. Stability of viscous long liquid filaments. *Phys. Fluids*, 25:062109, 2012.
- [200] A. A. Castrejón-Pita, J. R. Castrejón-Pita, and I. M. Hutchings. Breakup of liquid filaments. *Phys. Rev. Lett.*, 108:074506, 2012.
- [201] F. Wang, F. P. Conto, N. Naz, J. R. Castrejón-Pita, A. A. Castrejón-Pita, C. G. Bailey, W. Wang, J. J. Feng, and Y. Sui. A fate-alternating transitional regime in contracting liquid filaments. *J. Fluid Mech.*, 860:640–653, 2019.
- [202] C. R. Anthony, P. M. Kamat, M. T. Harris, and O. A. Basaran. Dynamics of contracting filaments. *Phys. Rev. Fluids*, 4:093601, 2019.
- [203] L. Rayleigh. Some applications of photography. *Nature*, 44:249–254, 1891.
- [204] N. Chigier and R. D. Reitz. Regimes of jet breakup and breakup mechanisms (physical aspects). In *Recent Advances in Spray Combustion: Spray Atomization and Drop Burning Phenomena*, pages 109–135, AIAA, Reston, 1996.
- [205] W. van Hoeve, S. Gekle, J. H. Snoeijer, M. Versluis, M. P. Brenner, and D. Lohse. Breakup of diminutive Rayleigh jets. *Phys. Fluids*, 22:122003, 2010.
- [206] B. Ambravaneswaran, S. D. Phillips, and O. A. Basaran. Theoretical analysis of a dripping faucet. *Phys. Rev. Lett.*, 85:034501, 2000.
- [207] A. Kalaaji, B. Lopez, P. Attané, and A. Soucemarianadin. Breakup length of forced liquid jets. *Phys. Fluids*, 15:2469–2479, 2003.
- [208] H. González and F. García. The measurement of growth rates in capillary jets. *J. Fluid Mech.*, 619:179–212, 2009.
- [209] W. T. Pimbley and H. C. Lee. Satellite droplet formation in a liquid jet. *IBM J. Res. Dev.*, 21:21–30, 1977.
- [210] J. W. S. Rayleigh. On the instability of a cylinder of viscous liquid under capillary force. *Phil. Mag.*, 35:145–155, 1892.
- [211] A. M. Gañán-Calvo, M. A. Herrada, and J. M. Montanero. How does a shear boundary layer affect the stability of a capillary jet? *Phys. Fluids*, 26:061701, 2014.
- [212] S. Tomotika. On the instability of a cylindrical thread of a viscous liquid surrounded by another viscous fluid. *Proc. R. Soc. Lond.*, 150:322–337, 1935.
- [213] M.-L. E. Timmermans and J. R. Lister. The effect of surfactant on the stability of a liquid thread. *J. Fluid Mech.*, 459:289–306, 2002.
- [214] S. Goren and M. Gottlieb. Surface-tension-driven breakup of viscoelastic liquid threads. *J. Fluid Mech.*, 120:245–266, 1982.
- [215] G. Taylor. Electrically driven jets. *Proc. Roy. Soc. Lond. A*, 313:453–475, 1969.
- [216] R. P. A. Hartman, D. J. Brunner, D. M. A. Camelot, J. C. M. Marijnissen, and B. Scarlett. Jet break-up in electrohydrodynamic atomization in the cone-jet mode. *J. Aerosol Sci.*, 31:65–95, 2000.
- [217] J. M. López-Herrera, P. Riesco-Chueca, and A. M. Gañán-Calvo. Linear stability analysis of axisymmetric perturbations in imperfectly conducting liquid jets. *Phys. Fluids*, 17:034106, 2005.
- [218] J. M. Gordillo, M. Pérez-Saborid, and A. M. Gañán-Calvo. Linear stability of co-flowing liquid-gas jets. *J. Fluid Mech.*, 448:23–51, 2001.
- [219] R. Seemann, M. Brinkmann, T. Pfohl, and S. Herminghaus. Droplet based microfluidics. *Rep. Prog. Phys.*, 75:016601, 2012.
- [220] T. Cubaud and T. G. Mason. Capillary threads and viscous droplets in square microchannels. *Phys. Fluids*, 20:053302, 2008.
- [221] K. J. Humphry, A. Ajdari, A. Fernández-Nieves, H. A. Stone, and D. A. Weitz. Suppression of instabilities in multiphase flow by geometric confinement. *Phys. Rev. E*, 79:056310, 2009.
- [222] C. E. Hickox. Instability due to density and viscosity stratification in an axisymmetric pipe flow. *Phys. Fluids*, 14:251–262, 1971.
- [223] M. N. Kashid, W. Kowalinski, A. Renken, J. Baldyga, and L. Kiwi-Minsker. Analytical method to predict two-phase flow pattern in horizontal micro-capillaries. *Chem. Eng. Sci.*, 74:219–232, 2012.
- [224] P. J. A. Janssen, H. E. H. Meijer, and P. D. Anderson. Stability and breakup of confined threads. *Phys. Fluids*, 24:012102,

- 2012.
- [225] M. G. Cabezas, M. A. Herrada, and J. M. Montanero. Stability of a jet moving in a rectangular microchannel. *Phys. Rev. E*, 100:053104, 2019.
- [226] A. Sanz and J. Meseguer. One-dimensional linear analysis of the compound jet. *J. Fluid Mech.*, 159:55–68, 1985.
- [227] A. Chauhan, C. Maldarelli, D. T. Papageorgiou, and D. S. Rumschitzk. Temporal instability of compound threads and jets. *J. Fluid Mech.*, 420:1–25, 2000.
- [228] R. Bocanegra, J. L. Sampedro, A. M. Gañán-Calvo, and M. Márquez. Monodisperse structured multi-vesicle microencapsulation using flow-focusing and controlled disturbance. *J. Microencapsulation*, 22:745–759, 2005.
- [229] S. Y. Lee, C. Snider, K. Park, and J. P. Robinson. Compound jet instability in a microchannel for mononuclear compound drop formation. *J. Micromech. Microeng.*, 17:1558, 2007.
- [230] S. Middleman. Stability of a viscoelastic jet. *Chem. Eng. Sci.*, 20:1037–1040, 1965.
- [231] M. Goldin, J. Yerushalmi, R. Pfeffer, and R. Shinnar. Breakup of a laminar capillary jet of a viscoelastic fluid. *J. Fluid Mech.*, 38:689–711, 1969.
- [232] Günter Brenn, Zhengbai Liu, and Franz Durst. Linear analysis of the temporal instability of axisymmetrical non-Newtonian liquid jets. *Int. J. Multiphase Flow*, 26:1621–1644, 2000.
- [233] T. Funada and D. D. Joseph. Viscoelastic potential flow analysis of capillary instability. *J. Non-Newtonian Fluid Mech.*, 111:87–105, 2003.
- [234] H.-Y. Ye, L.-J. Yang, and Q.-F. Fu. Instability of viscoelastic compound jets. *Phys. Fluids*, 28:043101, 2016.
- [235] K. V. Edmond, A. B. Schofield, M. Marquez, J. P. Rothstein, and A. D. Dinsmore. Stable jets of viscoelastic fluids and self-assembled cylindrical capsules by hydrodynamic focusing. *Langmuir*, 22:9052–9056, 2006.
- [236] A. Ponce-Torres, J. M. Montanero, E. J. Vega, and A. M. Gañán-Calvo. The production of viscoelastic capillary jets with gaseous flow focusing. *J. Non-Newtonian Fluid Mech.*, 229:8–15, 2016.
- [237] A. Ponce-Torres, E. J. Vega, A. A. Castrejón-Pita, and J. M. Montanero. Smooth printing of viscoelastic microfilms with a flow focusing ejector. *J. Non-Newtonian Fluid Mech.*, 249:1–7, 2017.
- [238] A. S. Mohamed, M. A. Herrada, A. M. Gañán-Calvo, and J. M. Montanero. Convective-to-absolute instability transition in a viscoelastic capillary jet subject to unrelaxed axial elastic tension. *Phys. Rev. E*, 92:023006, 2015.
- [239] S. J. Gill and J. Gavis. Tensile stress in jets of viscoelastic fluids. I. *J. Polym. Sci.*, 20:287–298, 1956.
- [240] A. L. Huebner and H. N. Chu. Instability and breakup of charged liquid jets. *J. Fluid Mech.*, 49:361–372, 1971.
- [241] D. A. Saville. Electrohydrodynamic stability: Fluid cylinders in longitudinal electric fields. *Phys. Fluids*, 13:2987–2994, 1970.
- [242] D. A. Saville. Stability of electrically charged viscous cylinders. *Phys. Fluids*, 14:1095–1099, 1971.
- [243] F. Li, X.-Y. Yin, and X.-Z. Yin. Linear instability of a coflowing jet under an axial electric field. *Phys. Rev. E*, 74:036304, 2006.
- [244] D. A. Saville. Electrohydrodynamic stability: effects of charge relaxation at the interface of a liquid jet. *J. Fluid Mech.*, 48:815–827, 1971.
- [245] A. J. Mestel. Electrohydrodynamic stability of a slightly viscous jet. *J. Fluid Mech.*, 274:93–113, 1994.
- [246] A. J. Mestel. Electrohydrodynamic stability of a highly viscous jet. *J. Fluid Mech.*, 312:311–326, 1994.
- [247] L. Xie, L. Yang, L. Qin, and Q. Fu. Temporal instability of charged viscoelastic liquid jets under an axial electric field. *Eur. J. Mech./Fluids*, 66:60–70, 2017.
- [248] C. P. Carroll and Y. L. Joo. Axisymmetric instabilities of electrically driven viscoelastic jets. *J. Non-Newtonian Fluid Mech.*, 153:130–148, 2008.
- [249] S. Kwak and C. Pozrikidis. Effect of surfactants on the instability of a liquid thread or annular layer. Part I: Quiescent fluids. *Int. J. Multiphase Flow*, 27:1–37, 2001.
- [250] S. Hansen, G. W. M. Peters, and H. E. H. Meijer. The effect of surfactant on the stability of a fluid filament embedded in a viscous fluid. *J. Fluid Mech.*, 382:331–349, 1999.
- [251] F. Li, A. M. Gañán-Calvo, J. M. López-Herrera, X.-Y. Yin, and X.-Z. Yin. Absolute and convective instability of a charged viscoelastic liquid jet. *J. Non-Newtonian Fluid Mech.*, 196:58–69, 2013.
- [252] E. J. Vega, A. M. Gañán-Calvo, J. M. Montanero, M. G. Cabezas, and M. A. Herrada. A novel technique for producing metallic microjets and microdrops. *Microfluid Nanofluid*, 14:101–111, 2013.
- [253] K. Mu, T. Si, E. Li, R. X. Xu, and H. Ding. Numerical study on droplet generation in axisymmetric flow focusing upon actuation. *Phys. Fluids*, 30:012111, 2018.
- [254] C. Yang, R. Qiao, K. Mu, Z. Zhu, R. X. Xu, and T. Si. Manipulation of jet breakup length and droplet size in axisymmetric flow focusing upon actuation. *Phys. Fluids*, 31:091702, 2019.
- [255] J. Ruiz-Rus, R. Bolaños-Jiménez, A. Sevilla, and C. Martínez-Bazán. Bubble formation regimes in forced co-axial air-water jets. *arXiv:1912.01386*, 2019.
- [256] F. J. García, H. González, F. J. Gómez-Aguilar, A. A. Castrejón-Pita, and J. R. Castrejón-Pita. Evolution of Gaussian wave packets in capillary jets. *Phys. Rev. E*, 100:053111, 2019.
- [257] J. C. Lasheras and E. J. Hopfinger. Liquid jet instability and atomization in a coaxial gas stream. *Annu. Rev. Fluid Mech.*, 32:275–308, 2000.
- [258] J. M. Gordillo and M. Pérez-Saborid. Aerodynamic effects in the break-up of liquid jets: on the first wind-induced break-up regime. *J. Fluid Mech.*, 541:1–20, 2005.
- [259] M. M. Hohman, M. Shin, G. Rutledge, and M. P. Brenner. Electrospinning and electrically forced jets. I. Stability theory. *Phys. Fluids*, 13:2201–2220, 2001.
- [260] W. Yang, H. Duan, C. Li, and W. Deng. Crossover of varicose and whipping instabilities in electrified microjets. *Phys. Rev. Lett.*, 112:054501, 2014.
- [261] J. W. S. Rayleigh. On the equilibrium of liquid conducting masses charged with electricity. *Proc. Roy. Soc.*, 5:110, 1881.
- [262] J. Guerrero, J. Rivero, V. R. Gundabala, M. Perez-Saborid, and A. Fernandez-Nieves. Whipping of electrified liquid jets. *Proc. Natl. Acad. Sci.*, 111:13763–13767, 2014.
- [263] Y. M. Shin, M. M. Hohman, M. P. Brenner, and G. C. Rutledge. Experimental characterization of electrospinning: the electrically forced jet and instabilities. *Polymer*, 42:9955–9967, 2001.
- [264] T. P. Forbes and E. Sisco. Chemical imaging of artificial fingerprints by desorption electro-flow focusing ionization mass spectrometry. *Analyst*, 139:2982, 2014.
- [265] Y. Huang, N. Bu, Y. Duan, Y. Pan, H. Liu, Z. Yin, and Y. Xiong. Electrohydrodynamic direct-writing. *Nanoscale*, 5:12007–12017, 2013.
- [266] I. Liashenko, J. Rosell-Llompart, and A. Cabot. Ultrafast 3D printing with submicrometer features using electrostatic jet deflection. *Nat. Commun.*, 11:753, 2020.
- [267] P. Kiselev and J. Rosell-Llompart. Highly aligned electrospun nanofibers by elimination of the whipping motion. *J. Appl. Polym. Sci.*, 125:2433–2441, 2012.
- [268] Y.-J. Chen and P. H. Steen. Dynamics of inviscid capillary

- breakup: collapse and pinch-off of a film bridge. *J. Fluid Mech.*, 341:245–267, 1997.
- [269] E. F. Goede and M.-C. Yuen. Experiments on liquid jet instability. *J. Fluid Mech.*, 40:495–511, 1970.
- [270] M.-C. Yuen. Non-linear capillary instability of a liquid jet. *J. Fluid Mech.*, 33:151–163, 1968.
- [271] K. C. Chaudhary and T. Maxworthy. The nonlinear capillary instability of a liquid jet. Part 3. Experiments on satellite drop formation and control. *J. Fluid. Mech.*, 96:287–297, 1980.
- [272] N. N. Mansour and T. S. Lundgren. Satellite formation in capillary jet breakup. *Phys. Fluids A*, 2:1141–1144, 1990.
- [273] N. Ashgriz and F. Mashayek. Temporal analysis of capillary jet breakup. *J. Fluid Mech.*, 291:163–190, 1995.
- [274] D. F. Rutland and G. J. Jameson. Theoretical prediction of the sizes of drops formed in the breakup of capillary jets. *Chem. Eng. Sci.*, 25:1689–1698, 1970.
- [275] P. Lafrance. Nonlinear breakup of a laminar liquid jet. *Phys. Fluids*, 18:428–432, 1975.
- [276] E. R. Setiawan and S.D. Heister. Nonlinear modeling of an infinite electrified jet. *J. Electrostat.*, 42:243–257, 1997.
- [277] J. M. Lopez-Herrera, A. M. Gañán-Calvo, and M. Perez-Saborid. One-dimensional simulation of the breakup of capillary jets of conducting liquids. Application to E.H.D. spraying. *J. Aerosol Sci.*, 30:895–912, 1999.
- [278] J. M. López-Herrera and A. M. Gañán-Calvo. A note on charged capillary jet breakup of conducting liquids: experimental validation of a viscous one-dimensional model. *J. Fluid Mech.*, 501:303–326, 2004.
- [279] R. T. Collins, M. T. Harris, and O. A. Basaran. Breakup of electrified jets. *J. Fluid Mech.*, 588:75–129, 2007.
- [280] R. V. Craster, O. K. Matar, and D. T. Papageorgiou. Pinch-off and satellite formation in surfactant covered viscous threads. *Phys. Fluids*, 14:1364–1376, 2002.
- [281] V. Dravid, S. Songsompong, Z. Xue, C. M. Corvalan, and P. E. Sojka. Two-dimensional modeling of the effects of insoluble surfactant on the breakup of a liquid filament. *Chem. Eng. Sci.*, 61:3577–3585, 2006.
- [282] P. T. McGough and O. A. Basaran. Repeated formation of fluid threads in breakup of a surfactant-covered jet. *Phys. Rev. Lett.*, 96:054502, 2006.
- [283] A. Martínez-Calvo and A. Sevilla. Temporal stability of free liquid threads with surface viscoelasticity. *J. Fluid Mech.*, 846:877–901, 2018.
- [284] P. M. Kamat, B. W. Wagoner, S. S. Thete, and O. A. Basaran. Role of Marangoni stress during breakup of surfactant-covered liquid threads: Reduced rates of thinning and microthread cascades. *Phys. Rev. Fluids*, 3:043602, 2018.
- [285] S. Popinet. An accurate adaptive solver for surface-tension-driven interfacial flows. *J. Comput. Phys.*, 228:5838–5866, 2009.
- [286] M. A. Herrada and J. M. Montanero. A numerical method to study the dynamics of capillary fluid systems. *J. Comput. Phys.*, 306:137–147, 2016.
- [287] J. B. Keller and M. T. Miksis. Surface tension driven flows. *SIAM J. Appl. Math.*, 43:268–277, 1983.
- [288] M. R. de Saint Vincent, J. Petit, M. Aytouna, J. P. Delville, D. Bonn, and H. Kellay. Dynamic interfacial tension effects in the rupture of liquid necks. *J. Fluid Mech.*, 692:499–510, 2012.
- [289] I. M. Hauner, A. Deblais, J. K. Beattie, H. Kellay, and D. Bonn. The dynamic surface tension of water. *J. Phys. Chem. Lett.*, 8:1599–1603, 2017.
- [290] A. Deblais, M. A. Herrada, I. Hauner, K. P. Velikov, T. van Roon, H. Kellay, J. Eggers, and D. Bonn. Viscous effects on inertial drop formation. *Phys. Rev. Lett.*, 121:254501, 2018.
- [291] D. T. Papageorgiou. On the breakup of viscous liquid threads. *Phys. Fluids*, 7:1529–1544, 1995.
- [292] M. Rubio, A. Ponce-Torres, E. J. Vega, M. A. Herrada, and J. M. Montanero. Complex behavior very close to the pinching of a liquid free surface. *Phys. Rev. Fluids*, 4:021602(R), 2019.
- [293] M. Moseler and U. Landman. Formation, stability, and breakup of nanojets. *Science*, 289:1165–1169, 2000.
- [294] J. Eggers. Dynamics of liquid nanojets. *Phys. Rev. Lett.*, 89:084502, 2002.
- [295] J. R. Castrejón-Pita, A. A. Castrejón-Pita, S. S. Thet , K. Sambath, I. M. Hutchings, J. Hinch, J. R. Lister, and O. A. Basaran. Plethora of transitions during breakup of liquid filaments. *Proc. Natl. Acad. Sci.*, 112:4582–4587, 2015.
- [296] Y. Li and J. E. Sprittles. Capillary breakup of a liquid bridge: identifying regimes and transitions. *J. Fluid Mech.*, 797:29–59, 2016.
- [297] X. D. Shi, M. P. Brenner, and S. R. Nagel. A cascade of structure in a drop falling from a faucet. *Science*, 265:219–222, 1994.
- [298] T. A. Kowalewski. On the separation of droplets from a liquid jet. *Fluid Dyn. Res.*, 17:121–145, 1996.
- [299] R. Bergmann, D. van der Meer, M. Stijnman, M. Sandtke, A. Prosperetti, and D. Lohse. Giant bubble pinch-off. *Phys. Rev. Lett.*, 96:154505, 2006.
- [300] N. C. Keim, P. Moller, W. W. Zhang, and S. R. Nagel. Breakup of air bubbles in water: memory and breakdown of cylindrical symmetry. *Phys. Rev. Lett.*, 97:144503, 2006.
- [301] S. T. Thoroddsen, T. G. Etoh, and K. Takehara. Experiments on bubble pinch-off. *Phys. Fluids*, 19:042101, 2007.
- [302] H. N. Oguz and A. Prosperetti. Dynamics of bubble growth and detachment from a needle. *J. Fluid Mech.*, 257:111–145, 1993.
- [303] J. C. Burton, R. Waldrep, and P. Taborek. Scaling and instabilities in bubble pinch-off. *Phys. Rev. Lett.*, 94:184502, 2005.
- [304] J. M. Gordillo, A. Sevilla, J. Rodríguez-Rodríguez, and C. Martínez-Bazán. Axisymmetric bubble pinch-off at high Reynolds numbers. *Phys. Rev. Lett.*, 95:194501, 2005.
- [305] J. Eggers, M. A. Fontelos, D. Leppinen, and J. H. Snoeijer. Theory of the collapsing axisymmetric cavity. *Phys. Rev. Lett.*, 98:094502, 2007.
- [306] J. C. Burton and P. Taborek. Bifurcation from bubble to droplet behavior in inviscid pinch-off. *Phys. Rev. Lett.*, 101:214502, 2008.
- [307] B. Dollet, W. van Hoeve, J.-P. Raven, P. Marmottant, and M. Versluis. Role of the channel geometry on the bubble pinch-off in flow-focusing devices. *Phys. Rev. Lett.*, 100:034504, 2008.
- [308] J. R. Lister and H. A. Stone. Capillary breakup of a viscous thread surrounded by another viscous fluid. *Phys. Fluids*, 10:2758–2764, 1998.
- [309] I. Cohen, M. P. Brenner, J. Eggers, and S. R. Nagel. Two fluid drop snap-off problem: Experiments and theory. *Phys. Rev. Lett.*, 83:1147–1150, 1999.
- [310] P. Doshi, I. Cohen, W. W. Zhang, M. Siegel, P. Howel, O. A. Basaran, and S. R. Nagel. Persistence of memory in drop breakup: The breakdown of universality. *Science*, 302:1185–1188, 2003.
- [311] A. A. Pahlavan, H. A. Stone, G. H. McKinley, and R. Juanes. Restoring universality to the pinch-off of a bubble. *Proc. Natl. Acad. Sci.*, 116:13780–13784, 2019.
- [312] H. Y. Lo, Y. Liu, S. Y. Mak, Z. Xu, Y. Chao, K. J. Li, H. C. Shum, and L. Xu. Diffusion-dominated pinch-off of ultralow surface tension fluids. *Phys. Rev. Lett.*, 2019.
- [313] Y. Hennequin, D. G. A. L. Aarts, J. H. van der Wiel, G. Wegdam, J. Eggers, H. N. W. Lekkerkerker, and D. Bonn. Drop

- formation by thermal fluctuations at an ultralow surface tension. *Phys. Rev. Lett.*, 97:244502, 2006.
- [314] J. Petit, D. Riviere, H. Kellay, and J.-P. Delville. Break-up dynamics of fluctuating liquid threads. *Proc. Natl. Acad. Sci.*, 109:18327–18331, 2012.
- [315] M. Rubio-Rubio, W. Mathues, A. Sevilla, and C. Clasen. One-dimensional modelling of the thinning of particulate suspensions near pinch-off. *Int. J. Multiphase Flow*, 108:202–210, 2018.
- [316] D. J. Ruth, W. Mostert, S. Perrard, and L. Deike. Bubble pinch-off in turbulence. *Proc. Natl. Acad. Sci.*, 116:25412–25417, 2019.
- [317] C. Clasen, J. Bico, V. M. Entov, and G. H. McKinley. “Gobbling drops”: the jetting-dripping transition in flows of polymer solutions. *J. Fluid Mech.*, 636:5–40, 2009.
- [318] A. V. Bazilevsky, V. M. Entov, and A. N. Rozhkov. *Liquid filament microrheometer and some of its applications*, volume 1 of *Proceedings of Third European Rheology Conference and Golden Jubilee Meeting of the British Society of Rheology*, pages 41–43. Oliver DR (ed), 1990.
- [319] J. Eggers, M. A. Herrada, and J. H. Snoeijer. Self-similar breakup of polymeric threads as described by the Oldroyd-B model. *J. Fluid Mech.*, 887:A19, 2019.
- [320] W. Mathues, S. Formenti, C. McIlroy, O. G. Harlen, and C. Clasen. CaBER vs ROJER-Different time scales for the thinning of a weakly elastic jet. *J. Rheology*, 62:1135–1153, 2018.
- [321] P. P. Bhat, S. Appathurai, M. T. Harris, M. Pasquali, G. H. McKinley, and O. A. Basaran. Formation of beads-on-a-string structures during break-up of viscoelastic filaments. *Nat. Phys.*, 6:625–631, 2010.
- [322] M. S. N. Oliveira and G. H. McKinley. Iterated stretching and multiple beads-on-a-string phenomena in dilute solutions of highly-extensible flexible polymers. *Phys. Fluids*, 17:071704, 2005.
- [323] R. Sattler, C. Wagner, and J. Eggers. Blistering pattern and formation of nanofibers in capillary thinning of polymer solutions. *Phys. Rev. Lett.*, 100:164502, 2008.
- [324] J. Eggers. Instability of a polymeric thread. *Phys. Fluids*, 26:033106, 2014.
- [325] Q. Wang. Breakup of a poorly conducting liquid thread subject to a radial electric field at zero Reynolds number. *Phys. Fluids*, 24:102102, 2012.
- [326] Q. Wang and D. T. Papageorgiou. Dynamics of a viscous thread surrounded by another viscous fluid in a cylindrical tube under the action of a radial electric field: breakup and touchdown singularities. *J. Fluid Mech.*, 683:27–56, 2011.
- [327] Y.-C. Liao, H. J. Subramani, E. I. Franses, and O. A. Basaran. Effects of soluble surfactants on the deformation and breakup of stretching liquid bridges. *Langmuir*, 20:9926–9930, 2004.
- [328] M. Roche, M. Aytouna, D. Bonn, and H. Kellay. Effect of surface tension variations on the pinch-off behavior of small fluid drops in the presence of surfactants. *Phys. Rev. Lett.*, 103:264501, 2009.
- [329] A. Martínez-Calvo, J. Rivero-Rodríguez, B. Scheid, and A. Sevilla. Natural break-up and satellite formation regimes of surfactant-laden liquid threads. *J. Fluid Mech.*, 883:A35, 2020.
- [330] N. M. Kovalchuk, E. Nowak, and M. J. H. Simmons. Effect of soluble surfactants on the kinetics of thinning of liquid bridges during drops formation and on size of satellite droplets. *Langmuir*, 32:5069–5077, 2016.
- [331] N. M. Kovalchuk, H. Jenkinson, R. Miller, and M. J. H. Simmons. Effect of soluble surfactants on pinch-off of moderately viscous drops and satellite size. *J. Colloid Interface Sci.*, 516:182–191, 2018.
- [332] A. Ponce-Torres, M. Rubio, M. A. Herrada, J. M. Montanero, and J. Eggers. Influence of a nearly-inviscid surfactant on the breakup of a pendant drop. in preparation, 2019.
- [333] A. Martínez-Calvo and A. Sevilla. Universal thinning of liquid filaments under dominant surface dissipation. *arXiv:1912.11499*, pages 1–5, 2019.
- [334] G. Giménez-Ribes, L. M. C. Sagis, and M. Habibi. Interfacial viscoelasticity and aging effect on droplet formation and breakup. *Food Hydrocolloids*, <https://doi.org/10.1016/j.foodhyd.2019.105616>, 2020.
- [335] F. Li, S.-Y. Ke, X.-Y. Yin, and X.-Z. Yin. Effect of finite conductivity on the nonlinear behaviour of an electrically charged viscoelastic liquid jet. *J. Fluid Mech.*, 874:5–37, 2019.
- [336] F. Li, S. Ke, S. Xu, X. Yin, and X. Yin. Radial deformation and disintegration of an electrified liquid jet. *Phys. Fluids*, 32:021701, 2020.
- [337] J. Zeleny. Instability of electrified liquid surfaces. *Phys. Rev.*, 10:1–6, 1917.
- [338] C. T. R. Wilson and G. I. Taylor. The bursting of soap-bubbles in a uniform electric field. *Math. Proc. Cambridge Philos. Soc.*, 22:728–730, 1925.
- [339] F. D. Rumscheidt and S. G. Mason. Particle motions in sheared suspensions XII. Deformation and burst of fluid drops in shear and hyperbolic flows. *J. Colloid Sci.*, 16:238–261, 1961.
- [340] J. D. Sherwood. Tip streaming from slender drops in a nonlinear extensional flow. *J. Fluid Mech.*, 144:281–295, 1984.
- [341] W. J. Milliken and L. G. Leal. Deformation and breakup of viscoelastic drops in planar extensional flows. *J. Non-Newtonian Fluid Mech.*, 40:355–379, 1991.
- [342] D. Duft, T. Achtzehn, R. Muller, B. A. Huber, and T. Leisner. Coulomb fission: Rayleigh jets from levitated microdroplets. *Nature*, 421:128, 2003.
- [343] M. R. Booty and M. Siegel. Steady deformation and tip-streaming of a slender bubble with surfactant in an extensional flow. *J. Fluid Mech.*, 544:243–275, 2005.
- [344] A. T. Brimmoaband and M. A. Qasimeh. Stagnation point flows in analytical chemistry and life sciences. *RSC Adv.*, 7:51206–51232, 2017.
- [345] J. Eggers and S. C. du Pont. Numerical analysis of tips in viscous flow. *Phys. Rev. E*, 79:066311, 2009.
- [346] Y.-H. Tseng and A. Prosperetti. Local interfacial stability near a zero vorticity point. *J. Fluid Mech.*, 776:5–36, 2015.
- [347] M. A. Herrada, A. M. Gañán-Calvo, A. Ojeda-Monge, B. Bluth, and P. Riesco-Chueca. Liquid flow focused by a gas: Jetting, dripping, and recirculation. *Phys. Rev. E*, 78:036323, 2008.
- [348] J. M. Montanero, N. Rebollo-Muñoz, M. A. Herrada, and A. M. Gañán-Calvo. Global stability of the focusing effect of fluid jet flows. *Phys. Rev. E*, 83:036309, 2011.
- [349] W. Zhang. Viscous entrainment from a nozzle: Singular liquid spouts. *Phys. Rev. Lett.*, 93:184502, 2004.
- [350] Q. Wang, M. Siegel, and M. R. Booty. Numerical simulation of drop and bubble dynamics with soluble surfactant. *Phys. Fluids*, 26:052102, 2014.
- [351] B. N. Muñoz-Sánchez, S. F. Silva, D. Pinho, E. J. Vega, and R. Lima. Generation of micro-sized PDMS particles by a flow focusing technique for biomicrofluidics applications. *Biomicrofluidics*, 10:14122, 2016.
- [352] C. G. Garton and Z. Krasucki. Bubbles in insulating liquids: stability in an electric field. *Proc. Roy. Soc. Lon. A*, 280:211–226, 1964.
- [353] T. Achtzehn and R. Muller, D. Duft, and T. Leisner. The Coulomb instability of charged microdroplets: dynamics and scaling. *Eur. Phys. J. D*, 34:311–313, 2005.

- [354] E. Giglio, B. Gervais, J. Rangama, B. Manil, B. A. Huber, D. Duft, R. Muller, T. Leisner, and C. Guet. Shape deformations of surface-charged microdroplets. *Phys. Rev. E*, 77:036319, 2008.
- [355] R. T. Collins, K. Sambath, M. T. Harris, and O. A. Basaran. Universal scaling laws for the disintegration of electrified drops. *Proc. Nat. Acad. Sci.*, 110:4905–4910, 2013.
- [356] N. Gawande, Y. S. Mayya, and R. Thaokar. Jet and progeny formation in the Rayleigh breakup of a charged viscous drop. *J. Fluid Mech.*, 884:A31, 2020.
- [357] K. Mohammadi, M. R. Movahhedy, and S. Khodaygan. A multiphysics model for analysis of droplet formation in electrohydrodynamic 3D printing process. *J. Aerosol Sci.*, 135:72–85, 2019.
- [358] A. M. Gañán-Calvo, N. Rebollo-Muñoz, and J. M. Montanero. Physical symmetries and scaling laws for the minimum or natural rate of flow and droplet size ejected by Taylor cone-jets. *New J. Phys.*, 15:033035, 2013.
- [359] M. A. Fontelos, U. Kindelán, and O. Vantzos. Evolution of neutral and charged droplets in an electric field. *Phys. Fluids*, 20:092110, 2008.
- [360] L. Oddershede and S. R. Nagel. Singularity during the onset of an electrohydrodynamic spout. *Phys. Rev. Lett.*, 85:1234–1237, 2000.
- [361] U. Stachewicz, J. F. Dijkman, C. U. Yurteri, and J. C. Marijnissen. Experiments on single event electrospraying. *Appl. Phys. Lett.*, 91:254109, 2007.
- [362] M. D. Paine. Transient electrospray behaviour following high voltage switching. *Microfluid Nanofluid.*, 6:775–783, 2009.
- [363] Q. Brosseau and P. M. Vlahovska. Streaming from the equator of a drop in an external electric field. *Phys. Rev. Lett.*, 119:034501, 2017.
- [364] J. Beroz, A. J. Hart, and J. W. M. Bush. Stability limit of electrified droplets. *Phys. Rev. Lett.*, 122:244501, 2019.
- [365] O. A. Basaran and L. E. Scriven. Axisymmetric shapes and stability of pendant and sessile drops in an electric field. *J. Colloid Interface Sci.*, 140:10–30, 1990.
- [366] B. W. Zeff, B. Kleber, J. Fineberg, and D. P. Lathrop. Singularity dynamics in curvature collapse and jet eruption on a fluid surface. *Nature*, 403:401–404, 2000.
- [367] A. L. Yarin. Drop impact dynamics: Splashing, spreading, receding, bouncing... *Annu. Rev. Fluid Mech.*, 38:159–192, 2006.
- [368] A. M. Gañán-Calvo. Revision of bubble bursting: Universal scaling laws of top jet drop size and speed. *Phys. Rev. Lett.*, 119:204502, 2017.
- [369] L. Martín-Banderas, M. Flores-Mosquera, P. Riesco-Chueca, A. Rodríguez-Gil, A. Cebolla, S. Chávez, and A. M. Gañán-Calvo. Flow focusing: A versatile technology to produce size-controlled and specific-morphology microparticles. *Small*, 1:688–692, 2005.
- [370] D. P. DePonte, U. Weierstall, K. Schmidt, J. Warner, D. Starodub, J. C. H. Spence, and R. B. Doak. Gas dynamic virtual nozzle for generation of microscopic droplet streams. *J. Phys. D: Appl. Phys.*, 41:195505, 2008.
- [371] B. N. Muñoz-Sánchez and M. G. Cabezas. Borosilicate nozzles manufactured by reproducible fire shaping. *J. Mater. Process. Tech.*, 261:173–183, 2018.
- [372] B. N. Muñoz-Sánchez, A. M. Gañán-Calvo, and M. G. Cabezas. A new fire shaping approach to produce highly axisymmetric and reproducible nozzles. *J. Mater. Process. Tech.*, 270:241–253, 2019.
- [373] T. Si, H. X. Feng, X. S. Luo, and R. X. Xu. Formation of steady compound cone-jet modes and multilayered droplets in a tri-axial capillary flow focusing device. *Microfluid Nanofluid.*, 18:967–977, 2015.
- [374] M. Trebbin, K. Kruger, D. DePonte, S. V. Roth, H. N. Chapman, and S. Forster. Microfluidic liquid jet system with compatibility for atmospheric and high-vacuum conditions. *Lab on a Chip*, 14:1733–1745, 2014.
- [375] K. R. Beyerlein, L. Adriano, M. Heymann, R. Kirjan, J. Knoska, F. Wilde, H. N. Chapman, and S. Bajt. Ceramic micro-injection molded nozzles for serial femtosecond crystallography sample delivery. *Rev. Sci. Instrum.*, 86:125104, 2015.
- [376] G. Nelson et al. Three-dimensional-printed gas dynamic virtual nozzles for X-ray laser sample delivery. *Opt. Express*, 24:11515–11530, 2016.
- [377] J. Knoska et al. Ultracompact 3D microfluidics for time-resolved structural biology. *Nat. Commun.*, 11:657, 2020.
- [378] J. Rosell-Llompart, J. Grifoll, and I. G. Loscertales. Electrosprays in the cone-jet mode: from Taylor cone formation to spray development. *J. Aerosol Sci.*, 2018.
- [379] J. B. Fenn, M. Mann, C. K. Meng, S. F. Wong, and C. M. Whitehouse. Electrospray ionization for mass spectrometry of large biomolecules. *Science*, 246:64–71, 1989.
- [380] M. Gamero-Castaño and V. Hruby. Electrospray as a source of nanoparticles for efficient colloid thrusters. *J. Propul. Power.*, 17:977–987, 2001.
- [381] F. Mei and D.-R. Chen. Investigation of compound jet electrospray: Particle encapsulation. *Phys. Fluids*, 19:103303, 2007.
- [382] S. Chakraborty, I. C. Liao, A. Adler, and K. W. Leong. Electrohydrodynamics: A facile technique to fabricate drug delivery systems. *Adv Drug Deliv Rev.*, 61:1043–1054, 2009.
- [383] T. A. Sill and H. A. von Recum. Electrospinning: applications in drug delivery and tissue engineering. *Biomaterials*, 29:1989–2006, 2008.
- [384] J.-U. Park et al. High-resolution electrohydrodynamic jet printing. *Nature Materials*, 6:782–789, 2007.
- [385] M. S. Onses, E. Sutanto, P. M. Ferreira, A. G. Alleyne, and J. A. Rogers. Mechanisms, capabilities, and applications of high-resolution electrohydrodynamic jet printing. *Small*, 11:4237–4266, 2015.
- [386] J. Bielecki et al. Electrospray sample injection for single-particle imaging with X-ray lasers. *Sci. Adv.*, 5:1–9, 2019.
- [387] A. G. Marín, I. G. Loscertales, M. Márquez, and A. Barrero. Simple and double emulsions via coaxial jet electrosprays. *Phys. Rev. Lett.*, 98:014502, 2007.
- [388] R. Pareta and M. Edirisinghe. A novel method for the preparation of biodegradable microspheres for protein drug delivery. *J. R. Soc. Interface*, 3:573–582, 2006.
- [389] U. Farook, H. B. Zhang, M. Edirisinghe, E. Stride, and N. Safari. Preparation of microbubble suspensions by co-axial electrohydrodynamic atomisation. *Med. Eng. Phys.*, 29:749–754, 2007.
- [390] M. Enayati, Z. Ahmad, E. Stride, and M. Edirisinghe. Size mapping of electric field-assisted production of polycaprolactone particles. *J. R. Soc. Interface*, 7:S393–S402, 2010.
- [391] A. Gupta and P. K. Panigrahi. Alternating current coaxial electrospray for micro-encapsulation. *Exp. Fluids*, <https://doi.org/10.1007/s00348-019-2851-x>, 2020.
- [392] D. H. Reneker, A. Yarin, H. Fong, and S. Koombhongse. Bending instability of electrically charged liquid jets of polymer solutions in electrospinning. *J. Appl. Phys.*, 87:4531–4547, 2000.
- [393] A. L. Yarin, W. Kataphinan, and D. H. Reneker. Branching in electrospinning of nanofibers. *J. Appl. Phys.*, 98:064501, 2005.
- [394] T. Han, D. H. Reneker, and A. L. Yarin. Buckling of jets in electrospinning. *Polymer*, 48:6064–6076, 2007.
- [395] T. Miloh, B. Spivak, and A. L. Yarin. Needleless electrospinning: Electrically driven instability and multiple jetting from the free surface of a spherical liquid layer. *J. Appl. Phys.*, 106:

- 114910, 2009.
- [396] A. L. Yarin, B. Pourdeyimi, and S. Ramakrishna. *Fundamentals and Applications of Micro- and Nanofibers*. Cambridge University Press, Cambridge, Great Britain, 2014.
- [397] A. G. Kanani and S. H. Bahrami. Review on electrospun nanofibers scaffold and biomedical applications. *Trends Biomater. Artif. Organs*, 24:93–115, 2010.
- [398] S. Agarwala, A. Greinera, and J. H. Wendorff. Functional materials by electrospinning of polymers. *Prog. Polym. Sci.*, 38: 963–991, 2013.
- [399] D. Sun, C. Chang, S. Li, and L. Lin. Near-field electrospinning. *Nano Lett.*, 6:839–842, 2006.
- [400] X.-X. He, J. Zheng, G.-F. Yu, M.-H. You, M. Yu, X. Ning, and Y.-Z. Long. Near-field electrospinning: Progress and applications. *J. Phys. Chem. C*, 121:8663–8678, 2017.
- [401] C. Cramer, P. Fischer, and E. J. Windhab. Drop formation in a co-flowing ambient fluid. *Chem. Engin. Sci.*, 59:3045–3058, 2004.
- [402] M. Lauricella, S. Succi, E. Zussman, D. Pisignano, and A. L. Yarin. Models of polymer solutions in electrified jets and solution blowing. *Rev. Mod Phys.*, in press, 2020.
- [403] R. E. Benavides, S. C. Jana, and D. H. Reneker. Nanofibers from scalable gas jet process. *ACS Macro Lett.*, 1:1032–1036, 2012.
- [404] Y. Lin, Y. Yao, X. Yang, N. Wei, X. Li, P. Gong, R. Li, and D. Wu. Preparation of poly(ether sulfone) nanofibers by gas-jet/electrospinning. *J. Appl. Polym. Sci.*, 107:909–917, 2008.
- [405] E. Zhmayev, D. Cho, and Y. L. Joo. Nanofibers from gas-assisted polymer melt electrospinning. *Polymer*, 51:4140–4144, 2010.
- [406] H. Lou, W. Han, and X. Wang. Numerical study on the solution blowing annular jet and its correlation with fiber morphology. *Ind. Eng. Chem. Res.*, 53:2830–2838, 2014.
- [407] A. Sevilla, J. M. Gordillo, and C. Martínez-Bazán. Bubble formation in a coflowing air-water stream. *J. Fluid Mech.*, 530: 181–195, 2005.
- [408] A. Luque, F. A. Perdignes, J. Esteve, J. Montserrat, A. M. Gañán-Calvo, and J. M. Quero. Silicon microdevice for emulsion production using three-dimensional flow focusing. *J. Microelectromech. Syst.*, 16:1201–1208, 2007.
- [409] Y. Morimoto, W.-H. Tan, and S. Takeuchi. Three-dimensional axisymmetric flow-focusing device using stereolithography. *Biomed. Microdevices*, 11:369–377, 2009.
- [410] G. T. Vladislavjevic, J. V. Henry, W. J. Duncanson, H. C. Shum, and D. A. Weitz. Fabrication of biodegradable poly(lactic acid) particles in flow-focusing glass capillary devices. *Progr. Colloid. Polym. Sci.*, 139:111–114, 2012.
- [411] L. Yobas, S. Martens, W. Onga, and N. Ranganathan. High-performance flow-focusing geometry for spontaneous generation of monodispersed droplets. *Small*, 6:1073–1079, 2006.
- [412] P. Zhu, T. Kong, L. Lei, X. Tian, Z. Kang, and L. Wang. Droplet breakup in expansion-contraction microchannels. *Sci. Rep.*, 6:21527, 2016.
- [413] A. Dewandre, J. Rivero-Rodriguez, Y. Vitry, B. Sobac, and B. Scheid. Raydrop: a universal droplet generator based on a non-embedded co-flowfocusing. *arXiv:2002.06909v1*, pages 1–14, 2020.
- [414] A. J. Acero, J. M. Montanero, C. Ferrera, M. A. Herrada, and A. M. Gañán-Calvo. Enhancement of the stability of the flow focusing technique for low-viscosity liquids. *J. Micromech. Microeng.*, 22:115039, 2012.
- [415] M. A. Wiedorn et al. Rapid sample delivery for megahertz serial crystallography at X-ray FELs. *IUCrJ*, 5:574–584, 2018.
- [416] D. Oberthuer et al. Double-flow focused liquid injector for efficient serial femtosecond crystallography. *Sci. Rep.*, 7:44628, 2017.
- [417] C. A. Stan et al. Liquid explosions induced by X-ray laser pulses. *Nat. Phys.*, 12:966–971, 2016.
- [418] A. M. Gañán-Calvo. Scaling laws of an exploding liquid column under an intense ultrashort X-ray pulse. *Phys. Rev. Lett.*, 123:064501, 2019.
- [419] A. M. Gañán-Calvo, E. Castro-Hernández, M. Flores-Mosquera, and L. Martín-Banderas. Massive, generic, and controlled microencapsulation by flow focusing: some physicochemical aspects and new applications. *J. Flow Chem.*, 2014.
- [420] E. Hofmann, K. Krüger, C. Haynl, T. Scheibel, M. Trebbin, and S. Förster. Microfluidic nozzle device for ultrafine fiber solution blow spinning with precise diameter control. *Lab Chip*, 18:2225–2234, 2018.
- [421] A. Ponce-Torres, E. Ortega, M. Rubio, A. Rubio, E. J. Vega, and J. M. Montanero. Gaseous flow focusing for spinning micro and nanofibers. *Polymer*, 178:121623, 2019.
- [422] R. Vasireddi, J. Kruse, M. Vakili, S. Kulkarni, T. F. Keller, D. C. F. Monteiro, and M. Trebbi. Solution blow spinning of polymer/nanocomposite micro-/nanofibers with tunable diameters and morphologies using a gas dynamic virtual nozzle. *Sci. Rep.*, 9:14297, 2019.
- [423] T. Si, G. B. Li, Q. Wu, Z. Q. Zhu, X. S. Luo, and R. X. Xu. Optical droplet vaporization of nanoparticle-loaded stimuli-responsive microbubbles. *Appl. Phys. Lett.*, 108:111109, 2016.
- [424] P. Tirandazi, G. Tomic, and C. H. Hidrov. An ultra-high-throughput flow-focusing microfluidic device for creation of liquid droplets in air. In *Proceedings of the ASME 2017 15th International Conference on Nanochannels, Microchannels, and Minichannels*, pages 1–6, Cambridge, Massachusetts, USA, 2018.
- [425] A. M. Gañán-Calvo, J. M. López-Herrera, and P. Riesco-Chueca. The combination of electrospray and flow focusing. *J. Fluid Mech.*, 566:421–445, 2006.
- [426] T. P. Forbes and E. Sisco. Mass spectrometry detection and imaging of inorganic and organic explosive device signatures using desorption electro-flow focusing ionization. *Anal. Chem.*, 86:7788–7797, 2014.
- [427] G.-B. Lee, C.-I. Hung, B.-J. Ke, G.-R. Huang, B.-H. Hwei, and H.-F. Lai. Hydrodynamic focusing for a micromachined flow cytometer. *J. Fluids Eng.*, 123:672–679, 2001.
- [428] B. J. Sun, H. C. Shum, C. Holtze, and D. A. Weitz. Microfluidic melt emulsification for encapsulation and release of actives. *Appl. Mat. Interf.*, 2:3411–3416, 2010.
- [429] Y. Tsuda, Y. Morimoto, and S. Takeuchi. Monodisperse cell-encapsulating peptide microgel beads for 3D cell culture. *Langmuir*, 26:2645–2649, 2010.
- [430] H. Chen, J. Li, H. C. Shum, H. A. Stone, and D. A. Weitz. Breakup of double emulsions in constrictions. *Soft Matter*, 7: 2345–2347, 2011.
- [431] Y. Chen, L. Wub, and L. Zhang. Dynamic behaviors of double emulsion formation in a flow-focusing device. *Int. J. Multiphase Flow*, 82:42–50, 2015.
- [432] J.-T. Wang, J. Wang, and J.-J. Han. Fabrication of advanced particles and particle-based materials assisted by droplet-based microfluidics. *Small*, 4:1728–1754, 2011.
- [433] Q. Wu, C. Y. Yang, G. L. Liu, W. H. Xu, Z. Q. Zhu, T. Si, and R. X. Xu. Multiplex coaxial flow focusing for producing multicompartment janus microcapsules with tunable material compositions and structural characteristics. *Lab Chip*, 17: 3168–3175, 2017.
- [434] D. F. do Nascimento, A. Mehl J. A. Avendaño, M. J. B. Moura, M. S. Carvalho, and W. J. Duncanson. Flow of tunable elastic microcapsules through constrictions. *Sci. Rep.*, 7:11898, 2017.
- [435] Z. Zhu, Q. Wu, S. Han, W. Xu, F. Zhong, S. Yuan, P. Dwivedi,

- T. Si, and R. X. Xu. Rapid production of single- and multi-compartment polymeric microcapsules in a facile 3D microfluidic process for magnetic separation and synergistic delivery. *Sens. Actuators B Chem.*, 275:190–198, 2018.
- [436] R. Madurga, G. V. Guinea, M. Elices, J. Pérez-Rigueiro, and A. M. Gañán-Calvo. Straining flow spinning: Simplified model of a bioinspired process to mass produce regenerated silk fibers controllably. *Eur. Polymer J.*, 97:26–39, 2017.
- [437] W. Jeong, J. Kim, S. Kim, S. Lee, G. Mensingc, and D. J. Beebe. Hydrodynamic microfabrication via “on the fly” photopolymerization of microscale fibers and tubes. *Lab Chip*, 4: S76–S80, 2004.
- [438] S. A. Nabavi, G. T. Vladislavjevic, and V. Manovic. Mechanisms and control of single-step microfluidic generation of multi-core double emulsion droplets. *Chem. Eng. J.*, 322:140–148, 2017.
- [439] T. Wu, Z. Luo, W. Ding, Z. Cheng, and L. He. Monodisperse droplets by impinging flow-focusing. *Microfluid Nanofluid.*, 21: 129, 2017.
- [440] J. Dong, M. Meissner, M. A. Faers, J. Eggers, A. M. Seddon, and C. P. Royall. Opposed flow focusing: evidence of a second order jetting transition. *Soft Matter*, 14:8344–8351, 2018.
- [441] M. J. Jensen, H. A. Stone, and H. Bruus. A numerical study of two-phase Stokes flow in an axisymmetric flow-focusing device. *Phys. Fluids*, 18:077103, 2006.
- [442] E. J. Vega, A. J. Acero, J. M. Montanero, M. A. Herrada, and A. M. Gañán-Calvo. Production of microbubbles from axisymmetric flow focusing in the jetting regime for moderate Reynolds numbers. *Phys. Rev. E*, 89:063012, 2014.
- [443] J. R. Lister. Selective withdrawal from a viscous two-layer system. *J. Fluid Mech.*, 198:231–254, 1989.
- [444] S. C. Case and S. R. Nagel. Spout states in the selective withdrawal of immiscible fluids through a nozzle suspended above a two-fluid interface. *Phys. Rev. Lett.*, 98:114501, 2007.
- [445] F. Blanchette and W. W. Zhang. Force balance at the transition from selective withdrawal to viscous entrainment. *Phys. Rev. Lett.*, 102:144501, 2009.
- [446] A. Evangelio, F. Campo-Cortés, and J. M. Gordillo. Pressure gradient induced generation of microbubbles. *J. Fluid Mech.*, 778:653–668, 2015.
- [447] K. He, F. Campo-Cortés, M. Goral, T. López-León, and J. M. Gordillo. Micron-sized double emulsions and nematic shells generated via tip streaming. *Phys. Rev. Fluids*, 4:124201, 2019.
- [448] E. Yildirim, Q. Xu, and O. A. Basaran. Analysis of the drop weight method. *Phys. Fluids*, 17:062107, 2005.
- [449] W. D. Harkins and F. E. Brown. The determination of surface tension and the weight of falling drops: The surface tension of water and benzene by the capillary height method. *J. Am. Chem. Soc.*, 41:499–524, 1919.
- [450] M. C. Wilkinson. Extended use of, and comments on, the drop-weight (drop-volume) technique for the determination of surface and interfacial tensions. *J. Colloid Interface Sci.*, 40:14–26, 1972.
- [451] I. Marginean, P. Nemes, and A. Vertes. A stable regime in electrosprays. *Phys. Rev. E*, 76:026320, 2007.
- [452] P. R. Chiarot, S. I. Gubarenko, R. B. Mrad, and P. Sullivan. On the pulsed and transitional behavior of an electrified fluid interface. *J. Fluid Eng.*, 131:091202, 2009.
- [453] S. N. Reznik, A. L. Yarin, A. Theron, and E. Zussman. Transient and steady shapes of droplets attached to a surface in a strong electric field. *J. Fluid Mech.*, 516:349–377, 2004.
- [454] S. N. Reznik, A. L. Yarin, E. Zussman, and L. Bercovici. Evolution of a compound droplet attached to a core-shell nozzle under the action of a strong electric field. *Phys. Fluids*, 18: 062101, 2006.
- [455] S. B. Q. Tran, D. Byun, V. D. Nguyen, and T. S. Kang. Liquid meniscus oscillation and drop ejection by AC voltage, pulsed DC voltage, and superimposing DC to AC voltages. *Phys. Rev. E*, 80:026318, 2009.
- [456] S. B. Q. Tran, D. Byun, H. T. Yudistira, and J. H. Oh. Semi-analytical study of hemispherical meniscus oscillation with an anchored edge on a conductive flat plate under an AC electric field. *Phys. Fluids*, 23:022006, 2011.
- [457] P. B. Umbanhowar, V. Prasad, and D. A. Weitz. Monodisperse emulsion generation via drop break off in a coflowing stream. *Langmuir*, 16:347–351, 2000.
- [458] J. M. Gordillo, A. Sevilla, and C. Martínez-Bazán. Bubbling in a co-flow at high Reynolds numbers. *Phys. Fluids*, 19:077102, 2007.
- [459] O. Amyot and F. Plouraboue. Capillary pinching in a pinched microchannel. *Phys. Fluids*, 19:033101, 2007.
- [460] S. Courrech du Pont and J. Eggers. Sink flow deforms the interface between a viscous liquid and air into a tip singularity. *Phys. Rev. Lett.*, 96:034501, 2006.
- [461] A. Andersen, T. Bohr, B. Stenum, J. J. Rasmussen, and B. Lautrup. Anatomy of a bathtub vortex. *Phys. Rev. Lett.*, 91:104502, 2003.
- [462] R. Bergmann, A. Andersen, D. van der Meer, and T. Bohr. Bubble pinch-off in a rotating flow. *Phys. Rev. Lett.*, 102:104502, 2009.
- [463] P. K. Notz and O. A. Basaran. Dynamics of drop formation in an electric field. *J. Colloid Interface Sci.*, 213:218–237, 1999.
- [464] Z. Wang, R. Li, L. Tian, L. Xia, S. Zhan, J. Wang, and J. Tu. Visualization of periodic emission of drops with micro-dripping mode in electrohydrodynamic (EHD) atomization. *Exp. Thermal Fluid Sci.*, 105:307–315, 2019.
- [465] Q. Xu, M. Hashimoto, T. T. Dang, T. Hoare, D. S. Kohane, G. M. Whitesides, R. Langer, and D. G. Anderson. Preparation of monodisperse biodegradable polymer microparticles using a microfluidic flow-focusing device for controlled drug delivery. *Small*, 5:1575–1581, 2009.
- [466] P. Garstecki, I. Gitlin, W. DiLuzio, G. M. Whitesides, E. Kumacheva, and H. A. Stone. Formation of monodisperse bubbles in a microfluidic flow-focusing device. *Appl. Phys. Lett.*, 85: 2649–2651, 2004.
- [467] C. Clanet and J. C. Lasheras. Transition from dripping to jetting. *J. Fluid Mech.*, 383:307–326, 1999.
- [468] G. I. Taylor. The dynamics of thin sheets of fluid. III. disintegration of fluid sheets. *Proc. R. Soc. Lond. A*, 253:313–321, 1959.
- [469] M. P. Borthakur, G. Biswas, and D. Bandyopadhyay. Formation of liquid drops at an orifice and dynamics of pinch-off in liquid jets. *Phys. Rev. E*, 96:013115, 2017.
- [470] N. S. Clarke. A differential equation in fluid mechanics. *Mathematika*, 12:51–53, 1966.
- [471] J. M. Montanero, M. A. Herrada, C. Ferrera, E. J. Vega, and A. M. Gañán-Calvo. On the validity of a universal solution for viscous capillary jets. *Phys. Fluids*, 23:122103, 2011.
- [472] L. L. F. Agostinho, G. Tamminga, C. U. Yurteri, S. P. Brouwer, E. C. Fuchs, and J. C. M. Marijnissen. Morphology of water electrosprays in the simple-jet mode. *Phys. Rev. E*, 86:066317, 2012.
- [473] L. L. F. Agostinho, C. U. Yurteri, E. C. Fuchs, and J. C. M. Marijnissen. Monodisperse water microdroplets generated by electrohydrodynamic atomization in the simple-jet mode. *Appl. Phys. Lett.*, 100:244105, 2012.
- [474] W. van Hoeve, B. Dollet, J. M. Gordillo, M. Versluis, L. van Wijngaarden, and D. Lohse. Bubble size prediction in co-flowing streams. *EPL*, 94:64001, 2011.
- [475] S. Tomotika. Breaking up of a drop of viscous liquid immersed

- in another viscous fluid which is extending at a uniform rate. *Proc. Roy. Soc. Lond.*, 153:302–318, 1936.
- [476] I. Cohen and S. R. Nagel. Scaling at the selective withdrawal transition through a tube suspended above the fluid surface. *Phys. Rev. Lett.*, 88:074501, 2002.
- [477] I. Cohen. Scaling and transition structure dependence on the fluid viscosity ratio in the selective withdrawal transition. *Phys. Rev. E*, 70:026302, 2004.
- [478] D. Zhou and J. J. Feng. Selective withdrawal of polymer solutions: Experiments. *J. Non-Newtonian Fluid Mech.*, 165: 829–838, 2010.
- [479] J. Eggers and S. Courrech du Pont. Comment on “force balance at the transition from selective withdrawal to viscous entrainment”. *Phys. Rev. Lett.*, 105:089401, 2010.
- [480] G. Benassayag, P. Sudraud, and B. Jouffrey. In situ high voltage tem observation of an electrohydrodynamic (EHD) ion source. *Ultramicroscopy*, 16:1–8, 1985.
- [481] W. Driesel, Ch. Dietzsch, H. Niedrig, and B. Praprotnik. HV TEM in situ investigations of the tip shape of a gallium liquid-metal ion/electron emitter. *Ultramicroscopy*, 57:45–58, 1995.
- [482] J. Fernandez de la Mora and I. G. Loscertales. The current transmitted through an electrified conical meniscus. *J. Fluid Mech.*, 260:155–184, 1994.
- [483] J. F. de la Mora and I. G. Loscertales. The current emitted by highly conducting Taylor cones. *J. Fluid Mech.*, 260:155–84, 1994.
- [484] A. M. Gañán-Calvo, A. Barrero, and C. Pantano. The electrohydrodynamics of electrified conical menisci. *J. Aerosol Sci.*, 24:S19–20, 1993.
- [485] R. P. A. Hartman, D. J. Brunner, D. M. A. Camelot, J. C. M. Marijnissen, and B. Scarlett. Electrohydrodynamic atomization in the cone-jet mode physical modeling of the liquid cone and jet. *J. Aerosol Sci.*, 30:823–849, 1999.
- [486] H. H. Xia, A. Ismail, J. Yao, and J. P. W. Stark. Scaling laws for transition from varicose to whipping instabilities in electrohydrodynamic jetting. *Phys. Rev. Appl.*, 12:014031, 2019.
- [487] M. Cloupeau and B. Prunet-Foch. Electrostatic spraying of liquids in cone-jet mode. *J. Electrostatics*, 22:135–159, 1989.
- [488] D. B. Bober and C.-H. Chen. Pulsating electrohydrodynamic cone-jets: from choked jet to oscillating cone. *J. Fluid Mech.*, 689:552–563, 2011.
- [489] W. J. Scheideler and C.-H. Chena. The minimum flow rate scaling of Taylor cone-jets issued from a nozzle. *Appl. Phys. Lett.*, 104:024103, 2014.
- [490] M. Gamero-Castaño and M. Magnani. The minimum flow rate of electrosprays in the cone-jet mode. *J. Fluid Mech.*, 876: 553–572, 2019.
- [491] H. Park, K. Kim, and S. Kim. Effects of a guard plate on the characteristics of an electrospray in the cone-jet mode. *J. Aerosol Sci.*, 35:1295–1312, 2004.
- [492] S. Martin, A. Perea, P. L. Garcia-Ybarra, and J. L. Castillo. Effect of the collector voltage on the stability of the cone-jet mode in electrohydrodynamic spraying. *J. Aerosol Sci.*, 46: 53–63, 2012.
- [493] C. Li, M. Chang, W. Yang, A. Madden, and W. Deng. Ballpoint pen tips as robust cone-jet electrospray emitters. *J. Aerosol Sci.*, 77:10–15, 2014.
- [494] M. Morad, A. Rajabi, M. Razavi, and S. P. Sereshkeh. A very stable high throughput Taylor cone-jet in electrohydrodynamics. *Sci. Rep.*, 6:38509, 2016.
- [495] M. Cloupeau and B. Prunet-Foch. Electrohydrodynamic spraying functioning modes: A critical review. *J. Aerosol Sci.*, 25: 1021–1036, 1994.
- [496] B. Pongrac, F. Krcma, L. Dostal, H.-H. Kim, T. Homola, and Z. Machala. Effects of corona space charge polarity and liquid phase ion mobility on the shape and velocities of water jets in the spindle jet and precession modes of water electro-spray. *J. Aerosol Sci.*, 101:196–206, 2016.
- [497] D. Li and Y. Xia. Electrospinning of nanofibers: Reinventing the wheel? *Adv. Mater.*, 16:1151–1170, 2004.
- [498] A. Greiner and J. H. Wendorff. Electrospinning: A fascinating method for the preparation of ultrathin fibers. *Angewandte Chemie-International Edition*, 46:5670–5703, 2007.
- [499] X. Chen, L. Jia, X. Yin, J. Cheng, and J. Lu. Spraying modes in coaxial jet electrospray with outer driving liquid. *Phys. Fluids*, 17:032101, 2005.
- [500] J. López-Herrera, M. Herrada, M. Gamero-Castaño, and A. M. Gañán-Calvo. A numerical simulation of coaxial electrosprays. *J. Fluid Mech.*, 885:A15, 2020.
- [501] X. Liu, L. Wu, Y. Zhao, and Y. Chen. Study of compound drop formation in axisymmetric microfluidic devices with different geometries. *Colloids Surf. A*, 533:87–98, 2017.
- [502] L. Wu, X. Liu, Y. Zhao, and Y. Chen. Role of local geometry on droplet formation in axisymmetric microfluidics. *Chem. Eng. Sci.*, 163:56–67, 2017.
- [503] K. Mu, H. Ding, and T. Si. Instability analysis of the cone-jet flow in liquid-driven flow focusing. *Microfluid. Nanofluidics*, 22:138, 2018.
- [504] M. Nooranoost, D. Izbassarov, and M. Muradoglu. Droplet formation in a flow focusing configuration: Effects of viscoelasticity. *Phys. Fluids*, 28:123102, 2016.
- [505] T. M. Moyle, L. M. Walker, and S. L. Anna. Predicting conditions for microscale surfactant mediated tipstreaming. *Phys. Fluids*, 24:082110, 2012.
- [506] J. K. Wrobel, M. R. Booty, M. Siegel, and Q. Wang. Simulation of surfactant-mediated tipstreaming in a flow-focusing geometry. *Phys. Rev. Fluids*, 3:114003, 2018.
- [507] A. M. Gañán-Calvo, M. Pérez-Saborid, J. M. López-Herrera, and J. M. Gordillo. Steady high viscosity liquid micro-jet production and fiber spinning using co-flowing gas conformation. *Eur. Phys. J. B*, 39:131–137, 2004.
- [508] A. Umemura. Self-stabilizing mechanism of a laminar inviscid liquid jet issuing from a circular nozzle. *Phys. Rev. E*, 83: 046307, 2011.
- [509] A. Umemura, J. Osaka, J. Shinjo, Y. Nakamura, S. Matsumoto, M. Kikuchi, T. Taguchi, H. Ohkuma, T. Dohkojima, T. Shi-maoka, T. Sone, H. Nakagami, and W. Ono. Coherent capillary wave structure revealed by ISS experiments for spontaneous nozzle jet disintegration. *Microgravity Sci. Technol.*, <https://doi.org/10.1007/s12217-019-09756-0>, 2020.
- [510] R. Zahoor, G. Belsak, S. Bajt, and B. Sarler. Simulation of liquid micro-jet in free expanding high-speed co-flowing gas streams. *Microfluidics and Nanofluidics*, 22:87, 2018.
- [511] T. Si, F. Li, X.-Y. Yin, and X.-Z. Yin. Spatial instability of coflowing liquid-gas jets in capillary flow focusing. *Phys. Fluids*, 22:112105, 2010.
- [512] F. Marra, A. De Vivo, and F. Sarghini. Virtualization of fluid-dynamics in micro-air assisted extruders for food microfluidic based encapsulation. *J. Food Eng.*, 213:89–98, 2017.
- [513] R. Zahoor, S. Bajt, and B. Sarler. Influence of gas dynamic virtual nozzle geometry on micro-jet characteristics. *Int. J. Multiphase Flow*, 104:152–165, 2018.
- [514] K. Muhlig, A. M. Gañán-Calvo, J. Andreasson, D. S. D. Larson, J. Hajdua, and M. Svenda. Nanometre-sized droplets from a gas dynamic virtual nozzle. *J. Appl. Cryst.*, 52:800–808, 2019.
- [515] T. Fu, Y. Ma, D. Funfschilling, and H. Z. Li. Bubble formation and breakup mechanism in a microfluidic flow-focusing device. *Chem. Engin. Sci.*, 64:2392–2400, 2009.
- [516] D. C. Blanchard and A. H. Woodcock. Bubble formation and

- modification in the sea and its meteorological significance. *Tellus*, 9:145–158, 1957.
- [517] L. Duchemin, S. Popinet, C. Josserand, and S. Zaleski. Jet formation in bubbles bursting at a free surface. *Phys. Fluids*, 14:3000–3008, 2002.
- [518] E. Ghabache, G. Liger-Belair, A. Antkowiak, and T. Séon. Evaporation of droplets in a Champagne wine aerosol. *Sci. Rep.*, 6:25148, 2016.
- [519] L. Deike, E. Ghabache, G. Liger-Belair, A. K. Das, S. Zaleski S., S. Popinet, and T. Seon. Dynamics of jets produced by bursting bubbles. *Phys. Rev. Fluids*, 3:013603, 2018.
- [520] A. Antkowiak, N. Bremond, S. Le Dices, and E. Villermaux. Short-term dynamics of a density interface following an impact. *J. Fluid Mech.*, 577:241–250, 2007.
- [521] A. A. Castrejón-Pita, J. R. Castrejón-Pita, and G. D. Martin. A novel method to produce small droplets from large nozzles. *Rev. Sci. Instrum.*, 83:115105, 2012.
- [522] A. S. Ismail, A. M. Gañán-Calvo, J. R. Castrejón-Pita, M. A. Herrada, and A. Castrejón-Pita. Controlled cavity collapse: scaling laws of drop formation. *Soft Matter*, 14:7671–7679, 2018.
- [523] C.-Y. Lai, J. Eggers, and L. Deike. Bubble bursting: Universal cavity and jet profiles. *Phys. Rev. Lett.*, 121:144501, 2018.
- [524] P. L. L. Walls, L. Henaux, and J. C. Bird. Jet drops from bursting bubbles: How gravity and viscosity couple to inhibit droplet production. *Phys. Rev. E*, 92:021002(R), 2015.
- [525] C. F. Brasz, C. T. Bartlett, P. L. L. Walls, E. G. Flynn, Y. E. Yu, and J. C. Bird. Minimum size for the top jet drop from a bursting bubble. *Phys. Rev. Fluids*, 3:074001, 2018.
- [526] J. M. Gordillo and J. Rodríguez-Rodríguez. Capillary waves control the ejection of bubble bursting jets. *J. Fluid Mech.*, 867:556–571, 2019.
- [527] J. Dinic, M. Biagioli, and V. Sharma. Pinch-off dynamics and extensional relaxation times of intrinsically semi-dilute polymer solutions characterized by dripping-onto-substrate rheometry. *J. Polym. Sci. B*, 55:1692–1704, 2017.
- [528] O. A. Basaran, H. Gao, and P. P. Bhat. Nonstandard inkjets. *Annu. Rev. Fluid Mech.*, 45:85–113, 2013.
- [529] G. E. A. Meier, A. Klopper, and G. Grabitz. The influence of kinematic waves on jet break down. *Exp. Fluids*, 12:173–180, 1992.
- [530] C. McIlroy and O. G. Harlen. Effects of drive amplitude on continuous jet break-up. *Phys. Fluids*, 31:064104, 2019.
- [531] J. W. S. Rayleigh, Lord. On the capillary phenomena of jets. *Proc. R. Soc. London, Ser. A*, 29:71–97, 1879.
- [532] A. E. Hasha and J. W. M. Bush. Fluid fishbones. *Phys. Fluids*, 14:S8, 2002.
- [533] J. D. Koralek, J. B. Kim, P. Bruza, C. B. Curry, Z. Chen, H. A. Bechtel, A. A. Cordones, P. Sperling, S. Toleikis, J. F. Kern, S. P. Moeller, S. H. Glenzer, and D. P. DePonte. Generation and characterization of ultrathin free-flowing liquid sheets. *Nat. Commun.*, 9:1353, 2018.